Spatially-resolved x-ray scattering experiments

by

Eliseo J. Gamboa

A dissertation submitted in partial fulfillment
of the requirements for the degree of
Doctor of Philosophy
(Applied Physics)
in The University of Michigan
2013

Doctoral Committee:

Professor R Paul Drake, Co-chair
Associate Research Scientist Paul A. Keiter, Co-chair
Associate Professor John E. Foster
Professor Alec D. Gallimore
Professor Karl M. Krushelnick

TABLE OF CONTENTS

LIST OF FIGURES

Figure

LIST OF ABBREVIATIONS

CCD charge-coupled device

CPA chirped pulse amplification

CRF carbonized resorcinol formaldehyde

DPP distributed phase plate

DSF dynamic structure factor

DT deuterium-tritium

EOS equation of state

FCC frequency conversion crystal

FFA form factor approximation

FWHM full width at half maximum

GDL Glass development laser

HEDP high energy density physics

HOPG highly oriented pyrolytic graphite

IA impulse approximation

ICF inertial confinement fusion

IXTS Imaging x-ray Thomson spectrometer

KDP potassium dihydrogen phosphate

LANL Los Alamos National Laboratory

LLE Laboratory for Laser Energetics

LLNL Lawrence Livermore National Laboratories

LPI Laser-plama instability

MCF magnetic confinement fusion

MCP microchannel plate

NIF National Ignition Facility

NLUF National Laser Users' Facility

PHD pulse height distribution

PSF point spread function

RPA random phase approximation

RPP random phase plate

SBS stimulated Brillouin scattering

SNR signal-to-noise ratio

SOP Streaked optical pyrometer

SRS stimulated Raman scattering

SSD smoothing by spectral dispersion

TBR tritium burning ratio

TIM Ten-inch manipulator

VISAR Velocity Interferometer System for Any Reflector

WDM warm dense matter

XRS x-ray scattering code

XRTS x-ray Thomson scattering

ABSTRACT

Spatially-resolved x-ray scattering experiments

by

Eliseo J. Gamboa

Co-chairs: R Paul Drake, Paul A. Keiter

In many laboratory astrophysics experiments, intense laser irradiation creates novel material conditions with large, one-dimensional gradients in the temperature, density, and ionization state. X-ray Thomson scattering (XRTS) is a powerful technique for measuring these parameters in dense plasmas. However, the scattered signal has previously been measured with little or no spatial resolution. This limits XRTS to characterizing homogenous plasmas like steady shocks or isochorically heated matter.

This dissertation reports on the development of the imaging x-ray Thomson spectrometer diagnostic for the Omega laser facility, which extends XRTS to the general case of plasmas with one-dimensional structure. The diffraction of x-rays from a toroidally-curved crystal creates high-resolution images that are simultaneously spectrally and spatially resolved along a one-dimensional profile.

The technique of imaging x-ray Thomson scattering is applied to produce the first measurements of the spatial profiles of the temperature, ionization state, relative material density, and shock speed of a blast wave in a high-energy density system. A decaying shock is probed with 90° scattering of 7.8 keV helium-like nickel x-rays. The spatially-resolved scattering is used to infer the material conditions along the shock

axis. These measurements enable direct comparison of the temperature as observed with that inferred from other quantities, with good agreement.

CHAPTER I

Introduction

1.1 Warm dense matter

Warm dense matter (WDM) is a state of matter common to massive bodies in the solar system and beyond. It encompasses a physical regime of matter that is much more energetic than can be described by condensed matter physics, yet significantly colder and denser than classical high temperature, low-density plasmas. At pressures above 1 Mbar and temperatures on the order of 10 eV, atoms may only be slightly ionized leading to strong inter-ion forces and a partially degenerate electron population. A rigorous understanding of the equation of state (EOS) of these materials is essential to the validity of models for planetary interiors (1), which sheds light on the origin of planetary magnetic fields (2) and the formation and distribution of extra-solar planets (3). The dynamics of WDM are also important to inertial confinement fusion (4), where WDM is created in the outer layers of the fuel capsule.

The study of WDM more generally belongs to the field of plasma physics, which finds applications to a diverse set of fields from cosmology to medicine. Plasmas span an enormous parameter space in density and temperature from the tenuous interstellar medium containing just a few particles per cubic centimeter at a fraction of an eV to the extreme conditions inside a pair instability supernova with densities on the order of 7×10^5 g/cc and temperatures of over 240 keV (5). For the conditions of present

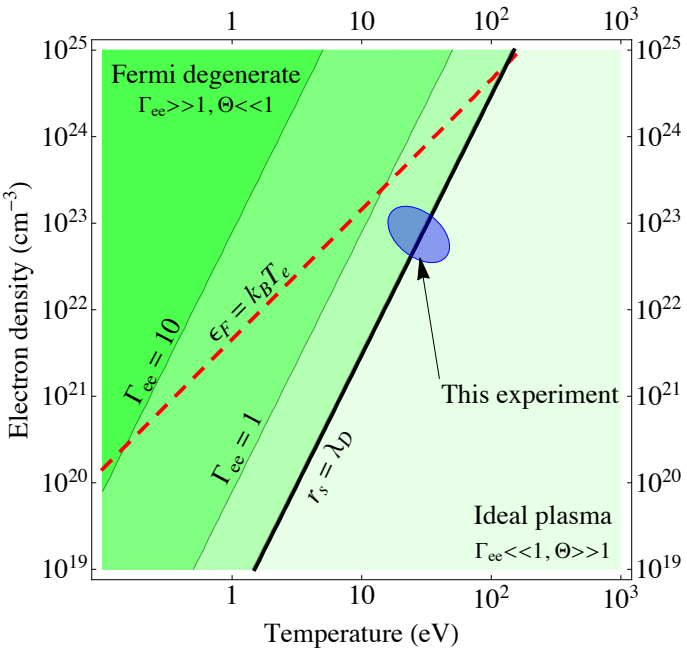

Figure 1.1: The Coulomb coupling parameter Γ_{ee} and degeneracy parameter Θ are plotted over temperature-density space. A blue shaded region shows the approximate extent of the conditions characterized in the experiments presented in this dissertation.

interest, plasmas may interact through some combination of thermal, electrostatic, and quantum forces. The scaling of the physical interactions may be characterized with a few dimensionless parameters, which help express the range of applicability of theoretical descriptions.

The Coulomb coupling parameter is defined as the ratio of the electrostatic potential energy to the thermal energy. For electrons, this may be written as

$$\Gamma_{ee} = \frac{e^2}{r_s k_B T},\ r_s = \left(\frac{4\pi n_e}{3}\right)^{\frac{-1}{3}} \tag{1.1}$$

where we can get an analogous coupling term for two ionic species, a and b, by replacing e^2 with $Z_a Z_b e^2$ and n_e with n_i. Here the Wigner-Seitz radius, r_s, is the mean separation between the electrons.

Likewise, the degeneracy parameter measures the strength of quantum effects in

the plasma. It is taken as the ratio between the electron temperature and the Fermi energy.

$$\Theta = \frac{k_b T}{\epsilon_F},\ \epsilon_F = \frac{\hbar^2}{2m_e}(3\pi^2 n_e)^{2/3} \tag{1.2}$$

The thermodynamic state of the plasma is dependent upon the Hamiltonian of the individual particles through the definition of the partition function. If either of the dimensionless parameters are at an extreme value, we can assume one of the three interactions dominates the Hamiltonian and the other effects are separable perturbations. For example, if $\Gamma_{ee} << 1$, the electrostatic coupling is minimal so that the system may be treated as an ideal gas. This can be either a quantum gas for $\Theta << 1$ or a classical one in the opposite limit. Quantum corrections may be introduced as small additive terms in the Hamiltonian, such as the effect of ionization for hot plasmas or exchange forces for cold ones.

For weakly coupled systems, the electric fields are at least partially screened by the charges in the plasma. This reduces or eliminates long range order in the system. In a classical plasma, electric fields are screened over distances larger than a Debye length.

$$\lambda_D = \sqrt{\frac{k_B T}{4\pi n_e e^2}}. \tag{1.3}$$

A basic requirement for the screening is a large number of charges within the screening volume. This condition is equivalent to $n_e \lambda_D^3 >> 1$, which is fulfilled for high temperatures and low densities. A similar screening effect occurs in degenerate plasmas, which we may define as one in which the thermal wavelengths of the particles overlap. Writing the de Broglie wavelength of an electron as

$$\Lambda_e = \frac{h}{2\pi m_e k_B T}, \tag{1.4}$$

a degenerate plasma contains many particles within a volume defined by the thermal wavelength, $n_e\Lambda_e^3 >> 1$. Evidently, this will occur at low temperatures and high densities. The Thomas-Fermi model is applicable to the screening of the electric fields with a characteristic screening length of

$$\lambda_{TF} = \sqrt{\frac{\epsilon_F}{6\pi n_e e^2}}. \tag{1.5}$$

In the intermediate case of medium temperatures and densities, the plasma can no longer effectively screen electric fields. For a classical plasma, as we increase the density the interparticle spacing decreases. When the Wigner-Seitz radius becomes smaller than the Debye length, the screening clouds begin to overlap. Charges may now interact, leading to correlations in the motions of the particles in the plasma. We can then make the distinction between an ideal plasma and a weakly coupled one by the requirement that $\lambda_D = r_s$.

WDM can be defined as a strongly coupled plasma ($\Gamma_{ee} \sim 1$) with partial degeneracy ($\Theta \geq 1$) (6). The plasma is not effective in screening electric fields, so it may exhibit long range order that is typical of fluids or solids. Plotted in Figure 1.1 are the two dimensionless parameters over a wide temperature-density space spanning from an ideal plasma to a Fermi-degenerate solid. Using the previous definitions, WDM loosely corresponds to the region around the intersection of the lines $\Theta = 1$ and $\Gamma_{ee} = 1$ with temperatures from a few to tens of eV and near or above solid density.

This state is challenging to describe theoretically because of the similar strength of the quantum, thermal, and electrostatic interactions, which makes a perturbative expansion invalid (7). Additionally, higher-Z systems may be in a state of partial electron degeneracy and strong ion coupling (8). Various theoretical approaches to model the EOS and material properties like the opacity and the electrical and thermal conductivities of WDM have given inconsistent results (9). This demonstrates the

need to perform experiments to characterize these measurable quantities to better constrain the theoretical descriptions.

1.2 Nuclear fusion

With the exception of isolated communities of chemosynthetic organisms (10), all of life on the Earth is dependent on the energy that is created by fusion reactions that take place in the core of the sun. Stellar fusion was first proposed by Arthur Eddington in the 1920s, based upon early quantum theory and the results of a precise measurement of the masses of the atoms. Eddington conjectured that the sun converted hydrogen into helium, releasing the small difference in mass between four hydrogen atoms and helium as energy. The details of this reaction would be later revealed by Hans Bethe in work which resulted in the 1967 Nobel Prize in Physics.

In stars about the same size as the sun, fusion is dominated by the proton-proton chain in which four protons are converted into a ^{4}He nucleus. The first step is the joining of two protons to form a ^{2}He nucleus. This state is highly unstable and the majority of the time it splits back into two protons. There is a very small chance that the ^{2}He nucleus will undergo β^+ decay to form a deuteron. The deuteron carries on the reaction, fusing with another proton to form ^{3}He and then with another ^{3}He to create a ^{4}He nucleus and two extra protons. The formation of the deuteron is the bottleneck for this reaction and, consequently, the sun burns its fuel very slowly. This slow reaction rate is responsible for the long lifetimes of stars, which is perhaps 10 billion years for a main-sequence star like the sun.

The proton-proton reaction would be unsuitable for terrestrial energy production as it requires high densities, temperatures, and long confinement times. In the core of the sun, temperatures reach up to 15 million K with a density of 150 g/cm^3. While these conditions may be partly met in fusion experiments, the sun maintains this state for billions of years, which compensates for the extremely slow reaction rate of

the proton-proton chain. The power density at the core of the sun is only the order of 300 W/m^3 (11), which is amusingly within a factor of two or so of human metabolism and several orders of magnitude less than a commercial fission reactor.

1.2.1 Fusion reactions relevant to energy production

Fusion energy research is primarily focused on the deuterium-tritium (DT) reaction of the two heavy hydrogen isotopes. For a fusion reaction to take place, the nuclei must be brought close enough for the attraction from the strong nuclear force to overcome the electrostatic repulsion. The strong force scales with the number of nucleons, so the heavy isotopes of hydrogen are the easiest to bring together. The DT reaction releases 17.6 MeV of energy, which is split between the kinetic energy of a ^{4}He nucleus and a free neutron.

$$\mathrm{D} + \mathrm{T} \rightarrow {}^4\mathrm{He} + \mathrm{n} + 17.6\ \mathrm{MeV} \tag{1.6}$$

By momentum conservation, the majority of the energy is carried by the neutron. At temperatures of interest for terrestrial fusion reactors, a less probable reaction is the fusion of two deuterium nuclei

$$\mathrm{D} + \mathrm{D} \rightarrow {}^3\mathrm{He} + \mathrm{n} + 3.27\ \mathrm{MeV} \tag{1.7}$$

$$\mathrm{D} + \mathrm{D} \rightarrow \mathrm{T} + \mathrm{H} + 4.03\ \mathrm{MeV}. \tag{1.8}$$

These species may undergo various other fusion processes, including T-T, D- ^{3}He, ^{3}He- ^{3}He, but these are much rarer owing to the smaller reaction cross section.

The first artificial fusion reaction to release a significant amount of energy was the "George" explosion in the Operation Greenhouse series of nuclear tests conducted by the United States in 1951. In this test, a container of DT gas was attached to a large fission bomb. The later "Item" test would be the basis what would later be called a

boosted fission weapon. A small amount of DT gas was introduced into the center of the fission "primary" bomb. The heating from the fission explosion drove fusion reactions in the DT gas, which provided fast neutrons to increase the fission reaction rate in the primary.

The American Castle Bravo and Soviet RDS-37 hydrogen bomb tests in 1954 and 1955 would be more representative of later proposals for fusion energy. The fusion fuel was lithium deuteride, which is an ionic solid at room temperature. Neutrons from the fission primary bred tritium from the two naturally occurring isotopes of lithium

$$^{6}\mathrm{Li} + \mathrm{n} \rightarrow \ ^{4}\mathrm{He} + \mathrm{T} + 4.78 \text{ MeV} \tag{1.9}$$

$$^{7}\mathrm{Li} + \mathrm{n} \rightarrow \ ^{4}\mathrm{He} + \mathrm{T} + \mathrm{n} - 2.47 \text{ MeV}. \tag{1.10}$$

In a hydrogen bomb, the implosion of a plutonium spark plug creates an excess of neutrons to create tritium. This tritium is consumed in the DT reaction, creating additional neutrons to breed more tritium and burn up the fissile tamper. With a half-life of only 12 years, only trace amounts of tritium are found in the environment. To achieve a closed fuel cycle, any fusion energy plant must be able to create and recover more than one tritium atom per fusion reaction .

1.2.2 Approaches to fusion energy

Conceptually, a fusion energy reactor would consist of a means to create and extract energy from a very hot DT plasma. This reaction emits most of the energy in the form of energetic neutrons. Those neutrons must interact with a blanket made of a material like lithium to breed the tritium fuel needed to supply the reactor. The tritium must be efficiently extracted from the blanket and processed to fuel the reaction. Energy can then be pulled from the fusion neutrons through heating a

working fluid for a heat engine.

The two main research efforts into controlled fusion energy are inertial confinement fusion (ICF) and magnetic confinement fusion (MCF). In ICF, large amounts of energy are deposited onto a hollow DT fuel capsule, driving an inward implosion that compresses and heats the fuel to conditions favorable to fusion. In MCF, magnetic fields are used to contain a low-density DT plasma which is heated by various methods to induce fusion. Current research in these two communities centers on demonstrating a burning plasma that generates an excess of energy. The two largest experimental efforts in these two fields are the National Ignition Facility (NIF) at Lawrence Livermore National Laboratories (LLNL) in the USA and the international collaboration that forms the ITER magnetic confinement fusion (MCF) project.

A successful fusion power plant must produce both an excess of energy and tritium fuel. These two requirements can be parameterized in the following way. The fusion energy gain factor, Q, is the ratio of the fusion power produced to the power consumed in maintaining the reaction. The tritium burning ratio (TBR) is defined as the average number of atoms of tritium that are bred per DT reaction. For break-even operation, both of these parameters would be equal to unity.

The economic feasibility of a fusion reactor depends on how large the values of these two parameters can be achieved. A reactor must produce a large energy surplus with $Q >> 1$. In the context of ICF, this represents a self-propagating reaction where the energetic alpha particles deposit enough energy to burn a significant fraction of the fuel; in MCF the goal is continuous operation. A commercial power plant must also have TBR > 1, to both account for losses in the recovery and refining process and to provide for safety margins for interruptions in the fuel supply.

The fusion triple product provides a useful metric for the conditions that are needed to create an ignited plasma. It is defined as the product of the density (n), temperature (T), and energy confinement time (τ_e) (12). For a self-sustaining DT

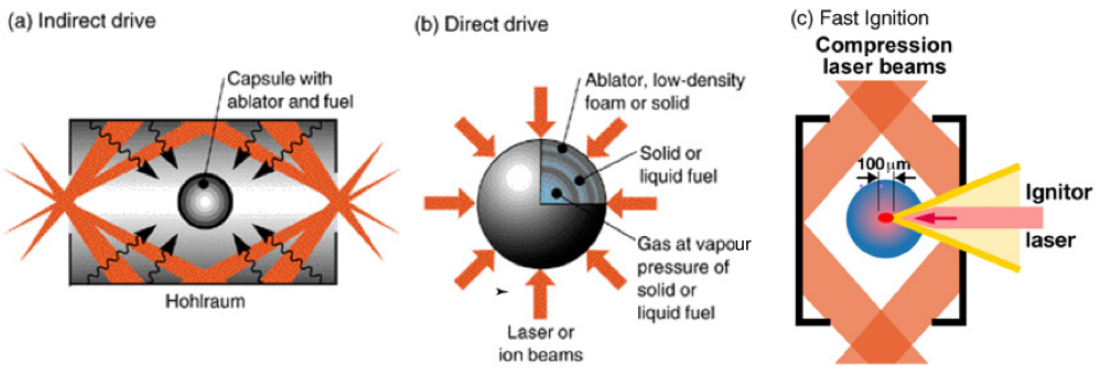

Figure 1.2: Three schemes for ICF are (a) indirect drive, (b) direct drive, and (c) fast ignition (14)

reaction, the triple product must be at least

$$nT\tau_e > 5 \times 10^{15} \text{ keV} \cdot \text{s/cm}^3. \tag{1.11}$$

MCF aims for low-density plasmas ($\sim 10^{13}$ cm^{-3}) with long confinement times (tens of seconds). Alternatively, ICF favors high densities (10^{26} cm^{-3}) and short confinement times (tens of ps) (13).

1.2.3 Inertial confinement fusion

An illustration of three different approaches to ICF is shown in Figure 1.2. All three approaches employ the same basic strategy and elements. The target is a fuel capsule consisting of a hollow DT ice shell, surrounded by a solid ablator made of plastic or a similar low-Z material, with the interior filled with DT gas. A sudden burst of energy drives a shock that implodes the fuel inwards, creating a highly compressed final state. While the shock implosion leads to both heating and compression of the fuel, which drives the triple product, reaching an ignited state with shocks alone would require an unfeasibly enormous amount of energy (4). ICF attempts to sidestep this problem by separating the compression and heating stages, with the bulk of the

compressed fuel self-heated by fusion reactions that begin at a central "hot-spot".

Conceptually, the simplest configuration is direct drive where laser energy is deposited onto the surface of a fuel capsule. The laser energy heats the ablator to temperatures of several keV, causing a plasma to stream away from the surface at a high velocity. The momentum flux from this ablated material drives a steady shock that pushes the DT shell inwards at velocities of hundreds of km/s. This spherical implosion converges at the center of the capsule and stagnates, with the shell dumping its kinetic energy into the enclosed DT gas. At this point, the shell is compressed to densities on the order of 1000 g/cm^3 while the DT gas is heated to several keV (15), creating a central hot spot at high densities and temperatures. Fusion reactions begin at the hot spot and release large amounts of energy. Some of this energy is absorbed by the rest of the assembled fuel, raising its temperature and inducing further fusion reactions in an outward propagating wave.

Direct drive puts stringent requirements on the spatial uniformity of the capsule surface and the laser or ion beams used to drive the implosion. Small non-uniformities in the intensity of the laser spots can drive fluid instabilities that greatly reduce the compression of the fuel.

Indirect drive (4) is an attempt to reduce the requirements on the driver by encasing the fuel capsule in a hollow gold or uranium can called a hohlraum. Energy is deposited onto the hohlraum walls which heat up and re-emit the energy as soft x-rays. The x-ray energy bounces around the hohlraum walls so that the interior rapidly comes to equilibrium with a uniform temperature radiation bath. The soft x-rays drive the implosion of the capsule, potentially much more smoothly than direct drive because of the uniformity in the driving radiation bath. However, compared to direct drive, less energy is coupled to the capsule because of geometric losses and the efficiency of the conversion process from laser light to x-rays.

In fast ignition (16), the compression and heating processes are further separated

to reduce the requirements on the shock strength and symmetry. As before, the fuel shell is compressed by either a direct or indirect drive approach. With the cold fuel assembled in a highly compressed state, a high-power, short pulse laser generates a beam of relativistic electrons that drive the central hot spot. In one approach, the short pulse laser bores a hole in the capsule (17), in another the electrons are guided into the capsule by a metal cone (18).

ICF research is performed at a number of research facilities around the world. The NIF is the largest ICF facility in world. It was built to demonstrate an ignited plasma using the indirect drive approach. A similar facility for indirect drive, the Laser Megajoule, is under construction in France. Experiments relevant to direct drive and fast ignition are underway at facilities including the OMEGA and Omega-EP lasers at the University of Rochester, the GEKKO XII at the University of Osaka, and the Trident laser facility at Los Alamos National Laboratory (LANL).

1.3 High-energy density facilities

1.3.1 Laboratory for Laser Energetics

The majority of the experimental work presented in this thesis was carried out at the Omega Laser facility at the LLE, University of Rochester. OMEGA is the latest in a series of long-pulse laser facilities built at the University of Rochester with the goal of investigating direct drive ICF.

One of the University of Rochester's earliest successes in building a high-power, long pulse laser facility involved the creation go the four beam DELTA laser in the early 1970s (19). Like all of Rochester's later efforts, DELTA used neodymium-doped glass as the gain medium, which lases at the fundamental wavelength of 1.054 μm. The laser yield was 15-50 J/beam in a pulse duration of 100 ps. This facility allowed for diagnostic development (20), investigations of laser-plasma instabilities, and some

of the some of the first reported fusion neutron yields (21)

Following the success of DELTA came plans to build the larger, 24 beam OMEGA laser that could provide symmetric illumination of a laser fusion target. In 1977 a prototype beam line was created as the Glass development laser (GDL), followed by the first 6 beams of the Omega laser which began operation as ZETA in 1978. The Omega laser fired its first shot in 1980, delivering up to 1.75 kJ of 1 μm laser light in a 300 ps pulse (22).

ICF experiments in the 1980s demonstrated that there were significant problems with the lasers used to implode the capsules. These difficulties were related to the long wavelength of the laser light and the non-uniformities in the beam spots. The technology developed to solve these problems are essential to the experiments presented in this thesis.

1.3.1.1 Frequency conversion

At the high intensities ($I > 10^{14}$ W/cm^2) that are required to drive an ICF implosion, the laser light can couple nonlinearly to the plasma formed at the laser spot through laser plasma instabilities (LPI). Of the various interaction, stimulated Brillouin scattering (SBS) and stimulated Raman scattering (SRS) are perhaps the most serious. SBS and SRS both represent the scattering and coupling of laser energy into waves within the plasma. For SRS, the driven mode is an electron plasma wave while in SBS it is an acoustic wave. In the ICF context, the effect of SBS is to scatter the incident laser light away from the target, reducing the drive efficiency, while SRS can couple laser energy to the creation of a population of very high energy electrons. This both saps energy from driving the implosion and preheats the fuel, reducing the final compression.

Although the effects of these instabilities are determined by nonlinear saturation dynamics, the magnitude of these effects is correlated with the exponential growth

rate for small-amplitude modulations. This growth rate is proportional to the intensity and wavelength of the laser light as $I\lambda^2$. Experiments on the 1.054 μm Shiva laser at LLNL in the 1970s demonstrated the seriousness of the problem from LPI; up to 50% of the incident laser energy was converted to hot electrons or scattered light (4). To reduce this growth rate, either the laser intensity or the wavelength of the light must be reduced. The intensity is set by the amount of kinetic energy that is needed to drive the implosion. The solution was to decrease the wavelength through the use of a frequency doubling or tripling crystal.

The fundamental wavelength for Nd-doped phosphate glass of 1.054 μm can be converted to the second (0.527 μm) or third harmonic (0.351 μm) using a potassium dihydrogen phosphate (KDP) frequency conversion crystal (FCC). This nonlinear optics effect was first described by Franken and coauthors (23). In the context of high power lasers, work at the GDL in 1980 demonstrated conversion efficiencies of up to 80% of the incident laser light to the third harmonic (24). While the laser output is diminished, frequency tripling reduces the LPI growth rate by a factor of 9. Additionally, the shorter wavelength light is more strongly absorbed to drive the shocks to implode the capsule.

Frequency tripling has since become a mainstay of laser ICF research since the mid-1980s. In 1984, the 10-beam NOVA laser came online at LLNL with a yield of about 40 kJ in the UV. This was closely followed by the upgrade to the 24-beam Omega laser to UV light in 1985.

1.3.1.2 Beam smoothing

To successfully implode an ICF capsule it is critical that the driving laser beams have very little variation in the intensity over the laser spot. In practice, the laser amplifier and optics seed the beams with spatial non-uniformities. For direct-drive ICF, this spatial structure leads to areas of the capsule that are driven with much

higher intensities. This can seed the capsule with hydrodynamic instabilities, such as Rayleigh-Taylor, leading to much lower final compressions or breakup of the capsule. Indirect-drive ICF suffers from similar problems. The high intensities in the hot spots can create the same LPI that frequency-tripling was intended to overcome.

One component of this spatial structure is generated by nonlinear effects in the amplification process and inhomogeneities in the gain medium. The gain process of the laser amplifiers is strongly non-uniform. The Kerr effect is responsible for the modification of the index of refraction of a material in response to a strong electric field. High-powered laser light can induce a change in the refractive index n as (25)

$$n = n_0 + \gamma I \tag{1.12}$$

where a baseline index of refraction, n_0, is modified by an intensity, I, dependent term with a growth coefficient γ. Small perturbations in the laser intensity can grow exponentially through self-focusing. This leads to the creation of filamentary structures in the light intensity over the laser spot. At very high intensities, self-focusing can exceed the damage threshold of the focusing optics. A consequence is that laser facilities must limit the gain of the amplifiers. The energy of a laser facility may be increased only by building more beam lines or upgrading to larger aperture amplifiers.

Experiments on the 24-beam Omega laser found that near-field phase errors in the beam lines are magnified by the frequency tripling process (26). These phase errors are introduced from a number of sources including atmospheric turbulence, variations in amplification, and scattering from the focusing optics. They cause the emergence of hot-spots in the beam spot, much like the speckle pattern in a laser pointer.

Phase plates were developed at LLE to correct for the phase errors in the beams. The simplest phase plate configuration is called a random phase plate (RPP). These

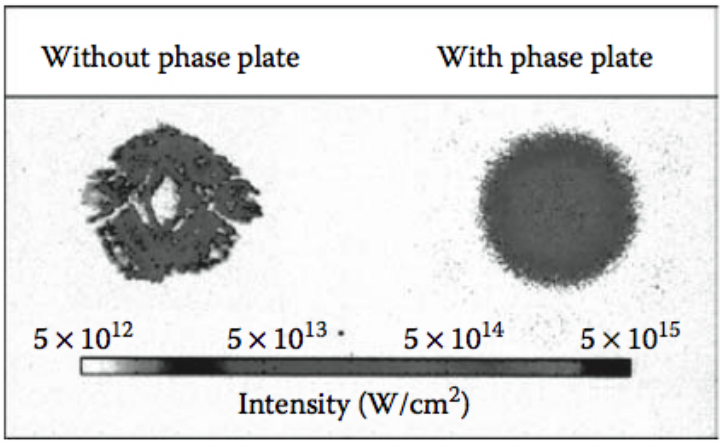

Figure 1.3: The use of random phase plate on the NOVA laser significantly reduced the large scale beam structure (4).

consist of a flat glass plate upon which are etched an array of hexagonal elements. The individual hexagons are randomly distributed between two levels that are π radians out of phase. The laser light enters the RPP and is broken into numerous packets, half of which lag the initial phase of the beam. The light is subsequently brought to a focus by the final focusing optic.

The smoothed beam spot is made up of the superposition of many thousands of the randomly phase delayed packets. The spatial structure from the beam is averaged from the interference of the packets. Figure 1.3 shows the results from implementation of this technique on the NOVA laser. The diffraction-limited focus from a beam smoothed with an RPP is an Airy pattern set by the dimensions of the hexagonal phases elements. Each phase plate is tailored to create a specific spot size. The high spatial frequencies from the vertices of the phase elements are poorly focused, so hexagonal RPPs create a six-spoked, star-like pattern around the central beam spot. Distributed phase plates (DPP) are a later refinement of this smoothing technique, where the spacing of the phase elements is adjusted to finely control the spatial profile of the laser spot (27).

Another beam smoothing technique that was developed at LLE is smoothing by

spectral dispersion (SSD) (28; 29). SSD is used in conjunction with phase plates to mitigate the high-frequency spatial noise that the latter imposes on the beam spot. Using only phase plates, the overall phase of the beam is recovered at the target plane from the interference of the many beam packets. However, small differences in the path length from the various phase elements tends to create small phase errors in the reconstruction of the beam. This generates high-frequency spatial variation in the laser spot. SSD mitigates this effect by eliminating the coherence and monochromaticity of the laser beam before it reaches the phase plate.

In SSD, a small amount of spectral bandwidth is introduced to the seed laser pulse by means of a electro-optical phase modulator and a pair of diffraction gratings. As before, the amplified and frequency converted laser beam is split up into a number of beam packets by a phase plate. When the beam is recombined at the target plane, the frequency variation between the beam packets cause the high-frequency speckle in the laser spot to vary in time. The frequency of the phase modulation is chosen so that the speckle varies much faster than the time scale of the hydrodynamic evolution of the experiment. The effects of speckle are thus reduced by being smoothed out over time. Since the efficiency of the frequency tripling process depends on a very precise alignment between the wavelength and the angle of incidence with respect to the FCC, the use of SSD entails a small drop in the maximum laser energy.

1.3.1.3 Omega laser facility

The OMEGA laser came online in 1995 as a replacement to the earlier 24 beam facility. It is a 60 beam laser system capable of delivering up 500 J/beam of 0.351 nm light in a 1 nanosecond pulse. Early experiments on OMEGA demonstrated a record fusion yield of 10^{14} DT neutrons (30), which was surpassed only recently by the ignition campaign on the NIF. The laser beams are uniformly distributed over the spherical target chamber to serve the primary research goal of direct drive ICF

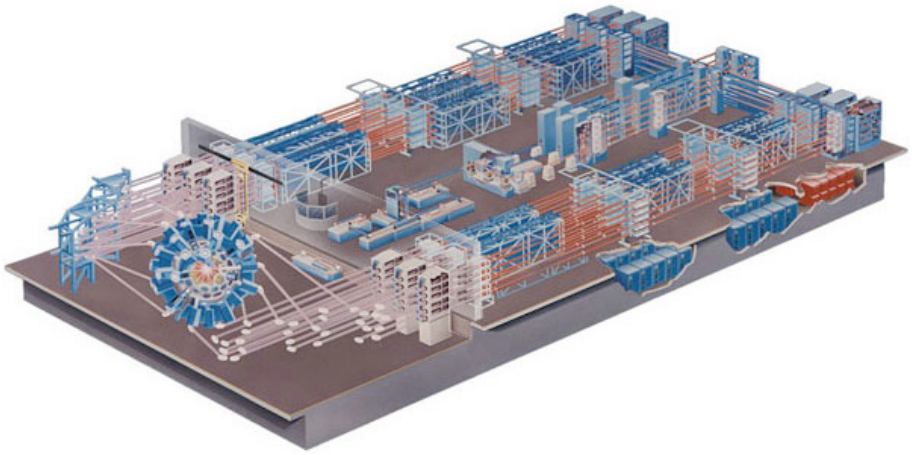

Figure 1.4: The OMEGA laser facility at the LLE

research. The flexibility afforded from this arrangement also serves a wide variety of high energy density physics (HEDP) experiments. Experimental shot days are awarded to outside researchers on a competitive basis by the National Laser Users' Facility (NLUF) program sponsored by the United States Department of Energy.

As it is a multipurpose facility, OMEGA possesses a wide variety of experimental diagnostics. These diagnostics are classified either as fixed to the target chamber or removable. Fixed diagnostics include a variety of cameras, spectrometers, and detectors for x-ray, visible light, and in some cases neutrons. Removable diagnostics tend to be more specialized and are generally developed to meet a specific experimental need. For each shot day, up to six removable diagnostics may be inserted into the target chamber through the use of a Ten-inch manipulator (TIM).

The TIM is a general-purpose insertion mechanism for removable diagnostics on OMEGA and other laser facilities. A diagram of the TIM is shown in Figure 1.5. The TIM consists of an airlock, an internal rail system, and a positioner with flexible bellows. To insert a diagnostic into the target chamber, it is first loaded into an external airlock on the TIM. After pumping the TIM down to vacuum, an internal airlock is opened to allow access to the chamber. The diagnostic is guided into the

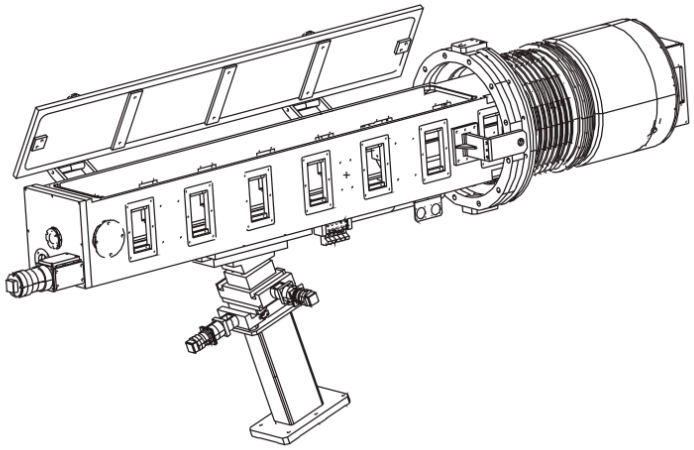

Figure 1.5: A schematic diagram of the Omega TIM. In this image, diagnostics are loaded into the airlock on the left and inserted into the chamber towards the right.

chamber by a set of rails and a lead screw. The final positioning of the diagnostic is done by translational stages on the TIM which permit precise movement along one rotational and three translational axes.

Many of the TIM-based diagnostics were developed by outside groups, notably LANL and LLNL. LLE maintains a qualification process for diagnostics, which emphasizes safety and compatibility with the existing target chamber layout. A significant portion of the work reported in this thesis concerns the design and implementation of a new TIM-based x-ray spectrometer for the OMEGA laser facility.

65t

1.3.2 Trident Laser Facility

The Trident Laser Facility is a kJ class laser system located at LANL. The laser has three beamlines which are split between the two (A & B) long-pulse and (C) short pulse beam. All three beams can be frequency doubled and one may be tripled. The A & B beams can deliver up to 200 J in 1 ns pulse, while the C beam's maximum yield is 100 J. The C beam can use chirped pulse amplification (CPA) to compress

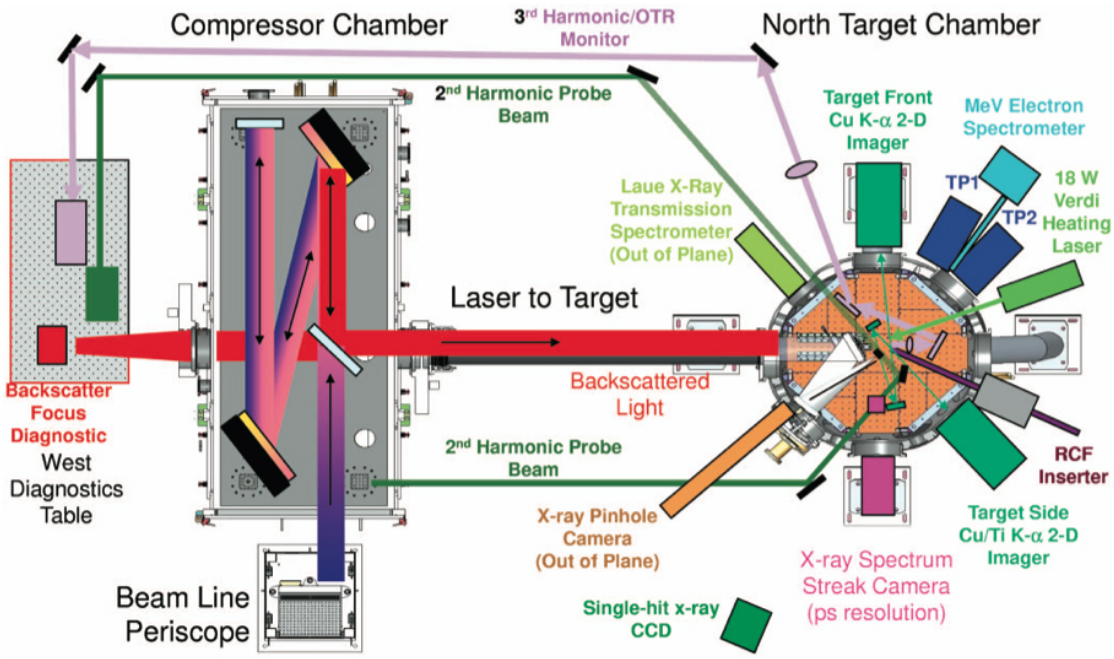

Figure 1.6: A diagram of the Trident north target chamber (31)

the duration of the laser pulse to less than 600 fs resulting in powers of over 200 TW. The Trident beams may be routed individually to either of the two available target chambers.

Experiments in the south target chamber typically use the long-pulse beams. Like much of the laser facility, the South target chamber was inherited from KMS Fusion. Unlike the North, the South target chamber can be used for experiments with targets that contain beryllium. Beryllium is an attractive material for HEDP experiments because it is largely transparent to x-rays and is an unreactive solid at room temperature. However, it is quite toxic and inhalation of beryllium dust can cause berylliosis, a chronic inflammation of the lungs. In work presented in this thesis, the concept of using one dimensional imaging to diagnose x-ray Thomson scattering was first demonstrated in an experiment on shock-compressed beryllium at Trident.

The IXTS diagnostic that forms the core of this thesis work was first tested on the North target chamber. The North target chamber is used primarily for short-pulse experiments and diagnostic development. It is fitted with an TIM , making it

compatible with many of the removable diagnostics from the OMEGA laser facility. Being a smaller scale facility, the presence of the TIM allows OMEGA diagnostics to be tested and refined over week-long campaigns without incurring the large expense of a shot day on OMEGA. The vacuum chamber itself was brought from LLE in the mid-1990s; it was originally the chamber for the now-decommissioned 24 beam Omega laser. The C-beam can be focused by an off-axis parabola to intensities on the order of 10^{20} - 10^{21} W/cm^2 (32).

1.4 Chapter summary

The introduction to this dissertation has discussed the motivation for studying astrophysically relevant matter in the lab. WDM is a particularly interesting physical regime where many of the theoretical descriptions break down and so it must be studied empirically. ICF research over the past fifty years has developed much of the technology that makes it possible to create these conditions in the lab. In chapter 2, I give an overview of the technique of laser-driven shock compression that may be used to create WDM in the laboratory. I include a discussion of the relevant physical scalings and a theoretical description of the fluid motion. The chapter concludes with a survey of the diagnostic techniques for characterizing these experiments in the lab. One of these techniques, x-ray Thomson scattering, forms the focus of this thesis. I give a theoretical description of x-ray scattering in dense plasmas in chapter 3. The various shortcomings of existing x-ray scattering instrumentation motivated the design and implementation of a spatially resolving spectrometer, the Imaging x-ray Thomson spectrometer (IXTS), which I detail chapter 4. The content in this chapter was originally presented as two articles published in the Review of Scientific Instruments (33) and the Journal of Instrumentation (34). Chapter 5 reports on the application of the IXTS to perform the first spatially resolved x-ray scattering measurement of a solid-density plasma. As of this writing, this work has been submitted

for publication. I conclude in chapter 6 with directions for future experimental work and a discussion of possible improvements to the IXTS. Appendix A discusses an experiment to measure the gain characteristics of an x-ray image intensifier, work which originally appeared in the Review of Scientific Instruments (35).

1.5 Acknowledgements and the author's role in this work

This work would not have been possible without the contributions of many individuals at the University of Michigan, Los Alamos National Laboratory, and the Laboratory for Laser Energetics, University of Rochester. The Trident experiments presented in Chapter 4 were performed in two campaigns in 2010 and 2011 by David Montgomery, John Benage, and the author. The data from these campaigns were analyzed by the author. The IXTS described in Chapter 4 was principally designed by the author and later refined by collaborators and engineering staff at Los Alamos National Laboratory including Sam Letzring, Frank Lopez, Paul Polk, John Benage, and David Montgomery. The IXTS was qualified for use at LLE with the assistance of Tim Duffy, Greg Pien, Bob Keck, Jack Armstrong, and others. The Omega experiment described in Chapter 5 was designed and principally carried out by the author in two shot dates in 2012. The experimental targets were designed by the author and fabricated at the University of Michigan by Sallee Klein, Robb Gillespie, and the author. On the shot days at Omega, Tom Sedillo and Scott Evans of LANL provided invaluable technical support. The analysis of these data is the work of the author, with invaluable scientific contributions from Katerina Falk, R Paul Drake, Paul Keiter, John Benage, and David Montgomery. The x-ray scattering code used to interpret the scattering data was created by Gianluca Gregori at the University of Oxford and improved upon by Carsten Fortmann while at LLNL.

CHAPTER II

Blast wave physics

2.1 Introduction

In this chapter, I describe the potential of creating shocks in the laboratory to access WDM conditions. I start with the challenges in describing these states of matter in terms of self-consistent thermodynamic variables. I then introduce the fluid conservation laws and derive the jump conditions that describe a hydrodynamic shock. I use these relations to estimate orders of magnitude for the material conditions that are accessible in laser experiments. I close the chapter with an overview of diagnostic techniques for diagnosing these experiments and the associated limitations that motivated the implementation of imaging x-ray Thomson that I discuss in later chapters.

When energy is very rapidly introduced into a fluid, it can create a transient discontinuity within the fluid. The discontinuity forms because the energy is deposited faster than the timescales over which the bulk of the fluid can react, typically the fluid scale length divided by the local speed of sound. This leads to the formation of a steep increase in the fluid pressure, density, and temperature at a traveling interface called a shock. Shocks are not typical part of everyday experience, but are nonetheless a fairly common phenomenon. The sound from a thunderclap, a knocking car engine, or cracking your knuckles (36) are all examples of a type of shock called a blast wave

which forms after the release of a sudden (and finite) amount of energy.

Blast waves are common in the astrophysical setting, found in phenomenon such as supernovae, colliding galaxies, and the formation off stars. The energy imparted by the shock often entails a significant amount of heating and compression. In the laboratory, we can drive shocks with short (nanosecond), high-energy (kJ) laser pulses to access material conditions similar to those found in these violent astrophysical events. While diagnosing these transient states is challenging, shocks can create pressure regimes far in excess of what is possible in static experiments such as diamond anvil cells.

2.2 Equations of state

An EOS describes a relationship between two or more thermodynamic state variables, such as pressure, temperature, or enthalpy. Much of the technology we take for granted depends on detailed knowledge of the EOS of materials. For example, the EOS of some metals like steel or plutonium can be very complex with many different crystalline phases giving rise to a diverse set of physical properties. An incorrect application or understanding of a material EOS can lead to catastrophic failure, such as the collapsing of various cast-iron railway bridges in late 19th century Britain.

In the HEDP context, the equation of state of most astrophysically-relevant materials is poorly known. Part of the difficulty is that only tiny amounts of these extreme material states can be created in the laboratory, often for only a few nanoseconds at a time. Nevertheless, an accurate understanding of the EOS is essential to correctly modeling the dynamics of experiments in the lab and therefore predicting the properties of astrophysical objects.

2.2.1 Ideal gas law

One of the simplest EOS, the ideal gas law, is useful for approximating the behavior of many weakly-coupled, non Fermi-degenerate systems. For an ionized plasma in which the electrons and ions have the same temperature, one can write this as

$$P = \frac{\rho(1+Z)k_bT}{Am_u}. \tag{2.1}$$

This is a relationship between the material pressure P, density ρ, average ionization Z, and temperature k_bT where Am_u is the average atomic weight of the matter.

In many HEDP experiments, intense laser irradiation creates a shock or other related phenomenon which moves much faster than the sound speed, c_s. Energy is slowly lost to the environment through thermal diffusion, with fluxes progressing at some fraction of c_s. Therefore, we can approximate the experiment as an adiabatic process in a closed system. For any adiabatic process, the following relationship holds

$$\frac{P}{\rho^\gamma} = \text{Constant} \tag{2.2}$$

where the ratio of specific heats, $\gamma = C_p/C_v$, is the adiabatic index. The specific internal energy ϵ of the gas is related to the pressure-volume work as

$$\frac{P}{\rho} = \epsilon(\gamma - 1). \tag{2.3}$$

which defines another EOS for an adiabatic ideal gas.

2.2.2 Tabular equation of state

The discontinuity in the material conditions across a shock means that matter may straddle a range of conditions over which no single EOS is applicable. For example, a solid irradiated by a laser may be Fermi degenerate upstream of the shock, very

nearly an ideal gas in the ablated plasma, and a WDM state in the shock for which no analytical EOS relation exists.

Tabular equations of state are constructed as an array of equilibrium values of state variables that is compiled over a wide range of parameters. These values generally come from some combination of experimental data and theoretical estimates from numerical simulations or analytical models. The speed and flexibility of EOS tables makes them useful for hydrodynamic simulation codes used to model experiments and ultimately predict the nature of astrophysical objects and processes.

The SESAME Equation-of-state library (37), developed by LANL, is a tabular EOS database that is commonly used in the HEDP community. The tables are computed using a semi-empirical approach where theoretical models are chosen to agree with the available experimental data. The models are then used to interpolate the EOS values between these data points.

This approach may become problematic for HEDP conditions because of the paucity of experimental data that can be used to to validate the theoretical models. Furthermore, the correct theoretical approach to modeling the EOS in WDM is an active area of research. The interpolated EOS values are not necessarily thermodynamically consistent, especially in the transition region between models (15).

Many materials used in HEDP and ICF experiments are absent from EOS tables because of a lack of experimental data. This is particularly an issue for porous materials, such as foams, where the crushing of the internal microstructure can affect the passage of a shock. Therefore, experiments to measure the EOS of materials are essential to improve the SESAME tables and the validity of the predictions from hydrodynamic codes.

2.3 Fluid conservation laws and the equations of motion

Any fluid disturbance must fundamentally follow the Euler equations of motion. In the differential form, these equations describe the conservations of mass, momentum, and energy in the fluid. The first is the continuity equation for mass

$$\frac{\partial \rho}{\partial t} + \nabla \cdot (\rho \mathbf{u}) = 0 \tag{2.4}$$

where ρ is the fluid density and $\mathbf{u}$ is the fluid velocity. The second is the equation of motion of the fluid, which is simply Newton's second law

$$\rho \left(\frac{\partial \mathbf{u}}{\partial t} + \mathbf{u} \cdot \nabla \mathbf{u} \right) + \nabla P = 0 \tag{2.5}$$

with P as the pressure of the fluid. The final relation is the energy equation

$$\frac{\partial}{\partial t} \left(\frac{\rho \mathbf{u}^2}{2} + \rho \epsilon \right) + \nabla \cdot \left(\rho \mathbf{u} \left(\epsilon + \frac{\mathbf{u}^2}{2} \right) + P \mathbf{u} \right) = 0 \tag{2.6}$$

where ϵ denotes the specific internal energy of the fluid. Each of the preceding equations is equivalent to a continuity equation of the form

$$\frac{\partial \rho_Q}{\partial t} + \nabla \cdot \Gamma_Q = 0 \tag{2.7}$$

where Q is some conserved quantity with a volume density ρ_Q and a flux of Γ_Q in the absence of any sources or sinks. By integrating over a Gaussian pillbox, it can be shown that the preceeding continuity equation implies that the fluxes entering and leaving any point must be equal.

$$\Gamma_Q(x_1) - \Gamma(x_2) = 0 \tag{2.8}$$

where x_1 and x_2 denote positions on either side of the pillbox.

A shock represents an sudden discontinuity in fluid parameters such as density, pressure, and temperature. Nevertheless, the fluid quantities are still conserved across the shock "jump." If we construct our pillbox across the shock, we can use Eq. 2.8 to rewrite the Euler equations as 1D shock jump conditions. In a frame moving such that the shock front is at rest, this yields

$$\rho_1 \mathbf{u}_1 = \rho_2 \mathbf{u}_2 \tag{2.9}$$

$$\rho_1 \mathbf{u}_1^2 + P_1 = \rho_2 \mathbf{u}_2^2 + P_2 \tag{2.10}$$

$$\rho_1 \mathbf{u}_1 \left(\epsilon_1 + \mathbf{u}_1^2\right) + P_1 \mathbf{u}_1 = \rho_2 \mathbf{u}_2 \left(\epsilon_2 + \mathbf{u}_2^2\right) + P_2 \mathbf{u}_2 \tag{2.11}$$

In these equations, quantities with a subscript of 1 are taken ahead, or upstream, of the shock while those with a subscript of 2 are behind or downstream. In the laboratory, we apply a large backing pressure P_2 to create a shock which moves with $u_2 >> u_1$, $\rho_2 > \rho_1$ and $\epsilon_2 >> \epsilon_1$.

2.4 Interaction of solids with high-power lasers

A variety of methods are used to create this backing pressure, including explosives, gas guns, flyer plates, and lasers. For visible light lasers at intensities of $10^{14} - 10^{15}$ W/cm^2, the predominant absorption mechanism is inverse bremsstrahlung. The intense electric field of the laser light oscillates the electrons. At high densities, a free electron may oscillate over some part of its cycle to be accelerated towards an ion. The electron can then scatter, crucially imparting some momentum to the heavy ion. In contrast to the absorption of a photon by a free electron, the momentum transfer allows the electron to absorb the photon as the interaction conserves momentum. After a few such interactions, the electron eventually has enough energy to liberate another electron into the continuum which can in turn absorb more energy from the

laser. This leads to the growth of a significant free electron population in a process called avalanche ionization.

The ionization will continue until the electron plasma frequency becomes equal to the frequency of the laser light. At this point, the plasma will become a very efficient reflector of the incident light. Since the plasma frequency is a function of only density, this condition is equivalent to reaching a critical density, n_c such that

$$n_c = 1.1 \times 10^{21}/\lambda^2. \tag{2.12}$$

Where the critical density is expressed in cm^{-3} and the wavelength of the light is in μm.

A solid undergoing laser irradiation will rapidly form this reflecting critical surface. To reach the critical surface, the light must first pass through a volume of lower density plasma. In this underdense region, the laser energy is absorbed through inverse bremsstrahlung. Since inverse bremsstrahlung is a collisional process, higher density plasmas are more efficient at extracting light energy, which provides an additional motivation for using short-wavelength light.

The radiation pressure from the laser is generally insignificant, so the ablated plasma will stream away from the critical surface. At moderate laser intensities, this plasma may heated to several keV. The hot, ablated plasma acts much like a rocket exhaust, creating a tremendous inward pressure which can drive a shock in the material.

Using dimensional analysis we can estimate the scaling of this interaction on the various physical parameters (4). The pressure created from this ablation is equal to the momentum flux from the critical surface.

$$P_{abl} = \rho \dot{x}^2 \propto n_c c_s^2 \tag{2.13}$$

where a reasonable velocity scale is, c_s, the sound speed of the material at the critical surface. The laser at some intensity I deposits energy onto the critical surface, heating it so that $I \propto k_B T n_c c_s$. Assuming that the electrons are an ideal gas, we have $c_s^2 \propto k_B T/m_e$. Using these two relations, we can eliminate the temperature dependence in Eq. (2.13). The ablation pressure is then

$$P_{abl} \propto I^{\frac{2}{3}} n_c^{\frac{1}{3}} = I^{\frac{2}{3}} \lambda^{\frac{-2}{3}} \tag{2.14}$$

For P_{abl} in Mbar, I in 10^{14} W/cm^2, n_c in cm^{-3} and λ in μm, a more exact solution will have a constant 8 on the right hand side (15). Even with modest intensities of a few 10^{14} W/cm^2, pressure on the order of tens of megabars may be created in the laboratory. This is a consequence of the enormous energy flux from the focused laser beam.

2.4.1 Shock compression

For a given backing pressure we can solve the jump conditions for the density ratio between the upstream and downstream fluids. In laser driven shocks, the downstream pressure is typically on the order of tens of megabars while the upstream pressure is substantially smaller. Hot electrons or x-rays from the drive surface may be able to preheat the upstream fluid to temperatures of a few eV, but the resulting thermal pressure is only a few tens of kilobars. This limit of $P_2/P_1 >> 1$ is called the strong shock limit. This permits us to write the density ratio as

$$\frac{\rho_2}{\rho_1} = \frac{\gamma + 1}{\gamma - 1} \tag{2.15}$$

which only depends on the adiabatic index (15). At first it may seem strange that the compression behind a shock is a material characteristic and is independent of the pressure driving the flow. However, the implication is that the shock is a self-

regulating system.

According to the first law of thermodynamics, an adiabatic process must have

$$dU + \delta W = \delta Q = 0 \tag{2.16}$$

where dU is the change in internal energy of the system and δW is the work done by the system. Since P/ρ^γ must remain constant for an adiabatic process, the added pressure driving the shock does work on the fluid, compressing it to a higher density. The work done by the system is simply $\delta W = PdV$, which I express using the ideal gas law as

$$PdV = -\frac{(1+Z)}{Am_p}\frac{k_B T}{\rho}d\rho. \tag{2.17}$$

Assuming a constant ionization across the shock, if the density and pressure increase the fluid must react by increasing its temperature. The temperature rises until the thermal pressure from the shock heated fluid can counterbalance driving pressure. The density thus reaches an equilibrium state where further pressure will only increase the temperature.

The only way to raise the shock compression is to put the PdV work into modes that do not increase the temperature. The adiabatic index is related to f, the number of degrees of freedom of its constituents, by

$$\gamma = 1 + 2/f \tag{2.18}$$

A monoatomic, ideal gas will have three translational degrees of freedom for $\gamma = 5/3$ and a maximum compression of 4. If the shock sufficiently heats this gas, the atoms will begin to ionize. This creates an additional degree of freedom, which will decrease γ and increase the peak compression. In an alternate description, the shock

can now dump PdV work into the ionization term in Eq. (2.17). This lowers the temperature so that the system responds by increasing the density to reestablish balance with the driving pressure. Very hot shocks may lose a significant amount of energy through radiation. This permits the downstream fluid to cool and achieve very high compressions. For example, compressions of 40 times were inferred in experiments that produced radiation-dominated shocks in xenon gas (38).

2.4.2 Shock heating

The work done compressing the fluid is $P_2/\rho_2 - P_1/\rho_1 \sim P_2/\rho_2$ in the strong shock limit. Using Eq. (2.9) and (2.10), this becomes

$$\frac{P_2}{\rho_2} = u_2(u_1 - u_2) \tag{2.19}$$

By Eq. (2.9) the ratio u_2/u_1 is the inverse of the compression ratio of Eq. (2.15). We can eliminate the downstream velocity and use the ideal gas law to write the temperature in the shock as

$$k_B T = \frac{A m_u}{1+Z} \frac{\gamma - 1}{\gamma + 1} \frac{2}{\gamma + 1} u_1^2. \tag{2.20}$$

For a laser driven shock in a low-Z plasma, we might have A=6, Z=2, γ=5/3, and $u_1 \sim 50$ μ/ns. These values correspond to a temperature of about 10 eV or on the order of 100 000 K. Therefore, shock heating can easily put matter into temperature regimes that are similar to the interiors of giant planets or stars.

2.5 Blast waves

The description so far has been of a steady shock that is supported by some constant source of pressure. In laboratory experiments and in the cosmos these pressure

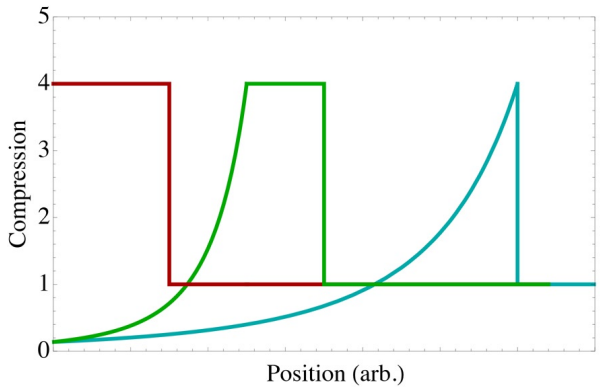

Figure 2.1: A steady shock (red) is initially supported by a pressure source incident from the left. After the pressure source is removed a rarefaction wave propagates from the left, relaxing the shocked material (green). The rarefaction eventually catches up with the shock to form a blast wave (blue).

sources are most often transient, limited in time by either the finite duration of a laser pulse or the sudden release of energy from a supernova. Once the pressure source is removed, the material behind the shock can no longer be supported in its compressed state. The post-shock fluid relaxes to a lower density, flowing outward from the initial interface. This is known as a rarefaction wave and it progresses through the shocked fluid until it catches up to the discontinuity from the shock. After this point, the shock and rarefaction wave travel together as a blast wave. This process is shown schematically in Figure 2.1.

2.5.1 Self-similar solutions

While there is considerably more spatial structure in blast waves as compared to steady shocks, we may still analyze their behavior with the fluid conservation laws. By grouping the physical parameters of the system into dimensionless quantities called similarity variables, the set of partial differential equations of (2.4) - (2.6) may be reduced into a set of ordinary differential equations of the similarity variables, which are more easily solved. The profiles of the parameters of interest are then extracted

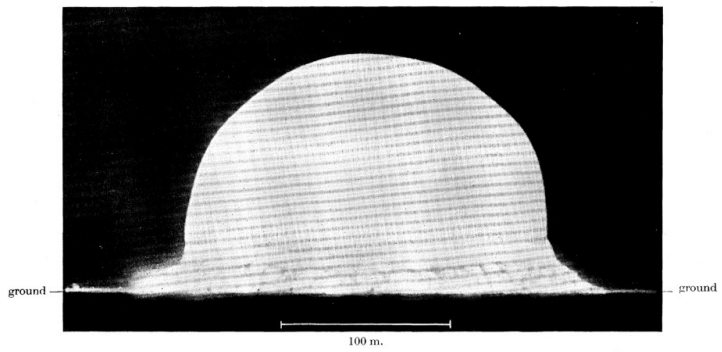

FIGURE 7. The ball of fire at $t = 15$ msec., showing the sharpness of its edge.

Figure 2.2: The Trinity nuclear test created a well-defined blast wave in the early stages of the explosion. The gas in the shock is heated to incandescence, saturating the photograph. Reproduced from (39)

from the similarity variables.

This approach was first used by Taylor (40) to estimate the explosive yield of the Trinity nuclear test of 1945 based on publicly available photos of the explosion (39). The only measurement needed was the radius of the blast wave at a known time, as is illustrated in Figure 2.2. In Chapter V, I use this technique to analyze the spatial density profile of the blast wave in the experiment.

2.6 Hugoniot equations

In the preceding discussion, we have been working in an inertial frame in which the shock is at rest. In this "shock frame", the upstream fluid streams into the shock at a velocity of $-u_1$ while the downstream fluid leaves at a velocity u_2. This is contrast to the "laboratory frame" in which experiments are usually observed where the upstream fluid is at rest and the shock proceeds at a velocity u_1.

In the laboratory frame the downstream, or post-shock, fluid velocity, is simply

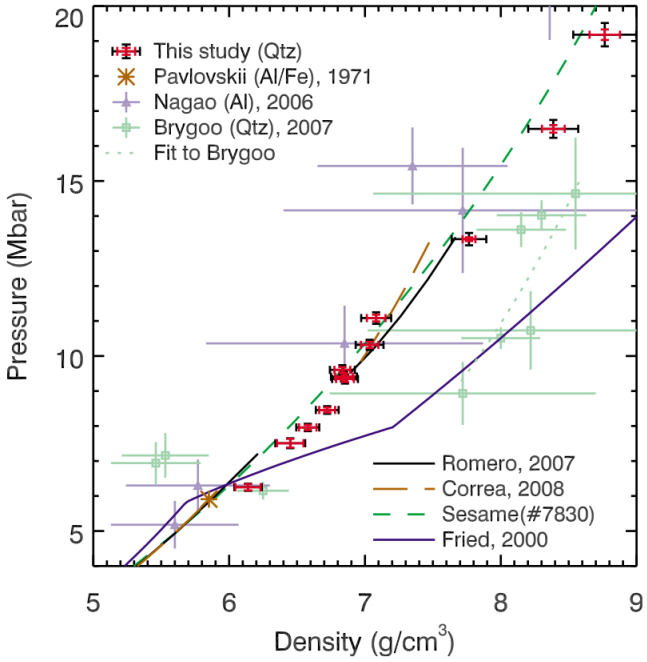

Figure 2.3: A comparison of experimental measurement on the shock Hugoniot of carbon (points) to EOS models (lines) (41).

$u_p = u_1 - u_2$. We can rewrite Eq. (2.4) - (2.6) in the laboratory frame as

$$\frac{\rho_2}{\rho_1} = \frac{u_1}{u_1 - u_p} \tag{2.21}$$

$$P_2 - P_1 = \rho_1 u_1 u_p \tag{2.22}$$

$$P_2 u_p = \rho_1 u_s (\tfrac{1}{2} u_p^2 + \epsilon_2 - \epsilon_1). \tag{2.23}$$

Experiments are prepared so that the upstream fluid conditions are well characterized. Therefore, we have a set of three equations and five unknowns. By measuring any two of $\rho_2, u_1, u_p, P_2, \epsilon_2$, we can solve for the others.

The velocity may be eliminated from this set, yielding the Hugoniot equation

$$\epsilon_2 - \epsilon_1 = \tfrac{1}{2}(P_2 + P_1)(v_1 - v_2) \tag{2.24}$$

where $v = 1/\rho$ is the specific volume. This equation defines the Hugoniot curve, a path along pressure-volume space that is accessible through the action of a single shock. Through a choice of an equation of state, relating ϵ to P and v, we may plot this curve.

Figure 2.3 shows a plot from (41) summarizing an experiment to measure the shock Hugoniot of carbon that is initially in the diamond phase. The experimental data points are compared to various numerical calculations of the EOS for carbon. The EOS models are generally in good agreement with the data in this regime, which the authors ascribe to a coexistence of carbon in the diamond, liquid, and the BC8 phases over this pressure range.

2.7 Measurement techniques for EOS experiments

This section presents a brief overview of some of the methods used in EOS experiments. This list is not intended to be comprehensive, but to illustrate the difficulties with existing methods that motivated the development of the IXTS diagnostic.

2.7.1 VISAR and SOP

Shocks in transparent material can be probed with optical instrumentation. On the Omega laser facility, the Velocity Interferometer System for Any Reflector (VISAR)(42) and the Streaked optical pyrometer (SOP)(43) are two diagnostics that are often used in tandem to measure shock velocity and temperature. When a transparent material is subject to a shock, the material in the shock is heated and compressed into an overdense state. A critical surface forms in front of the shock, which readily reflects and emits light as a blackbody. Since the upstream material is still transparent light can escape and be measured to provide information on the state of the shock.

VISAR (44) relies on measuring the Doppler shift of a low power, visible light laser beam that is reflected from the shock. The resulting phase shift between incident and

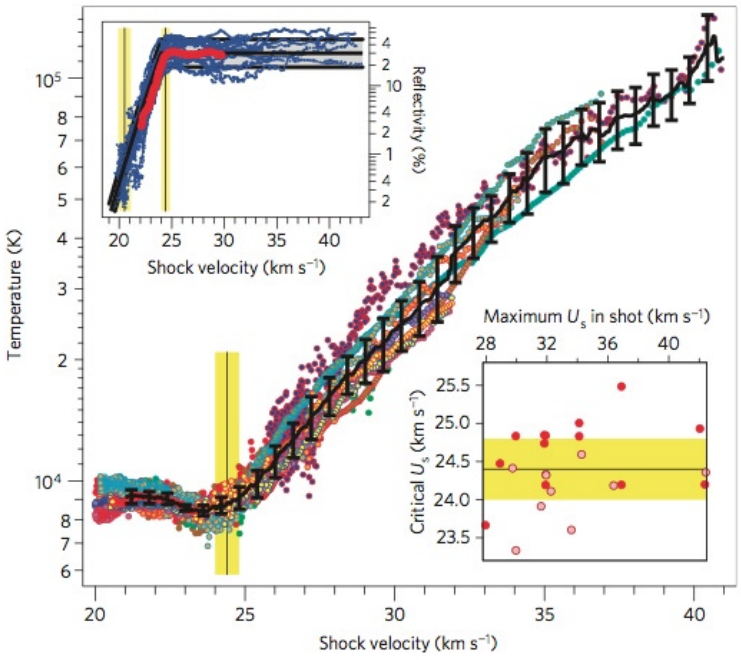

Figure 2.4: A plot of the shock velocity against the temperature for shock compressed diamond, from (45)

reflected beams is found by comparing the shift in the interference patterns after a finite optical delay. The shock velocity is then calculated by counting the number of fringe shifts and using an absolute calibration between fringe shift and velocity. The interferograms are streaked in time to measure accelerations of the shock front.

The heated material in the shock front emits radiation as a black body. The SOP measures the self-emission of light from the shock over a narrow optical bandwidth. Through comparing the intensity of this emission to Planck's law, the blackbody temperature may be inferred. The emission is streaked in time, so that the temperature of the shock front is also time-resolved.

Since VISAR and SOP are both resolved in time, they can provide extended measurements of the shock velocity and temperature over the range of conditions that are accessible by an accelerating shock front. Figure 2.4 reproduces a plot from Eggert et al (45) of the properties of diamond compressed by a blast wave (45). The high-temperature, high-pressure points are data taken early in time. As the shock

propagates and dissipates its internal energy, the velocity and temperature decrease. This combined technique has been used on experiments for characterizing various other transparent materials including deuterium (46; 47), plastic (48; 49), magnesia (50), and lithium fluoride (51).

2.7.2 Impedance matching

A material in which the EOS is known to a high degree of confidence can be used to infer the properties of another material in which the EOS is less certain through the impedance matching technique (52; 53; 54; 48). A steady shock is driven in a slab of some well characterized material, often aluminum (55) or quartz (56). A thin section of a second material of interest is attached to the rear of the first. The pressure from the first shock drives another shock in the second material. By measuring the velocities of these two shocks and using the known EOS to infer the downstream pressure in the first material, the fluid equations (2.4) - (2.6) can be solved for the particle velocity in the second material. The EOS of the second material can then be defined by the Hugoniot equations.

The shock velocities can be measured by looking at the breakout of the shock from a stepped target. The shock front itself is a blackbody which can be quite bright, but is often surrounded by cold, opaque material so that this light does not escape. Once the shock reaches the end of its propagation medium, it "breaks-out" into vacuum and the emission from the shock is visible. By including steps of known thickness in the shock propagation direction, the shock velocities can be measured using a time-resolved streak camera.

2.7.3 Time-resolved x-ray absorption spectroscopy

In an ion, the binding energy of the innermost K-shell electron is dependent not only on the attraction from the nucleus but also the screening charge from the re-

maining spectator electrons. For a neutral atom, this binding energy is called the K-edge. In a plasma, as the outer electrons are ionized away, the screening effect diminishes and the K-edge shifts to higher energy. Measuring the K-edge shift can reveal the ionization state of the plasma. With the assumption that the ions are at equilibrium, the EOS of the material can be used to relate the ionization state to the plasma temperature.

In experiments that utilize x-ray absorption spectroscopy, the level shifts are observed in the plasma either directly or by introducing a heavy dopant. The plasma is illuminated by a broadband x-ray source, which is strongly absorbed by the plasma at the K-edge. The transmitted spectrum shows absorption bands at energy levels characteristic of the ions. It is recorded by a time-resolved spectrometer and may be analyzed to extract the K-edge shifts indicative of the ionization state.

Absorption spectroscopy has typically been limited to experiments to characterize very low-density foams (57; 58; 59) or a thin (50 μm) section of solid plastic (60). The ideal x-ray source is a broadband continuum which lacks any features in the spectral region around the K-edge of interest. The ability to probe denser materials is limited by the availability of appropriate broadband x-ray backlighters above a few keV. This has motivated studies of M and L-shell emission from high-Z materials such as cesium iodide and uranium, which are useful up to about 6 keV (61). Denser materials require higher x-ray energies which mean they are currently out of reach for this technique.

2.7.4 X-ray Thomson scattering

Since the experiments of Compton (62), observing the spectrum of scattered radiation has been a fundamental technique to measure the physical parameters of dense matter. In the simplest description, incident x-rays scatter from the electrons in a sample. The scattering process may lead to an energy transfer between the x-rays

and electrons. Therefore, the scattered spectrum reflects an averaged microscopic or thermodynamic state of the system. In the high-energy density physics context, XRTS was first proposed as a method to diagnose solid-density plasmas by Landen (9) and given an extensive theoretical description by Gregori (63).

XRTS has been applied to characterize isochorically heated matter. Glenzer (64) first demonstrated using XRTS to diagnose a HEDP system in an experiment on radiatively heated beryllium. In later experiments, laser compression was used to drive a steady shock, creating a quasi-homogenous plasma which was probed with time resolution. Kritcher used an ultrafast x-ray probe (65; 66) on experiments to characterize shocked lithium hydride. Time gated x-ray framing cameras were used in experiments to diagnose shock compression of various materials relevant to ICF including plastic (67), beryllium (68) and deuterium (69). XRTS has also been demonstrated on laser heated hydrocarbon gasbags (70) and carbon foams heated by irradiation from soft (71) and hard x-rays (72).

The experiments of Visco (73) showed that the spatial profile of a shock could be built up over multiple shots by viewing the plasma through a narrow slit and varying the time gating. The spatial resolution of this approach is limited as the signal quality competes with the spatial resolution through the width of the viewing slit. The absolute position of the blast wave was predicted based on one-dimensional modeling and so was subject to a systematic uncertainty. Later experiments incorporated a secondary diagnostic to track the position of the shock in time (74).

2.8 Conclusion

Having defined the diagnostics that are available for EOS measurements in the laboratory, we are left with the observation that none of these techniques are easily applicable to diagnosing a blast wave in an optically thick medium. VISAR and SOP would be ideal, yet they can only be applied to the case in which the upstream

material is transparent. Impedance matching is well suited to optically thick materials. However, this technique is only applicable to thin samples driven by steady shocks. Variations in the shock speed greater than 1% create large uncertainties in the particle velocity (15). Absorption spectroscopy is limited by the unavailability of a several-keV broadband backlighter/dopant pair to overcome the photoattenuation from dense plasmas. Finally, XRTS has been applied mostly to systems that can be approximated as isochorically heated and compressed, but by definition a blast wave entails significant spatial structure.

In the present work, I report the development of an imaging spectrometer for use in diagnosing spatially inhomogenous plasmas via XRTS. A toroidally curved, perfect Ge crystal affords high spatial resolution within a large field-of-view combined with spectral resolution that is an order of magnitude higher than is available with more commonly used mosaic-crystal spectrometers. I applied this method in an experiment to characterize the spatial profiles of the density, temperature, and ionization state in an inhomogeneous plasma flow.

CHAPTER III

Theoretical description of x-ray Thomson scattering

This chapter is presents an overview of the theory of x-ray scattering as applied to dense plasmas. The x-ray scattering spectrum is described in terms of a dynamic structure factor. This concept connects the correlations between the motions of the particles in the plasma and interference between the scattered wavefronts. Described next are the possible x-ray scattering processes and their relative contributions to the scattered spectrum. Measuring the scattered spectrum is presented as the basis for diagnosing HEDP plasmas through XRTS.

3.1 Introduction

For the physical system considered in this work, the strongest x-ray scattering processes are elastic Thomson scattering and inelastic Compton scattering. Thomson scattering is a classical process which is analogous to Rayleigh scattering of visible light. The photon energy is conserved in the scattering process. In contrast, Compton scattering requires a quantum mechanical picture where the scattered photon loses some of its initial energy to a recoiling electron. The scattered x-ray is downshifted in energy by amount equal to the Compton shift. In the HEDP community, these two

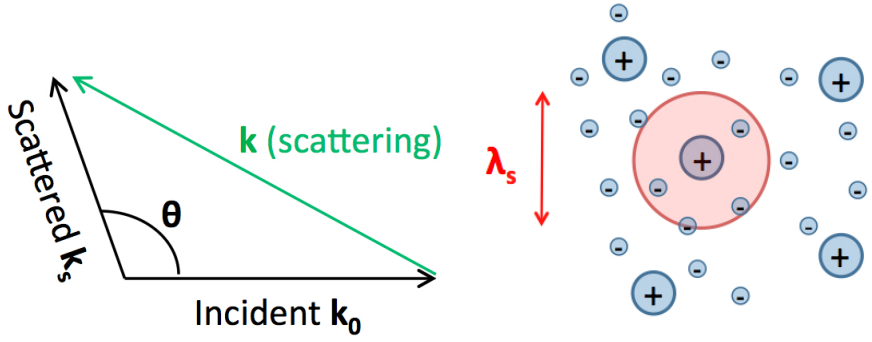

(a) (b)

Figure 3.1: (a) In x-ray Thomson and Compton scattering, an incident photon with wavenumber k_0 is scattered through an angle θ. (b) The scattering regime is determined by x-ray probe wavelength relative to the plasma screening length λ_s.

processes are often collectively called x-ray Thomson scattering given the fact that elastic Thomson scattering is simply inelastic Compton scattering in the limit of zero energy transfer.

Consider the Compton scattering process, as shown diagrammatically in Figure 3.1. An incident x-ray with a wave vector k_0 interacts with a free electron. The x-ray is scattered over an angle θ to a new wave vector k_s. In the process, the electron absorbs a recoil momentum $\hbar\mathbf{k} = \hbar\mathbf{k_0} - \hbar\mathbf{k_s}$ and energy $\hbar\omega = \hbar\omega_0 - \hbar\omega_s$.

The domain of the scattering interaction is usually expressed through the dimensionless scattering parameter

$$\alpha = \frac{1}{k\lambda_s}. \tag{3.1}$$

Here λ_s is the scale length for the screening of the electric fields in the plasma. This is the Debye length for a classical plasma and the Thomas-Fermi length for a degenerate plasma. For $\alpha > 1$, the size of the scattering interaction is larger than the length scale of the collective oscillations of the electrons. This is called collective scattering because the x-rays are scattered from the combined motions of the electrons through

various plasma waves. In the non-collective limit of $\alpha < 1$, the x-rays may penetrate the plasma waves and scatter from the motion of the individual electrons.

The energy exchanged between the photon and the electron in Compton scattering may be derived using an argument based on the conservation of momentum and energy. I write the formula for the energy shift as

$$\hbar\omega - \hbar\omega_0 = -\frac{\hbar^2}{2m_e}\mathbf{k^2} + \frac{\hbar}{\mathbf{m_e}}\mathbf{k}\cdot\mathbf{p} \tag{3.2}$$

here the initial momentum of the electron is written as $\mathbf{p}$. The first term is the well known Compton shift, which is equal to

$$E_C = \hbar\omega_0\left(1 - \frac{1}{1 + \hbar\omega_0/m_e c^2(1-\cos\theta)}\right). \tag{3.3}$$

The second term accounts for the Doppler broadening of the downshifted photon from the initial motion of the electrons. Therefore, the inelastic scattering gives rise to a Compton peak that is downshifted in energy and Doppler broadened by the momentum distribution of the electrons.

This last detail hints at the power of spectrally resolved, non-collective x-ray scattering. For an ensemble of free particles, the velocity of the particles is distributed according to a thermodynamic average of the available energy states. The broadening of the Compton profile depends on the Hamiltonian of the particles, which may reveal ensemble parameters such as density and temperature. For bound electrons, the velocity is found through solving the Schrödinger equation in momentum space. Therefore, the inelastic spectrum reflects the energy levels of the bound state.

3.2 Elastic scattering

For simplicity, consider scattering from a single atom containing two electrons separated by a vector $\boldsymbol{r}$. Photons are elastically scattered, changing the wavenumber according to $\boldsymbol{k} = \boldsymbol{k_0} - \boldsymbol{k_s}$. The two scattered wavefronts will interfere depending on the phase difference introduced by their separation. We may write the amplitude of the scattered wave as

$$A(\boldsymbol{k}) = A_0 e^{-i\boldsymbol{k}\cdot\boldsymbol{r}} \tag{3.4}$$

where A_0 is the scalar amplitude of the indent wavefront. For a collection of electrons distributed in a charge cloud surrounding an atom, we must consider all possible separations $\boldsymbol{r}$ weighted by the charge distribution function $\rho(\boldsymbol{r})$. The scattered amplitude becomes

$$A(\boldsymbol{k}) = A_0 \int \rho(\boldsymbol{r}) e^{-i\boldsymbol{k}\cdot\boldsymbol{r}} d^3\boldsymbol{r} \tag{3.5}$$

$$= A_0 f(\boldsymbol{k}) \tag{3.6}$$

The integral term is called the atomic form factor, which describes the amplitude of scattering of wavenumber $\boldsymbol{k}$ from an isolated atom. This is a characteristic parameter of matter which is tabulated for the various chemical elements.

For a collection of N identical atoms, the scattering amplitude must then be summed over the various positions, r_i, of the atoms.

$$A(\boldsymbol{k}) = \sum_{i=1}^{N} A_0 f(\boldsymbol{k}) e^{-i\boldsymbol{k}\cdot\boldsymbol{r_i}} \tag{3.7}$$

The intensity on the detector is then the product of the amplitude of the scattered

wave with its complex conjugate.

$$I(\boldsymbol{k}) = A(\boldsymbol{k})A(\boldsymbol{k})^* = |A_0|^2 f(\boldsymbol{k})^2 \left\langle \sum_{i=1}^{N}\sum_{j=1}^{N} e^{-i\boldsymbol{k}\cdot(\boldsymbol{r_i}-\boldsymbol{r_j})} \right\rangle \tag{3.8}$$

where the brackets denote a thermodynamic ensemble average taken over the position of all the scatterers in the system. The sum is now taken between pairs of atoms i and j.

Dividing through by all terms related to the magnitude of the the scattered wave, $|A_0|^2$, $f(\boldsymbol{k})^2$ and N, we are left with a geometrical term

$$S(\boldsymbol{k}) = \frac{1}{N}\left\langle \sum_{i=1}^{N}\sum_{j=1}^{N} e^{-i\boldsymbol{k}\cdot(\boldsymbol{r_i}-\boldsymbol{r_j})} \right\rangle. \tag{3.9}$$

This is called the structure factor and it describes how the arrangement of the atoms affects the interference of the scattered x-rays.

Using this definition, for a group of N particles the total differential cross section for scattering is

$$\frac{d\sigma}{d\Omega} = N\frac{d\sigma_1}{d\Omega_1}S(\boldsymbol{k}) \tag{3.10}$$

where the one in the subscript indicates that the cross section on the right hand side is defined per particle.

The structure factor has a particularly simple interpretation in $\boldsymbol{r}$-space, which is accessed by a Fourier transformation.

$$G(\boldsymbol{r}) = \frac{1}{N}\frac{1}{(2\pi)^3}\int_{-\infty}^{\infty} e^{-i\boldsymbol{k}\cdot\boldsymbol{r}}\left\langle \sum_{i=1}^{N}\sum_{j=1}^{N} e^{-i\boldsymbol{k}\cdot(\boldsymbol{r_i}-\boldsymbol{r_j})} \right\rangle \tag{3.11}$$

$$= \frac{1}{N}\left\langle \sum_{i=1}^{N}\sum_{j=1}^{N} \delta(\boldsymbol{r}-(\boldsymbol{r_i}-\boldsymbol{r_j})) \right\rangle \tag{3.12}$$

The density correlation function $G(\boldsymbol{r})$ then expresses the probability to find two particles that are separated by a vector $\boldsymbol{r}$ out of a population of N particles. In k-space, the meaning is similar. The structure factor is then proportional to the probability to find two particles that are separated by a wavenumber $\boldsymbol{k}$. Given a particular value of $\boldsymbol{k}$, the structure factor is equivalent to the probability of finding another particle which may constructively interfere with the scatter wave.

The sum in Eq. (3.9) can be expanded so that the structure factor takes on the form

$$S(\boldsymbol{k}) = 1 + \frac{1}{N}\left\langle \sum_{i=1, i\neq j}^{N} e^{-i\boldsymbol{k}\cdot(\boldsymbol{r_i}-\boldsymbol{r_j})} \right\rangle. \tag{3.13}$$

The factor of one comes from the case when $i = j$ so that $r_i - r_j = 0$ and the argument of the exponential in Eq. (3.9) is zero. This contribution describes the atoms as scattering as a collection of isolated particles with no net interference. For $i \neq j$, the summation term can assume a net value for certain values of $\boldsymbol{k}$ that correspond to regular interparticle spacings or structure in the ensemble.

In a highly ordered system like a crystal, the position of each atom is highly correlated to the rest of the atoms in the crystal through the lattice. When Bragg's law is fulfilled for an incident x-ray with some $\boldsymbol{k}$, the spacing between crystal planes is a multiple of a full wavelength. This gives the condition for constructive interference of the scattered wavefront. Alternatively, in k-space, there is a high probability to find an atom in an adjacent crystal plane separated by the specific value of $\boldsymbol{k}$. The structure factor in Eq. 3.13 takes on a large value because it's easy to find two atoms that scatter constructively. On the other hand an ideal gas lacks interparticle interactions so that the position of the ith particle is independent of its neighbors. The ensemble average is then taken over the r_i and r_j terms separately, both of which average to zero. In the absence of correlations, scattering is equally probable in all

directions.

In position space, the density function for the electrons is simply a sum of delta functions. We may write $\rho(\boldsymbol{r})$ and its Fourier transform as

$$\rho(\boldsymbol{r}) = \sum_{i=1}^{N} \delta(\boldsymbol{r} - \boldsymbol{r_i}),\ \rho(\boldsymbol{k}) = \sum_{i=1}^{N} e^{-i\boldsymbol{k}\cdot\boldsymbol{r_i}}. \tag{3.14}$$

The static structure factor of Eq. (3.9) then takes on the simple form

$$S(\boldsymbol{k}) = \frac{1}{N} < \rho(\boldsymbol{k})\rho(-\boldsymbol{k}) >= \frac{1}{N} \int e^{-i\boldsymbol{k}\cdot\boldsymbol{r}} < \rho(\boldsymbol{r})\rho(0) > d\boldsymbol{r}. \tag{3.15}$$

The terms in brackets are the density-density correlation functions calculated in r and k-space. These functions describe the amount of correlation between the positions or wavevectors of pairs of particles throughout the ensemble. This is evident in the density-density correlation function in r-space: we take each particle at r=0 and compare the fluctuations in its position to the rest of the particles located at $\boldsymbol{r}$ and then sum these correlations over all possible interparticle distances.

Figure 3.2 shows the results of numerical calculations of the structure factor for low density carbon at two temperatures. The structure factors show an oscillatory behavior that is more pronounced for the lower temperature curve. The structure factor reaches a maximum at around 1.3 Å^{-1}, which is from constructive interference from the nearest neighbor atoms.

By the definition of the Wigner-Seitz radius, the average separation between two particles is simply $2r_s$. For carbon at $\rho = 0.34$ g/cc, the first peak in the structure factor occurs at $k = 2\pi/2r_s$ or $k = 1.3$ Å^{-1}. At shorter distances (and larger values of k), the material looks more like a collection of individual atoms so that the structure factor approaches the ideal gas limit. The higher temperature curve exhibits less variation from the ideal gas limit because of the lessened influence of interparticle interactions in comparison to the thermal energy of the particles.

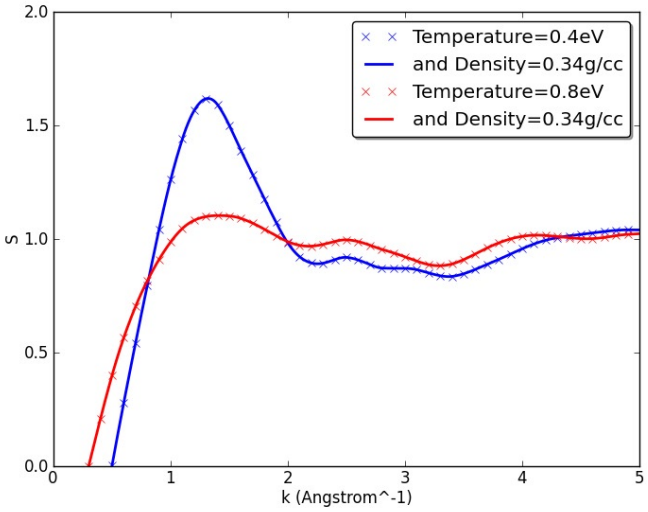

Figure 3.2: Results of DFT-MD calculations of the structure factor for carbon (Gianluca Gregori, University of Oxford). The structure factor was calculated for carbon at ρ =0.34 g/cc at two temperatures

3.3 Inelastic scattering

The static structure factor of Eq. (3.15) considers the correlations of the fluctuations in the spatial positions of the particles, which affects the magnitude of the scattering as function of $\boldsymbol{k}$. By analogy, we can define a dynamic structure factor (DSF) to account for the density fluctuations in time (75). The particles move along time dependent trajectories $\boldsymbol{r_i}(t)$ so that the density is now

$$\rho(\boldsymbol{k}, t) = \sum_{i=1}^{N} e^{-i\boldsymbol{k}\cdot\boldsymbol{r_i}(\boldsymbol{t})}. \tag{3.16}$$

Much like Eq. (3.15), the DSF is then the Fourier transform of the time dependent density-density correlation function

$$S(\boldsymbol{k}, \omega) = \int e^{i\omega t} \frac{1}{2\pi N} < \rho(\boldsymbol{k}, t)\rho(-\boldsymbol{k}, 0) > \tag{3.17}$$

The DSF is invariant to shifts in time, so we may consider correlations between two times t and t' with corresponding frequencies ω and ω'. The density-density correlation function in ($\boldsymbol{k}$, ω) space is related to the dynamic structure factor by

$$< \rho(\boldsymbol{k},\omega)\rho(-\boldsymbol{k},\omega') >= NS(\boldsymbol{k},\omega)\delta(\omega-\omega') \tag{3.18}$$

The simplest case to consider is a non-interacting plasma. If we describe the particle motion by the vector

$$\boldsymbol{r_i}(t) = \boldsymbol{r_i} + \boldsymbol{v_i}t \tag{3.19}$$

we can write the particle density as

$$\rho^0(\boldsymbol{k},\omega) = \sum_{i=1}^{N} e^{-i\boldsymbol{k}\cdot\boldsymbol{r_i}}\delta(\omega - \boldsymbol{k}\cdot\boldsymbol{v_i}). \tag{3.20}$$

Here the superscript 0 indicates the particles are non-interacting. Using Eq. (3.18), the structure factor for the physically interesting case of $\boldsymbol{k} \neq 0$ is then

$$S^0(\boldsymbol{k},\omega) = \int d\boldsymbol{v} f(\boldsymbol{v})\delta(\omega - \boldsymbol{k}\cdot\boldsymbol{v}) \tag{3.21}$$

The velocity distribution of the particles, $f(\boldsymbol{v})$, entered through the ensemble average of the density-density correlation function. This indicates the sensitivity of the structure factor to thermodynamic variables.

This analysis may be extended to an interacting plasma based on the simplifying assumptions that each particle interacts with a screening potential so that longer range correlations do not need to be considered. The electrons are taken as a uniform background that establishes charge neutrality in the plasma. These assumptions form the basis of the one component plasma model

The effect of this screening is to reduce the effective particle density by a factor equal to the dielectric response function, $\epsilon(\boldsymbol{k},\omega)$

$$\frac{\rho^0(\boldsymbol{k},\omega)}{\rho(\boldsymbol{k},\omega)} = \epsilon(\boldsymbol{k},\omega). \tag{3.22}$$

Carrying out the derivation from Eq. (3.18), the DSF is then

$$S(\boldsymbol{k},\omega) = \frac{S^0(\boldsymbol{k},\omega)}{|\epsilon(\boldsymbol{k},\omega)|^2} = \frac{1}{|\epsilon(\boldsymbol{k},\omega)|^2}\int d\boldsymbol{v} f(\boldsymbol{v})\delta(\omega - \boldsymbol{k}\cdot\boldsymbol{v}) \tag{3.23}$$

This is a statement of the fluctuation-dissipation theorem (76), which relates the density fluctuations that give rise to the scattering spectrum to the effect of screening within the plasma (63). For weakly coupled plasmas, the dielectric response function may be calculated explicily using the random phase approximation (RPA) or Debye-Hückel approximation. Modeling strongly coupled plasmas is much more involved, but the details are beyond the scope of this work.

3.4 Modeling the x-ray scattering spectrum

In an experiment to spectrally resolve an x-ray scattering profile, a detector measures the scattered x-ray power divided into frequency intervals of $d\omega$ over a solid angle of $d\Omega$. The scattered power can be written as (77)

$$P_s(\boldsymbol{R},\omega)d\Omega d\omega = \frac{P_0 r_0^2 d\Omega}{2\pi A} N S(\boldsymbol{k},\omega)d\omega|\hat{\boldsymbol{k}_s}\times(\hat{\boldsymbol{k}_s}\times\hat{\boldsymbol{E}_0})|. \tag{3.24}$$

An incident x-ray power of P_0 irradiates an area of the plasma A and is scattered by a collection of N electrons with a scale length on the order of the classical electron radius r_0. The cross product term accounts for the polarization of the incident x-rays. For the unpolarized x-rays used to probe the present experiment, this term is simply $|\hat{\boldsymbol{k}_s}\times(\hat{\boldsymbol{k}_s}\times\hat{\boldsymbol{E}_0})| = \frac{1}{2}(1+\cos^2\theta)$.

We experimentally measure the power spectrum of scattering from a plasma and compare it to a theoretical computation of the DSF. Since the DSF is sensitive to the velocity distribution function, the scattered spectrum can reveal the thermodynamic state of the plasma. By varying parameters such as density, temperature, and ionization, the theoretical DSF may be fitted to the experimental data. The thermodynamic parameters that yield the "best fit" DSF to the data are taken as the inferred values for the plasma conditions.

The DSF can be split into three terms denoting contributions to the scattering spectrum from elastic scattering by bound electrons, inelastic scattering by free electrons, and inelastic scattering by electrons that are lifted into the continuum (78; 79),

$$S(\boldsymbol{k},\omega) = |f_I(\boldsymbol{k}) + q(\boldsymbol{k})|^2 S_{ii}(\boldsymbol{k}) + Z_{free} S^0_{ee}(\boldsymbol{k},\omega) + Z_c \int \widetilde{S}_{ce}(\boldsymbol{k},\omega-\omega') S_s \boldsymbol{k},\omega' d\omega'. \tag{3.25}$$

Figure 3.3 depicts an x-ray scattering spectrum and the relative contribution of these three terms. The elastic scattering component conserves the incident photon energy and is centered at zero energy shift. The profile is broadened chiefly by the finite resolution of the detector. The downshifted Compton peak is comprised of scattering from free and weakly bound electrons. For moderate ionizations, the free electron scattering dominates the Compton peak. The final component is Raman excitations of core electrons, which forms a broad background at energy shifts greater than the core electron binding energy.

3.4.1 Elastic scattering

The elastic scattering comes from electrons which are strongly bound to the ions and those in the screening cloud that dynamically follow the ion motion. These relative contributions are weighted by the atomic form factor $f_I(\boldsymbol{k})$ and a similarly defined screening charge $q(\boldsymbol{k})$. In the limit of small $\boldsymbol{k}$ the screening charge drops out

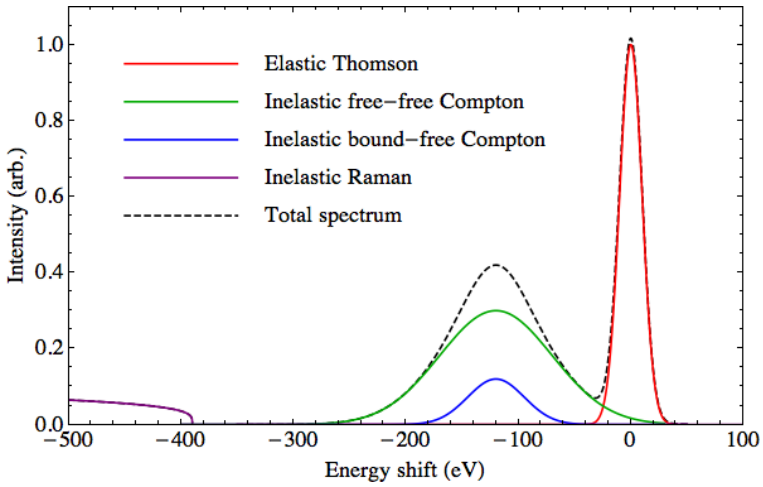

Figure 3.3: A synthetic scattering spectrum showing the contributions from elastic and inelastic scattering.

and we have (6)

$$\lim_{\boldsymbol{k}\to 0} f_I(\boldsymbol{k}) + q(\boldsymbol{k}) = Z_b \tag{3.26}$$

Here Z_b is the number of core electrons that have a binding energy greater than the Compton shift. The scattering from the bound electrons has a small inelastic component from ion thermal and wave motion. However, the frequency shifts are too small to currently resolve in experiments. The elastic scattering is treated as monochromatic, which motivates the use of a static ionic structure factor $S_{ii}(\boldsymbol{k})$.

3.4.2 Inelastic free-free scattering

The second term accounts for inelastic Compton scattering from free electrons. The weighting factor Z_{free} is the sum of the number of kinematically free electrons (created through ionization) and valence electrons that are shared by the ions. The latter contribution is typical of metals that have delocalized electrons within the conduction band. For an ideal gas at small k, we can write the ratio of the intensities of the elastic to inelastic scattering as Z_b^2/Z_{free}. Therefore, the scattered spectrum is

sensitive to the ionization state of the plasma.

By Eq. (3.23), the spectral shape of the DSF is influenced by the velocity distribution of the electrons, which is related to thermodynamic variables of interest. For a non-degenerate plasma ($\Theta >> 1$) the electron velocities will take on a Maxwell-Boltzmann distribution. The Compton peak will then reflect the Gaussian shape of the distribution. The width will be sensitive to the electron temperature through $\sigma_v = \sqrt{3k_BT/me}$. A degenerate plasma ($\Theta << 1$) will assume Fermi-Dirac statistics so that the electron velocities are distributed according to the density of states. The Compton peak will be parabolic with a total width of $\sqrt{2m_e\epsilon_F}$. Since the Fermi energy depends on the density, the width of the inelastic peak will be sensitive to the electron density.

3.4.3 Inelastic bound-free scattering

The final term in Eq. (3.25) accounts for inelastic scattering of bound electrons. The relation of the electron binding, E_b, to the Compton shift determines the scattering process. Strongly bound core electrons with $E_b > E_C$ predominantly participate in elastic scattering. Inelastic x-ray Raman scattering is also possible, in which a core electron gains energy from a vibrational excitation and is promoted into the continuum. The photon loses an energy equal to the core binding energy, leading to a broad spectral feature with a threshold at E_b

Compton scattering is only possible if the electron can accept the recoil momentum. For weakly bound electrons, this is the case if $E_b < E_c$. For the experiments in this work, the average Compton shift was 117 eV. Accordingly, all four of the valence electrons in carbon were accessible to Compton scattering. The ensemble average of the density-density fluctuation term in Eq. (3.17) instead must be performed over the initial bound and final continuum states of the electron.

The first spectrally resolved x-ray scattering experiments were performed by Du

Mond on cold beryllium (80). Consistent with the theory of Compton for inelastic scattering from isolated electrons, Du Mond assumed that the electrons in beryllium scattered as free electrons with momenta distributed according to the bound states. This is equivalent to the assumption that the time scale of the interaction is so short that the potential well of the atom is unchanged by the removal of the electrons and that the electrons' wavefunctions take on plane wave solutions.

These approximations form the core of the impulse approximation (IA). The DSF then takes on a form similar to Eq. (3.21), but with the velocity distribution $f(\boldsymbol{v})$ replaced by the $|\psi_i(\boldsymbol{p})|^2$, the probability density function in momentum space for the i-th bound state(81; 82). The structure factor in the IA is straightforward to evaluate as all that is required is knowledge of the bound-state wave functions, which can be found by solving the Schrödinger equation.

The IA is correct up to the order $|E_b/E_c|^2$, failing when the binding energy is comparable to the Compton shift (81). The binding energies of the four L-shell electrons in carbon are 11, 24, 48, and 64 eV. For this experiment, the resulting in errors in the IA are 1, 4, 17, and 30 %, respectively. The main source of error is a shift of the location of the Compton peak from the location implied by Eq. (3.3) (72). This shift is called the Compton defect and was first noted by Bloch (83) and measured by Ross and Kirkpatrick (84). The experiments of Weiss demonstrated Compton defects on the order of -10 eV for Molybdenum K-shell x-rays scattered from lithium, beryllium, and polyethylene(85). Efforts to rigorously characterize this effect have been hampered by the difficulty of measuring such small absolute energy shifts.

The form factor approximation (FFA) attempts to improve upon the IA by including the effect of the recoil momentum from the Compton scattering in the final plane wave state of the electron (86). This approach has been used to analyze experimental data in much of the literature on XRTS (68; 64; 73). In these experiments,

the scattering from bound electrons is negligible because either the outer shell electrons are stripped by shock heating or, in the case of beryllium, the valence electrons are already delocalized by residing in the conduction band. To date, the lack of experimental scattering data for partially ionized, HEDP systems precludes a direct comparison of these two methods.

3.5 Conclusion

This chapter has presented an overview of the theory of x-ray scattering from dense plasmas. X-ray scattering provides for simultaneous and noninvasive measurements of the temperature, density, and ionization state of dense plasmas. multiple thermodynamic state variables as well as the atomic state of weakly ionized species. The experiments that are later presented in this thesis span a poorly characterized regime from cold, un-ionized carbon to fully stripped to the heliumlike state. This provides a unique opportunity to evaluate theoretical models of the bound-free scattering contribution.

CHAPTER IV

Design and implementation of the Imaging x-ray Thomson spectrometer

4.1 Introduction

In this chapter, I present an overview of the design and implementation of a spatially resolving x-ray spectrometer for x-ray scattering experiments on the Omega laser facility. The result was the creation of the Imaging x-ray Thomson spectrometer instrument through a collaboration with researchers at LANL.

Experiments in the 1930s demonstrated that the performance of x-ray crystal spectrometers could be dramatically improved by curving the crystal. In the Johann and Johannson geometries (87; 88), the crystal is bent to a cylindrical profile. This offers increased resolution by eliminating the dependence of the spectral width on the spatial extent of the source. Alternatively, the von Hámos scheme (89) places the source at the focal position of the cylindrical curvature, which offers increased brightness and the ability to spatially resolve the x-rays. Improvement in crystal fabrication in later years made it possible to create x-ray optics based on spherically-bent crystals. These could either be arranged to provide two-dimensional imaging within a narrow spectral window (90), or combining the imaging of the von Hámos spectrometer with the improved dispersion of the Johann scheme (91).

Because of the relative difficulty in aligning crystal optics for fine resolution, a common approach in high-energy density facilities is to use a flat or singly-curved crystal optic. Mosaic crystals, which consist of randomly aligned grains of crystals, such as highly oriented pyrolytic graphite (HOPG) are commonly used for their high-brightness in the mosaic focussing mode (92; 93). However, the spatial and spectral resolution achievable with a mosaic crystal in a von Hámos spectrometer is limited by aberrations in the crystal and the wide spectral bandpass. (94).

The FSSR-1D scheme, employing a spherical crystal for one-dimensional spatial focusing and spectral dispersion, has been used extensively in HEDP experiments (95; 96; 97; 98; 99; 100). This configuration uses relatively easily manufactured and aligned spherical crystals to achieve high spectral and spatial resolution when certain geometric constraints can be met. These constraints arise from the fact that the Bragg angle is limited to larger than 45 degrees (101) and must to be greater than 80 degrees to limit astigmatism (102).

Perhaps for this reason, spherical crystals have been used much less extensively in spectroscopic applications at high energy density. As discussed further below, the focus here is on the need for a compact diagnostic that can be inserted and aligned from a single direction and within a relatively small solid angle. This is important in the context of facilities such as OMEGA or the NIF in which diagnostic access and perhaps time for alignment are very limited.

Advances in optics technologies have allowed the mating of high quality crystals with toroidally curved substrates (103). With unequal radii of curvature, toroidal crystals can be made free from astigmatism so that any Bragg angle may be chosen. This greatly increases the flexibility for the instrument to fit in tight geometries. These crystals have been used to create two-dimensional, monochromatic images with high resolution (104; 103; 105).

This chapter demonstrates how such a crystal can be used to create an imaging

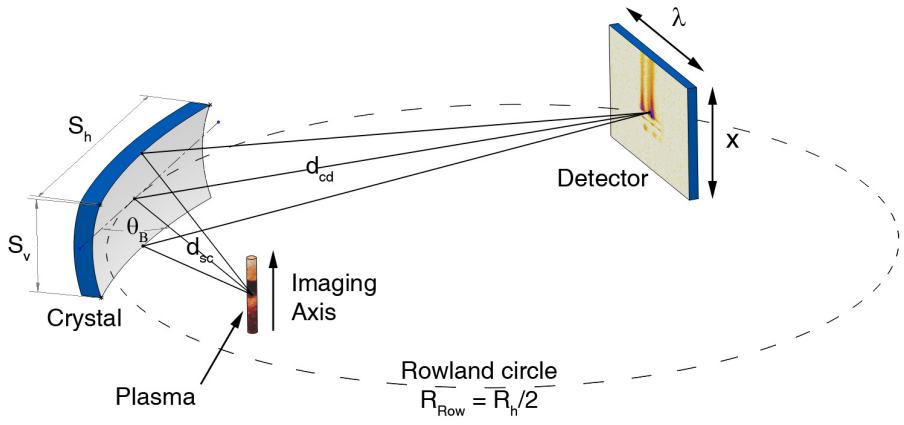

Figure 4.1: A schematic of the toroidal imaging crystal arrangement. The ratio of the source to detector distances yields a magnified image with $M = d_{sc}/d_{cd}$

spectrometer(106) that yields magnified 1D images with high spatial and spectral resolutions. A sketch of this arrangement is given in Figure 4.1. The Bragg angle may be made small, with the spatial resolution limited only by higher-order aberrations like coma, so that the instrument can be inserted and aligned from a single direction.

4.2 Optimizing the crystal parameters

To better understand and optimize the choice of a crystal for a toroidal imaging spectrometer, this section is devoted to a geometrical analysis of the x-ray throughput of this arrangement. This analysis is similar to a derivation presented by Missalla et al. (107). The throughput of the crystal is defined in terms of the effective solid angle of the detector with respect to the source for a single value of the photon energy. The assumption is that the crystal is small so that the central energy approximately describes the complete energy range.

4.2.1 Geometrical definitions

A perfect Bragg crystal, cut from a defect free, semiconductor grade wafer, forms the basis of the diagnostic. X-ray photons of wavelength λ are dispersed according

to the well known Bragg law,

$$\sin\theta_B = m\lambda/2d \tag{4.1}$$

where θ_B is the Bragg angle, m is the diffraction order, and d is the spacing of the crystal lattice planes. The crystal is bent along a toroidal surface so that it has two different radii of curvature. The focal lengths of the horizontal and vertical curvatures are related to the two bending radii R_h and R_v, respectively, and the Bragg angle.

$$f_h = \tfrac{1}{2}R_h \sin\theta_B, \quad f_v = \frac{R_v}{2\sin\theta_B} \tag{4.2}$$

For a single photon energy, the condition for stigmatic two-dimensional imaging may be met if R_h and R_v are chosen such that f_h=f_v. One-dimensional imaging within a spectral window is possible if the lensmaker's equation is satisfied for the vertical curvature only.

$$\frac{1}{d_{sc}} + \frac{1}{d_{cd}} = \frac{1}{f_v} \tag{4.3}$$

The crystal-to-detector distance, d_{cd}, is set so that the detector lies on the Rowland circle defined by the horizontal curvature

$$d_{cd} = R_h \sin\theta_B \tag{4.4}$$

Solving (4.3) for the source-to-crystal distance, d_{sc}, in terms of the magnification $M = d_{cd}/d_{sc}$ yields

$$d_{sc} = \frac{R_v}{2\sin\theta_B}\frac{M+1}{M} \tag{4.5}$$

The crystal face is selected as a section of the convex/convex face of a three-dimensional toroid. The chosen coordinate system has the origin at the center of the

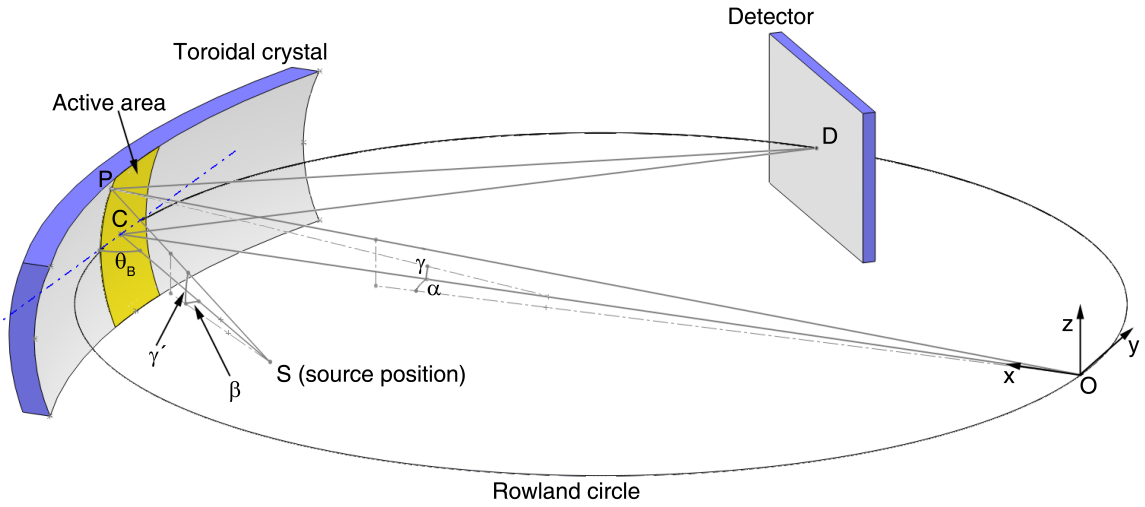

Figure 4.2: A sketch showing the definition of the geometry used in the analysis of toroidally curved imaging spectrometers. The horizontal curvature is defined along the xy-plane while the vertical curvature is along the xz-plane.

toroid as shown in Figure 4.2. The center of the crystal is defined as point C. An arbitrary point P on the surface of the toroid is then described by the vector $\overrightarrow{OP}$. This vector is a function of a horizontal angular displacement α and a vertical angle γ as measured from the axis along vector $\overrightarrow{OC}$

Photons are emitted by a point source, at position S. The central source-to-crystal vector $\overrightarrow{SC}$ makes an angle θ_B with the center of the crystal face and has a magnitude d_{sc}. Likewise, the central crystal-to-detector vector $\overrightarrow{CD}$ has a magnitude of d_{cd}. It is assumed that a photon that hits the crystal at a point P will specularly reflect with respect to the local crystal normal $\hat{n}_{crys}$.

We can write these terms as

$$\overrightarrow{OS} = (R_h - d_{sc}\sin\theta_B, -d_{sc}\cos\theta_B, 0) \tag{4.6}$$

$$\overrightarrow{OP} = (\eta\cos\alpha, \eta\sin\alpha, R_v\sin\gamma) \tag{4.7}$$

$$\overrightarrow{OC} = (R_h, 0, 0) \tag{4.8}$$

$$\hat{n}_{crys} = (-\cos\gamma\cos\alpha, -\cos\gamma\sin\alpha, -\sin\gamma) \tag{4.9}$$

$$\eta = R_h + R_v(\cos\gamma - 1) \tag{4.10}$$

We are interested in calculating the variation of the Bragg angle in terms of coordinates with respect to the source, the horizontal and vertical angles (β, γ'). Bragg diffraction will occur as long as the angular deviation from the Bragg angle is within the non-zero region of the rocking curve function, which describes the angular acceptance of the crystal(108). By calculating the deviation of the Bragg angle as a function of the displacement angles (β, γ'), we may express the active area in terms of a solid angle with respect to the source. Thus, this calculation will define the throughput of the crystal.

4.2.2 Geometrical analysis of the imaging spectrometer

For a ray that is displaced by a small angle (β, γ') from the central vector $\overrightarrow{SC}$ to the point P, the angle that the ray makes with the local crystal normal is modified by a small increment δ from the Bragg angle. The local angle of incidence θ' is a function of the angular displacements and the central Bragg angle of incidence $\theta'_B = \pi/2 - \theta_B$.

$$\theta' = \theta'_B + \delta(\beta, \gamma') \tag{4.11}$$

We are interested in the angle of incidence of the source-to-intersection vector, $\overrightarrow{SP} = \overrightarrow{OS} - \overrightarrow{OP}$, relative to the local crystal normal.

$$\theta' = \arccos\left(\frac{\overrightarrow{SP}}{|\overrightarrow{SP}|} \cdot \hat{n}_{crys}\right) \tag{4.12}$$

We may compute this angle using (4.6)-(4.10). Applying the small angle approximation for α and γ and taking terms up to first order yields

$$\theta' = \pi/2 - \theta_B + \left(\frac{R_h \sin\theta_B - d_{sc}}{d_{sc}}\right)\alpha \tag{4.13}$$

Then we can transform the angular deviations back to source-coordinates via the relation

$$\alpha = \beta + \theta'_B - \theta' \tag{4.14}$$

Using (4.4), (4.5), (4.11), and (4.14), (4.13) can be simplified as

$$\delta(\beta) = \left(\frac{M-1}{M}\right)\beta \tag{4.15}$$

Up to first order, deviations in the Bragg angle are affected by only variations in the horizontal angle β. The physical meaning is that, for a given energy, the active area on the crystal forms a thin vertical strip.

Bending the crystal modifies the interaction with x-rays in two ways. The crystal lattice is modified on a microscopic scale, so that the angle that an incident ray makes with the distorted crystal planes changes as it moves through the surface layer of the crystal. This leads to an enhancement of the integrated reflectivity for bent crystals (109). The second effect is apparent from (4.15). The magnification of the imaging spectrometer changes the geometrical variation of the incident angle with the crystal

face.

In the absence of geometrical effects from the curved surface, the integrated reflectivity of the crystal is R_{int}. For simplicity, the rocking curve is taken as a Gaussian function $RC(\delta(\beta))$. Substituting in Eq. (4.15) yields the relationship

$$RC(\delta(\beta)) = RC\left(\left(\frac{M-1}{M}\right)\beta\right) \tag{4.16}$$

The integrated reflectivity is the integral of the rocking curve over all angles of incidence. Evaluating the integral, we recover the curved crystal integrated reflectivity modified by a geometrical term.

$$R'_{int} = R_{int}\left|\frac{M}{M-1}\right| \tag{4.17}$$

4.2.3 Crystal throughput

The active area on the crystal is defined by a thin width Δy_m in the horizontal (dispersion) direction and a length Δx_m in the vertical (imaging) direction. The width of the active area is approximately the length over which the incident angle varies by the geometrically modified integrated reflectivity

$$\Delta y_m \approx \frac{d_{sc} R'_{int}}{\sin\theta_B} \tag{4.18}$$

The crystal focuses all radiation over its vertical dimension S_v so that the length of the active area is $\Delta x_m = S_v$. The solid angle subtended by the active area with respect to the source is then

$$\Omega_{act} = \frac{\Delta x_m \Delta y_m \sin\theta_B}{d_{sc}^2} = \frac{S_v}{d_{sc}} R'_{int} \tag{4.19}$$

Substituting in Eq. (4.5) and (4.17) into Eq. (4.19) yields

$$\Omega_{act} = 2 \sin\theta_B \, R_{int} \left(\frac{S_v}{R_v} \right) \left| \frac{M^2}{M^2 - 1} \right| \tag{4.20}$$

For the spectrometer described in the next section, this equation gives a throughput of 1.82×10^{-5} sr.

While this value is an order of magnitude below the throughput for the more commonly used HOPG spectrometers (6), in certain types of experiments imaging spectrometers using perfect crystals can produce brighter images compared to their non-imaging HOPG counterparts. Using XRTS to diagnose hydrodynamic flows with a non-imaging crystal normally requires time gating the detector (typically using a microchannel plate that offers detection efficiencies of a few percent) and designing a narrow spatial window into the scattering volume. An imaging spectrometer may use an order of magnitude more sensitive image plate or deep-depletion CCD detector while capturing scattering along a large spatial chord in the scattering volume.

4.2.4 Ray tracing analysis

A ray tracing analysis was performed using the SHADOW (110) code for a spectrometer configuration using a Ge(400) crystal with $R_v = 15$ cm, a nominal $R_h = 30$ cm, $S_v = 2$ cm, and $R_{int} = 0.107$ mrad. The calculations were initialized with a monochromatic point source at 4750 eV and θ_B =67.33°. R_h was varied from f_v to 1000 cm with d_{sc} adjusted by means of Eq. (4.5) to fulfill the focusing condition. The throughput was calculated by the resulting brightness of the traced image. The results are plotted against the magnification in Figure 4.3. Also shown is the analytical expression from (4.20).

The analytical expression agrees with the ray tracing results except in the limit of $M \to 1$. To describe the throughput at this position, it is necessary to take higher

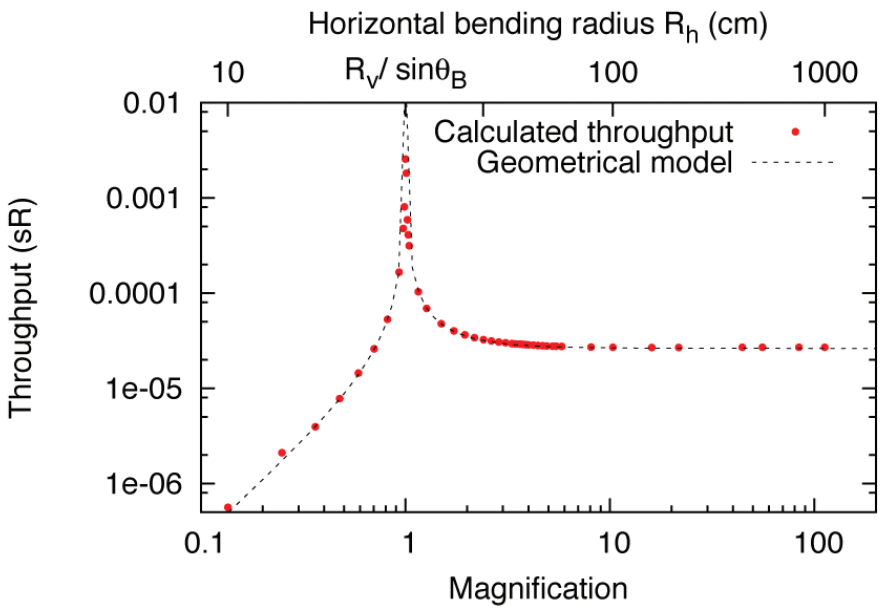

Figure 4.3: Plotted is the analytical expression for the throughput from (4.20) compared to the results from a ray tracing analysis.

order terms in the expansion of Eq. (4.13). A second order term $1/(2\tan\theta_B)\alpha^2$ describes the variation in the angle as the $(M-1)\alpha$ term goes to 0. This limits to a finite value the asymptotic behavior at $M = 1$.

4.3 Tests of the spatial and spectral resolution

To determine the spatial and spectral resolving characteristics of the described imaging spectrometer, we fielded a prototype diagnostic at the Trident laser facility. The spectrometer featured a Ge(400) crystal with $R_v = 20$ cm, $R_h = 40$ cm, M=2.5, and $\theta_B = 70.25°$to observe the helium-like emission from a Ti source. The crystal length in the dispersion direction was 5 cm, yielding a spectral range of 350 eV.

We performed shots on a series of grid targets to evaluate the resolution of the spectrometer. The resolution grid targets consisted of a 12.5 μm thick Ti backlighter foil attached at a right angle to a wire grid as shown in Figure 4.4. The wire grid had alternating 16 and 32 μm copper wires with 130 μm center-to-center spacings. The

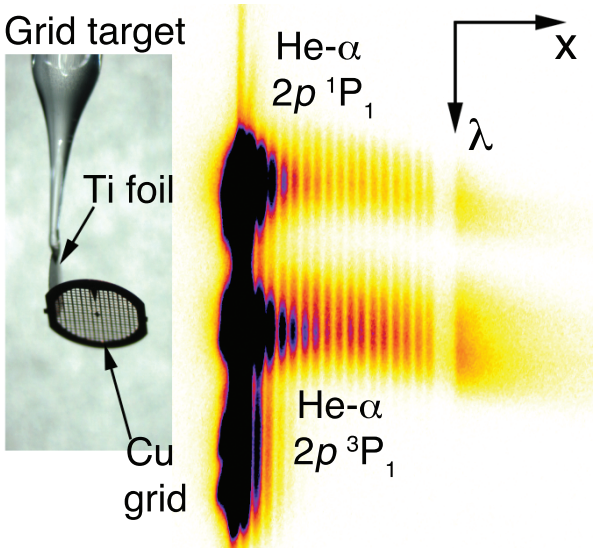

Figure 4.4: A resolution grid target and the resulting spatio-spectrograph from the imaging spectrometer. The image is resolved spatially along the horizontal axis and spectrally along the vertical. The Ti foil produces the saturated vertical line on the left while the spatial modulation in brightness from the grid is visible in the two helium-like emission lines. The full spectral range, spanning 350 eV centered at 4680 eV, is not shown.

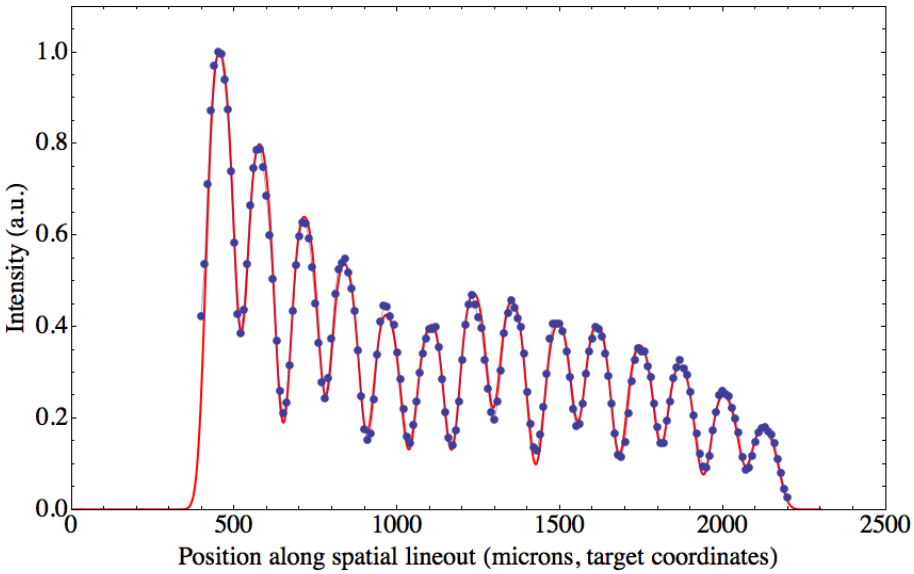

Figure 4.5: Plotted is a spatial lineout through the $2p^3P_1$ line in Figure 4.4 (purple dots) and the fit to the data (red line). The FWHM resolution of the image is 48 μm

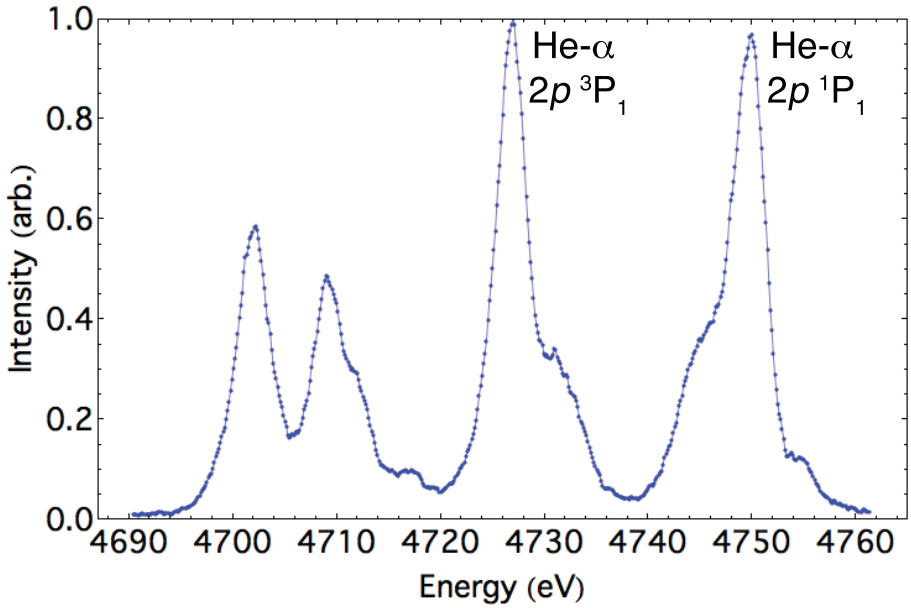

Figure 4.6: Plotted is a spectral lineout left of the foil in Figure 4.4. The FWHM spectral resolution is 4 eV.

spectrometer was focused on the grid so that it viewed it face-on. We irradiated the foils with up to 200 J of 527 nm laser light in 1.2 ns pulses. X-rays created within the extended plasma plume were spatially modulated through the grid and were imaged by the crystal onto a BAS-SR image plate.

Figure 4.4 shows the results from one such resolution test. All 18 grid wires as well as the right edge of the rim of the grid are visible in the image, corresponding to a field of view of at least 3 mm. The spectral direction of the image shows the two prominent He-α lines in the Ti emission as well as weaker transitions at lower energies.

The spatial resolution was estimated by fitting the experimental data to a simulated image. The image plates were scanned at 25 μm per pixel and the spatial magnification of the spectrometer was 2.5. From the Nyquist theorem, we would expect the lower-limit on the spatial resolution to be 20 μm. Figure 4.5 shows a spectrally integrated, spatial lineout of the unsaturated region in Figure 4.4.

Given the known thickness and spacing of the grid wires, an idealized, one dimen-

sional representation of the x-ray transmission was created. This profile was then convolved with a Gaussian point spread function (PSF) to represent the effect of the finite resolution of the crystal imager. By varying the width of the PSF, the theoretical profile was fit to the experimental lineout. Through minimizing the residuals, the best fit indicated a PSF full width at half maximum (FWHM) of 48 μm.

The demonstrated spatial resolution of the spectrometer is likely to be dominated by broadening from within the image plate detector. The image plates we used in the experiments were Fuji BAS-SR scanned with a FLA-7000. The edge response function of the image plate was evaluated by placing a knife edge in front of the detector. The derivative of the edge response function is simply the PSF, which yielded a width of 105 μm on the detector plane. This value is consistent with those reported by Seely et al. (111). Assuming that the broadening from the image plate and the intrinsic resolution of the crystal add in quadrature, we can estimate the resolution limit of the crystal imager itself. With the images resolved to 48 μm and image plate broadening of 105 μm/($M = 2.5$)= 42 μm in the target plane, the intrinsic crystal resolution was then < 25 μm. The results of these tests motivated the use of a x-ray CCD with a higher pixel density.

The limits on the spatial resolution are a consequence of two effects. The first is the fact that the toroidal crystal spectrometers lack the rotational symmetry of spherical crystals and such must be precisely aligned over six axes (112). Subtle errors in the positioning of the source and the setting of the Bragg angle can degrade the spatial resolution by defocusing errors. The second effect comes from the broadening of the source perpendicular to the source-to-crystal vector and imaging axis. The image becomes defocused as the spatial resolution elements move off of the imaging axis.

We performed tests to determine the depth of field of the spectrometer. The source was stepped over a distance of ± 250 μm along the source-to-crystal vector. There was little systematic change in the spatial resolution, only fluctuations of ± 5

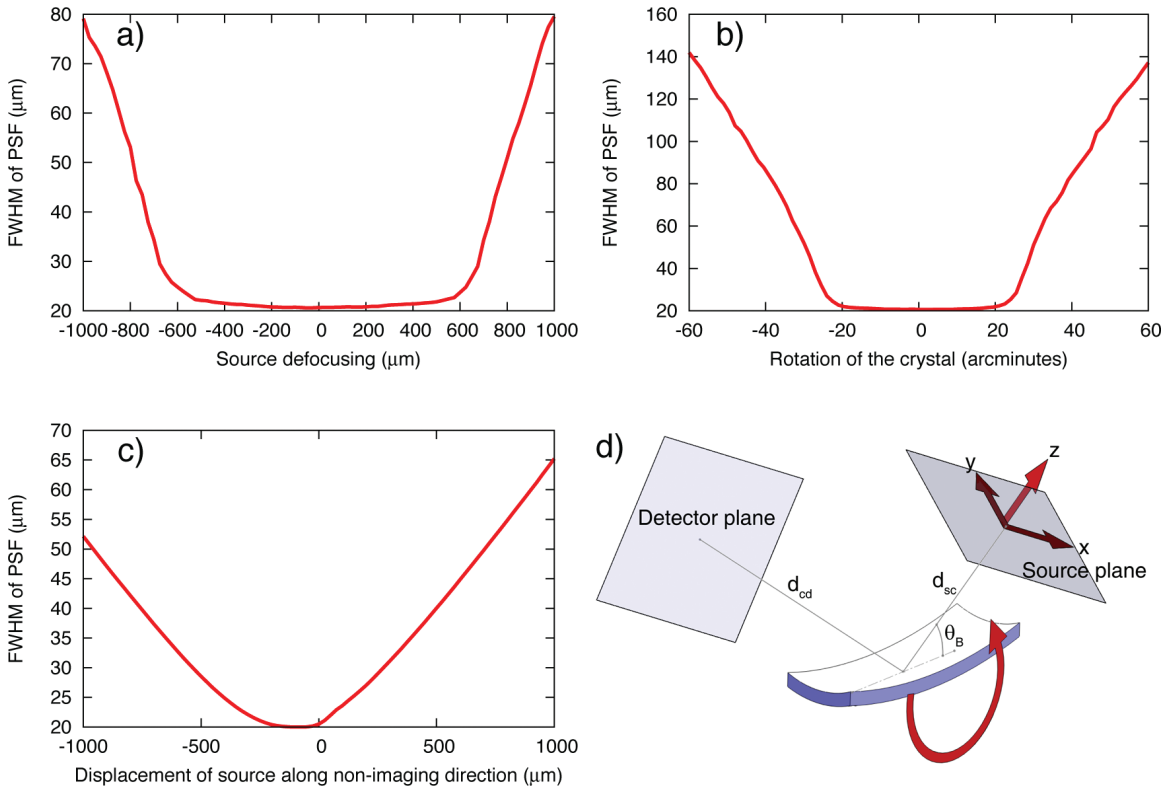

Figure 4.7: Results of the ray tracing analysis to assess defocusing errors. The coordinate system used in the ray tracing is shown in part d). The ordinate in these plots is the FWHM of the PSF divided by the magnification, to yield the PSF width in source coordinates. This value is summed in quadrature with the Nyquist-limited resolution of 20 μm. In plot a), a point source initially at the position of best focus was displaced along the z-axis to evaluate the effect of defocusing through the source-to-crystal vector. For part b), the crystal was rotated about the imaging x-axis to change the angle of incidence off of the Bragg angle. Plot c) shows the results of displacing the point source along the non-imaging y-axis to quantify source broadening.

μm. This indicates that this spectrometer configuration has a depth of field of at least 0.5 mm.

To asses the effect of position errors on the spatial resolution, a raytracing analysis was performed on the spectrometer configuration fielded on Trident. The results are summarized in Figure 4.7. The three largest defocusing effects were source defocusing, rotation of the crystal about the Bragg angle, and lengthening of the spatial resolution elements in the non-imaging direction. Other positioning errors, including detector defocusing and displacements of the source along the imaging axis, were found to have little impact on the spatial resolution. The demonstrated spatial resolution is likely a combination of these three effects, which informed the design of the Omega instrument and subsequent experiments.

The depth of field along the source-to-crystal vector was found to be $\pm$ 600 μm. As our experimental tests showed little variation in the spatial resolution over 500 μm, it is likely that this distance was correctly set in our experiments. The spatial resolution rapidly worsens for angular displacements greater than 20 arcminutes, which may be the ultimate culprit. Displacing the source along the non-imaging y-axis has a similar effect on the spatial resolution as the rotational errors. The plume was allowed to freely expand as it shined through the resolution grid. The dimensions of the source in the non-imaging axis are unknown, but the uniform spatial resolution across the grid suggests that the plume was smaller than the 3 mm grid.

It is essential for future applications of the imaging spectrometer to XRTS experiments to limit the extent of the scattering volume along the non-imaging dimension. Extending the length of the spatial resolution elements will integrate over more signal and yield a brighter signal. However, the added signal from the edges will contribute less and less to central peak of the PSF and instead form a broad foot which contributes little to creating contrast in the image

The raytracing analysis indicates that the spectral resolution is unaffected by an

extended source or positioning errors. Fitting a Gaussian to the two main peaks in the spectrum shown in Figure 4.6 yields a 4 eV FWHM resolution. This resolution is sufficient to see multiple lines around the main helium-like transitions. For the He-α line at 4750 eV, the XOP simulation code (113) indicates the integrated reflectivity for unpolarized light to be 0.130 mrad. Using (4.17), the spectral resolution due to geometric effects can be estimated as

$$\Delta E = \frac{hc}{2d}\left(\frac{1}{\sin(\theta_B)} - \frac{1}{\sin(\theta_b - R'_{int})}\right). \tag{4.21}$$

This expression gives a value for the spectral resolution of $\Delta E = 4.3$ eV at 4750 eV. This value is a bit higher than the experimentally demonstrated resolution, likely because of errors in the calculated value for the integrated reflectivity.

In principle, it is possible to design an instrument of this nature for any desired x-ray source. For a given transition energy, the limited number of crystal planes that yield high integrated reflectivities constrains the choice of the Bragg angle. Higher x-ray energies generally result in lower Bragg angles and reduced spatial resolution from increased coma.

X-ray imaging spectroscopy using toroidally-curved crystals offers a new diagnostic possibility to measure scattered radiation from along a spatial chord. The diagnostic combines high spectral and spatial resolutions with a large field-of-view in space and wavelength. These first attempts demonstrate an instrument which uses a Ge crystal set to the He-α lines of titanium with spectral resolution of $\frac{E}{\Delta E} = 1200$, a spectral range of 350 eV, <25 μm spatial resolution, and a spatial range of at least 3 mm.

A unique strength of the toroidal crystal is the lack of astigmatism which allows for the use of low Bragg angles. In this way, the toroidal crystal imaging spectrometer may easily be adapted to experiments on large high-energy density facilities where space in the target chamber is at a premium.

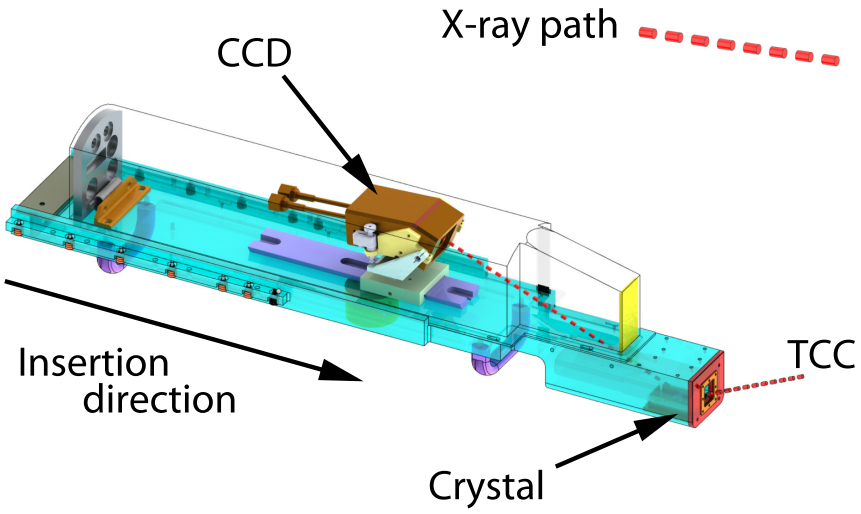

Figure 4.8: A rendering of the computer model of the IXTS. The crystal focus is nominally situated at target chamber center (TCC)

4.4 The Imaging x-ray Thomson spectrometer

The Imaging x-ray Thomson spectrometer (IXTS) was designed and built through a collaboration between the University of Michigan and Los Alamos National Laboratory. The purpose of the diagnostic is to extend the ability of XRTS to be used to diagnose spatially inhomogenous plasmas. Experiments may be done to measure the spatial profile of plasma parameters in a single shot. The IXTS was primarily built for the OMEGA laser at the Laboratory for Laser Energetics in the University of Rochester (114). As diagnostic access is primarily through TIMs, the size constraints of the TIM drove the choice of the toroidal crystal geometry over spherical crystal designs (102) which are limited by astigmatism in angles far from normal.

HOPG crystals are a common choice for XRTS instrumentation as they offer superior brightness in the mosaic-focusing mode (115). The spectral resolution is decreased due to the widening of the crystal rocking curve by the angular spread of the crystallites and depth-broadening from x-ray reflection taking place over an extended depth in the crystal. The latter effect is more pronounced for higher energy

x-rays (92). The wide rocking curve also affects the spatial resolution. In the similar Von Hamos focusing scheme, the spatial resolution can be estimated as $\sim 2R\delta\theta$, where R is the focusing curvature radius and $\delta\theta$ is the rocking curve width(116). For a HOPG crystal with $R \sim 10$ cm and $\delta\theta = 1°$, the predicted resolution of a few millimeters is unacceptably poor for the IXTS.

A schematic of the new diagnostic is shown in Figure 4.8. The spectrometer uses a doubly curved, "perfect" germanium crystal that images in one spatial dimension while spectrally resolving in the other. The IXTS must be aligned very accurately to achieve the best spatial resolution. The source position is found by scanning the focus using an optical source. A physical pointer then recalls that source position for alignment. The TIM holding the IXTS is positioned relative to the target chamber center using that pointer. We found that the TIM may be retracted and reinserted multiple times without repointing with no discernible loss of focusing.

The IXTS crystal is Ge(220) bent to a toroidal profile with vertical and horizontal radii of curvature of 10 and 100 cm, respectively. The crystal bending is done with great care to ensure that fracturing of the lattice is minimized, yielding high spectral and spatial resolution. The germanium attenuates x-rays within the top 10 microns of the surface, so that depth broadening is minimal. The source-to-crystal distance is 19.1 cm and the crystal-to-detector distance is 39.6 cm yielding a magnification of 2.07. The Bragg angle is far from normal, at 23.4°, which corresponds to the heliumlike transition of nickel at 7.8 keV. The diagnostic can accommodate other energy ranges by changing the crystal, but the Bragg angle must be close to 20° to fit within the spectrometer body.

There are several tradeoffs in the choice of x-ray probe. Higher energy x-rays will attenuate less through photoabsorbtion in the sampled material. This is especially important for imaging XRTS target geometries where a there is a need to illuminate a large region to expose spatial structure. However, these high energy x-rays are more

difficult to generate and detect. Intense sources of K-shell x-rays may be created by using lasers to heat thin metallic foils. The efficiency of the laser to x-ray conversion process has been found to decrease strongly with the K-shell x-ray energy (117). This is manifested as a decreasing contrast between the heliumlike lines and the x-ray continuum for higher-Z targets (118). The presence of spectral features in the region spectrally downshifted from the main heliumlike emission can also interfere with the extraction of data from the Compton peak.

The x-rays are detected by a back illuminated, deep-depletion CCD (Princeton Instruments PI-MTE). The CCD chip contains 2048×2048 pixels of 13.5 μm pitch. With deep depletion CCDs, the depth of the photosensitive epitaxial silicon layer is extended thereby increasing the probability that an x-ray will be photoabsorbed and detected. This results in a factor of 2-3 higher quantum efficiency than a typical CCD for x-rays created from mid-Z sources (119). The choice of a digital detector was also motivated by facility concerns. Since the entire diagnostic sits in vacuum, retrieving image plate or film requires retracting the TIM which can cost time on an experimental day. A drawback is that the CCD has much poorer dynamic range than film or image plate. The CCD saturation level of 100,000 photoelectrons/pixel is equivalent to about 46 7.8 keV x-ray photons/pixel, which is a factor of 50 below that of an image plate (120) .

Together with the horizontal bending of the crystal, placing the detector on the Rowland circle improves the linearity of the dispersion and negates source broadening. These are key advantages for measurements of Thomson scattering. The scattered signal tends to be very weak compared to the laser-irradiated mid-Z plasma that typically serves as an x-ray source. Experiments have shown that low-density plasma may blow around shielding, leading to source broadening that distorts the scattered spectrum. The information on the electron temperature and density in non collective Thomson scattering lies in the width of the inelastic scattering feature. Improved

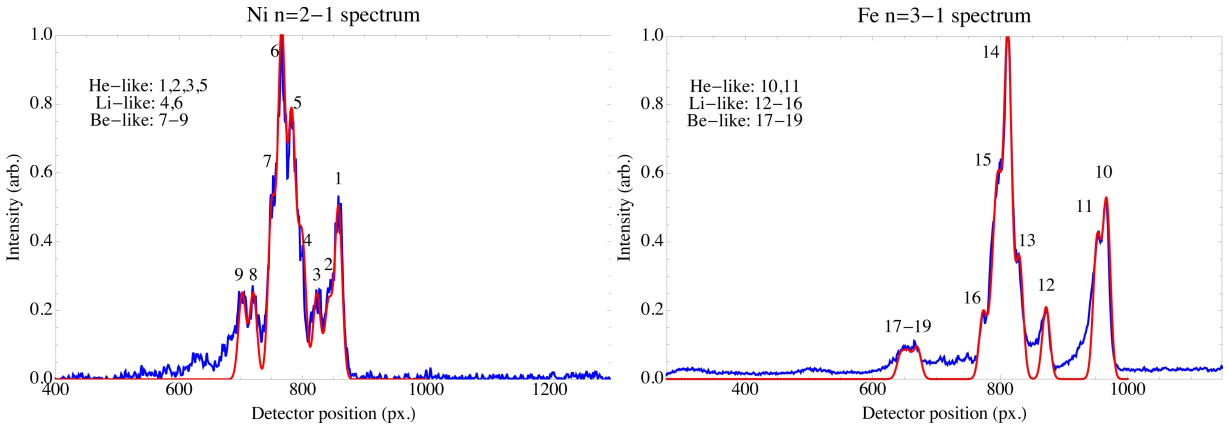

(a) (b)

Figure 4.9: Spectra collected from irradiating thin foils of nickel (a) and iron (b) on the Trident laser. The lines are clustered around the nickel He-α and iron He-β. The abscissa is the position on the detector and the ordinate is the scaled intensity. The blue curve is the recorded spectrum. The red curve is the result of a peak search using the x-ray transition energies from (121; 122; 123; 124; 125)

linearity in the dispersion eases the analysis by reducing the amount of resampling needed to linearize the scattered spectrum.

4.5 First tests of the IXTS at the 200-TW Trident laser facility

We first tested the IXTS using the long-pulse beams of the Trident laser facility. Thin foils of nickel and iron were irradiated with up to 200 J of 527 nm laser light in 1 ns. Two representative spectra are shown in Figure 4.9. The identified x-ray transitions are numbered and fit to Gaussians with FWHM of 9 eV. The peaks are numbered according to the transitions listed in Table 4.11. These spectra are sampled from the brightest region near the foil where the line widths are affected by Doppler broadening. In cooler regions of the ejected plasma plume, the line widths are reduced to around 4 eV.

The spectral dispersion of the detector is calculated using the known positions and

energies of the identified x-ray transitions. Figure 4.10 shows a plot of the dispersion. The red curve, a geometrical calculation of the dispersion, is in very good agreement with the positions of x-ray transitions from the detector. For ease in later analysis, the dispersion curve is fit to a second order function. The dispersion function is then

$$E(x) = 7342 + 0.4801(849 + x) + 7.858 \times 10^{-5}(849 + x)^2. \tag{4.22}$$

This function converts between a pixel location on the detector and an x-ray energy in electron volts.

In both spectra, lithium-like lines dominate the emission over the He-α. Given the stronger oscillator strengths of the heliumlike transitions, the foils may have been significantly underdriven so that the heliumlike charge state was not significantly populated. The laser beam was set to best focus (80-100 μm) on the foils with a nominal intensity of a few 10^{15} W/cm^2 (126). We tested a prototype of the scattering target described in the next chapter on Trident. We observed no evidence of a scattered signal due to high background levels and poor production of the nickel source x-rays.

We initially operated the CCD with an open aperture because the interior of the diagnostic was built to be light-tight. The background levels were relatively high, on the order of one 7.8 keV photon/pixel. This background was likely from fluorescence of the aluminum body of the spectrometer (127). We added a 50 μm thick Kapton window to the front of the CCD, which dropped the background to a level almost indistinguishable from exposures taken without the laser beams propagating.

4.5.1 Filter fluorescence

The spectrometer has a filter pack on the aperture. The filtering consists of a 50 μ thick beryllium light block and additional high-Z x-ray attenuators. To establish the signal level for the disk shots, we used iron filters of varying thickness. We started

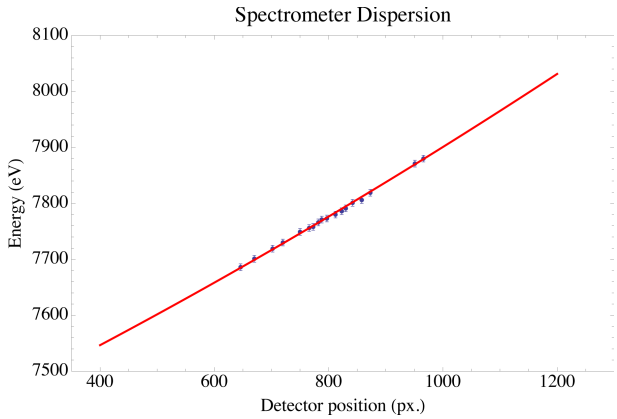

Figure 4.10: Plotted is the experimental dispersion curve of the IXTS. The red curve is a geometrical calculation of the dispersion and the blue points are the positions of the identified transitions in the iron and nickel spectra.

Index	Transition	Wavelength (Å)	Energy (eV)
Nickel			
1	$1s2p\ ^1P_1^o - 1s^2\ ^1S_0$ (He-α_1)	1.5885	7806
2	$1s2p(^1P)3p\ ^2S_{1/2} - 1s^23p\ ^2P_{3/2}$	1.5893	7802
3	$1s2p\ ^3P_2^o - 1s^2\ ^1S_0$ (He-like)	1.5923	7786
4	$1s2p\ ^3P_2^o - 1s^2\ ^1S_0$ (He-α_2)	1.5965	7766
5	$1s^22p\ ^2P_{1/2} - 1s2p^2\ ^2D_{3/2}$	1.5978	7753
6	$1s^22p\ ^2S_{1/2} - 1s2s2p\ ^2P_{1/2}$	1.6000	7750
7	$1s2p^2\ ^4P_{3/2} - 1s^22p\ ^2P_{1/2}$	1.6039	7730
8	$1s2p^2\ ^4P_{1/2} - 1s^22p\ ^2P_{1/2}$	1.6062	7719
Iron			
10	$1s3p\ ^1P_1^o - 1s^2\ ^1S_0$ (He-β_1)	1.5732	7881
11	$1s3p\ ^3P_1^o - 1s^2\ ^1S_0$ (He-β_2)	1.5751	7871
12	$1s2s\ (^1S)3p\ ^2P_{3/2} - 1s^22s\ ^2S_{1/2}$ (Li-like)	1.5856	7819
13	$1s2s(^3S)3p(^2P_{1/2}) - 1s^22s(^2S_{1/2})$	1.5931	7790
14	$1s2p(^3P)3p(^2D_{3/2}) - 1s^22p(^2P_{1/2})$	1.5936	7780
15	$1s2p(^3P)3p(^4P_{5/2}) - 1s^22p(^2P_{3/2})$	1.5951	7773
17	$1s2s3d_{5/2}]_{3/2} - 1s^22p_{1/2}$ (124)	1.5980	7758
18-20	Be-like satellites		7686 - 7700

Figure 4.11: A listing of the identified x-ray lines in Figure 4.9

with a thickness of 50 μm of iron which had a transmission of a few 10^{-6} to the Ni He-α at 7.8 keV. There was no discernible line radiation and the image consisted of uniform noise. Reducing the iron filter thickness dropped the noise level and line radiation appeared on the CCD.

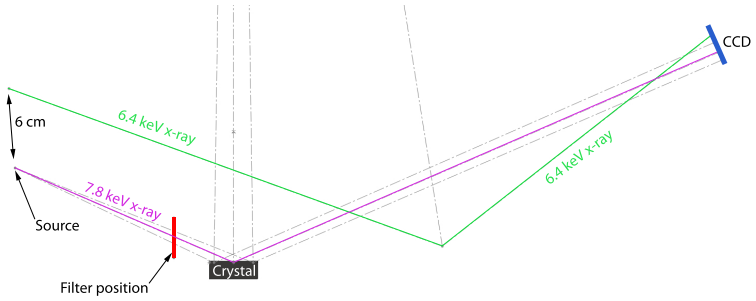

Figure 4.12: The violet ray is the properly focused, Ni He-α. For the Fe K-α to undergo Bragg diffraction and for the reflected ray to hit the CCD, the incident ray must reflect at a point distant from the actual crystal and source.

One hypothesis conjectured that the noise on the CCD was coming from the fluorescence of the iron filter, driven by absorption of the Ni He-α. Since the iron was relatively transmissive to its K-α and absorptive to the Ni He-α, reducing the thickness of the iron filter boosted the Ni line while reducing the intensity of the iron fluorescence. It was also hypothesized that, since the filter was so large and close to the crystal, the Fe K-α would be Bragg diffracted onto the CCD.

Upon analysis of the crystal geometry, it is not possible that the Fe K-α could have been Bragg diffracted onto the CCD. While the filters may have fluoresced, the iron targets would have only driven K-shell fluorescence from the weaker He-β transition. Low energy fluorescence of the crystal and spectrometer body seem a more likely source of noise.

Figure 4.12 shows a diagram of the possible reflection of the Fe K-α. To satisfy the Bragg law for the Fe K-α, the crystal would have needed to be much larger. The difficulty in overlapping energies on the detector is a natural consequence of the negation of source broadening from the horizontal curvature of the crystal.

Since the targets were iron instead of nickel, K-shell vacancies in the filter could have been only created by He-β transitions or higher. The K-shell binding energy of iron is 7.1 keV (128) while the He-α is at 6.7 keV, Ly-α at 6.9 keV, and He-β at

7.8 keV. The Fe He-β yield is perhaps an order of magnitude lower than the He-α (117). In any case, since these photons could not Bragg diffract from the crystal, fluoresced photons would be nearly indistinguishable from the brighter He-α as both energies would be absorbed by the crystal and spectrometer interior to drive low energy fluorescence.

Spectrometer fluorescence

The x-rays that make it through the beryllium are at least 1 keV and illuminate a small region on the inside of the spectrometer. Figure 4.13 is an illustration of the region of the inner surfaces of the spectrometer that are directly illuminated by the source. The largest exposed area is aluminum, followed by the germanium of the crystal, and finally the stainless steel of the crystal substrate and the aperture frame. Of these materials, the following fluorescence transitions are possible with Fe/Ni He-α irradiation: Ge/Fe/Cr/Ni L-shell at 500-1400 eV, Al K-shell at 1.5 keV, Cr K-shell 5.4 keV and Fe K-shell. The 50 μm of Kapton in front of the CCD will block fluorescence from everything except the chromium and iron K-shell.

This process can be modeled quite simply in one dimension. An incident x-ray of energy E_i hits the crystal and is attenuated according to Beer's law with attenuation coefficient λ_i. If the absorption occurs at a depth of x away from the surface of the crystal, the fluoresced x-ray of energy E_f must then escape back through the same path with attenuation coefficient λ_f. The relative strength of the fluoresced signal is multiplied by the K or L shell fluorescent yield, $\omega_{K,L}$ and a factor of $\frac{1}{2}$ to account for the the fraction of x-rays that propagate towards the surface. We then integrate over the crystal thickness Δx to yield the expression

$$I(E_i, E_f) = \int_0^{\Delta x} \tfrac{1}{2}\omega_{K,L}\lambda_f e^{-\lambda_i x} e^{-\lambda_f x} dx \tag{4.23}$$

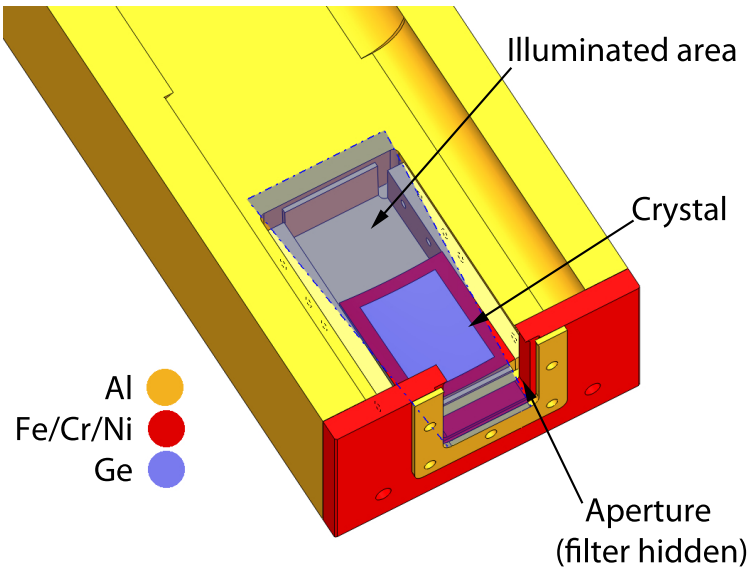

Figure 4.13: A cutaway of the model for the spectrometer. The blue shaded region is illuminated by rays originating at the target chamber center that travel through the spectrometer aperture. The spectrometer is colored according to the material where yellow represents the 6061 aluminum of the spectrometer body, red is 304 stainless steel, and lavender is the germanium crystal.

The units here are fluoresced photons/incident photon or the probability that an incident photon will create a fluoresced photon that escapes to the surface. For our crystal, $\Delta_x = 100$ μm, $\omega_L = 0.015$ for Ge with λ_i and λ_f from NIST. We can also consider fluorescence from the spectrometer interior with $\omega_K = 0.0357$ for Al and $\omega_K = 0.281$ for Cr (129).

The fluorescent yield is plotted in Figure 4.14. For x-rays with incident energy above 6 keV, the Cr K-shell emission dominates. For Ni He-α irradiation, the Fe K-shell will be an order of magnitude brighter in this region. The fact that the Kapton stopped the majority of noise (even with a proper nickel foil source) suggests that the energy in continuum x-rays between 1-6 keV is much greater than that of the line radiation.

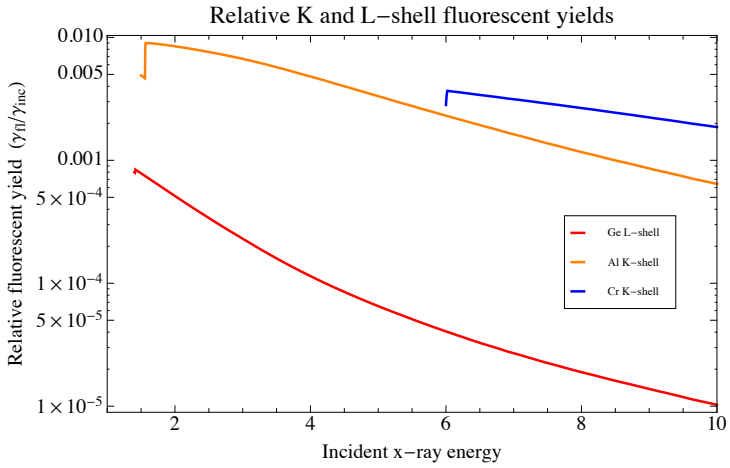

Figure 4.14: A plot of the x-ray fluorescent yield calculated using Equation 4.23

4.6 Conclusion

This chapter has presented the design and implementation of a new x-ray scattering diagnostic for the Omega laser facility. The IXTS extends the ability of XRTS to be used to diagnose spatially inhomogenous plasmas. This diagnostic is currently available for experiments at the Omega and Omega EP laser facilities.

Of interest to future experiments is the development of x-ray Thomson scattering diagnostics with even higher spatial resolutions, on the order of 10 μm or better. There is generally a tradeoff between spatial resolution and signal brightness. The IXTS is time integrating so that the length of the laser pulse use to drive the x-ray source determines the amount of motion blurring in the shock. This may be reduced with the use of ultrafast K-α sources with pulse durations on the order of picoseconds. However, the conversion efficiencies for these sources are on the order of $10^{-4} - 10^{-5}$ (130; 65). Spherical aberration may be reduced by limiting the width of the crystal in the focusing direction, at the expense of signal. Likewise, the spatially integrating dimension of the scattering slit on the target may be made narrower to limit astigmatism. This tradeoff between spatial resolution and Poisson noise may favor higher resolution in experiments to probe very dense matter, for example capsule

implosion experiments with electron densities $> 10^{24}$ (131).

CHAPTER V

Spatially-resolved x-ray scattering measurements of a planar blast wave

Figure

5.1 Introduction

In this section, an experiment is described to diagnose the material conditions created in a blast wave driven in a near-solid density carbon foam. We performed these experiments on the Omega laser facility in two shot days in March and September of 2012. A diagram of the experiment is given in Figure 5.1. The goal of the experiment was to take a snapshot of the scattering from the blast wave when it had traversed approximately halfway through the foam. We can infer from this scattering data the spatial profiles of the temperature, ionization, and density across the blast wave propagation direction.

These experiments are the first to use x-ray scattering to diagnose an HEDP system that has large 1D gradients in the material conditions. The temperature in the shock inferred by x-ray scattering is shown to be consistent with an independent determination of the temperature by means of simultaneously measuring the shock compression and speed. The experimental results indicate a stronger than expected

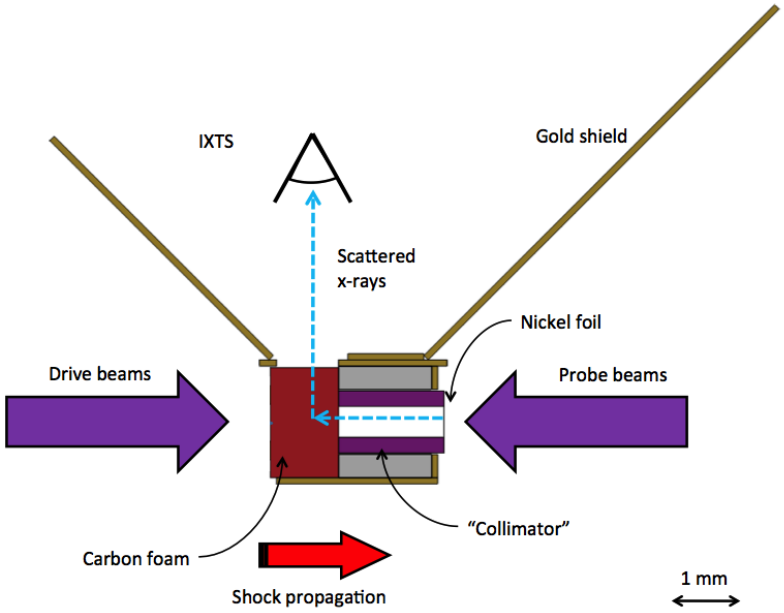

Figure 5.1: A schematic of the design for the Omega x-ray scattering experiment

preheat of the foam by heat transport from the laser-irradiated spot. This leads to a reduced compressions in the shock. In comparison to hydrodynamic modeling of the temperature profile of the blast wave, the experimental data shows higher temperatures in the rarefaction which is indicative of either a weaker than expected rate of cooling or the presence of an additional source of heating. The inferred temperatures and ionization states show good agreement with the results from a collisional-radiative simulation code for material near the shock front. In contrast, the material in the rarefaction is more strongly ionized than is suggested by the equilibrium calculations from the simulation code, leading to further evidence of nonlocal heating.

A set of ten Omega "drive" beams were incident on a block of carbonized resorcinol formaldehyde (CRF) foam. The ablation of material from the laser irradiated surface of the foam drove a strong shock which transitioned to a blast wave some time after the end of the laser pulse. The drive beams delivered 4.5 kJ $\pm 1\%$ of 0.351 μm laser light in a 1 ns FWHM, nominally flat-topped pulse with a rise and fall time of 100 ps. The beams were smoothed with phase plates and SSD to a spot size of 860 μm

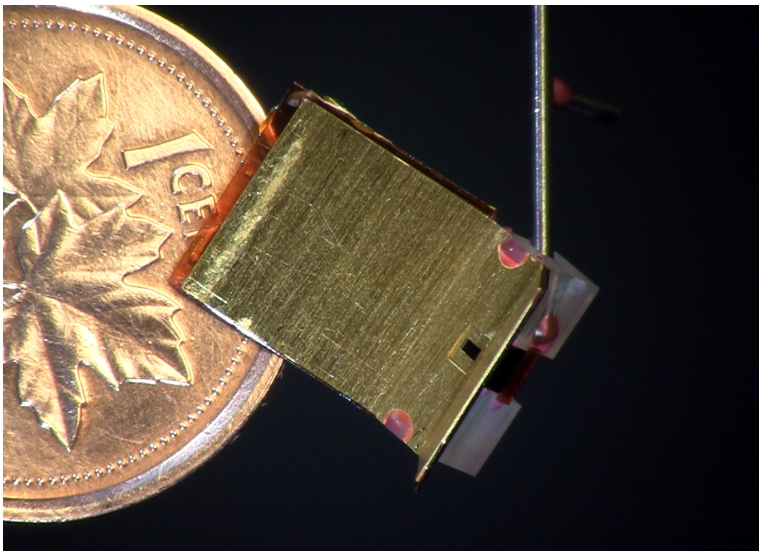

Figure 5.2: A completed x-ray scattering target next to a penny for scale.

FWHM resulting in a irradiance of 7×10^{14} W/cm^2 $\pm$ 10%.

After a delay of several nanoseconds, a second set of 12 "probe" beams heated a thin (5 μm) nickel foil to create a source of x-rays for scattering. The line emission from this source came primarily from the 7.8 keV He-α doublet from the 2-1 transition in He-like nickel ions. The probe beams delivered up to 5.4 kJ of laser light over a 1 ns pulse at an intensity of $3{\times}10^{15}$ W/cm^2. As the effectiveness of the conversion of laser light to x-rays depends on the intensity of the laser spot, I set the intensity to maximize the production of x-rays informed by the scalings in Workman and Kyrala(117).

A probe delay of 8.2 ns was chosen based on the results from HYADES simulations, given in Figure 5.3. The simulations indicate that the shock front will have moved 650 μm from the drive surface. Since the scattering aperture is displaced by 100 μm relative to the drive surface, the shock should be about half way through the aperture at this time. The simulations indicate a temperature of about 20 eV, density of 1.36 g/cc, and an ionization state of 2.5. These conditions describe a weakly coupled, partially degenerate plasma with $\Gamma_{ee} = 0.6$ and $\Theta = 1.9$

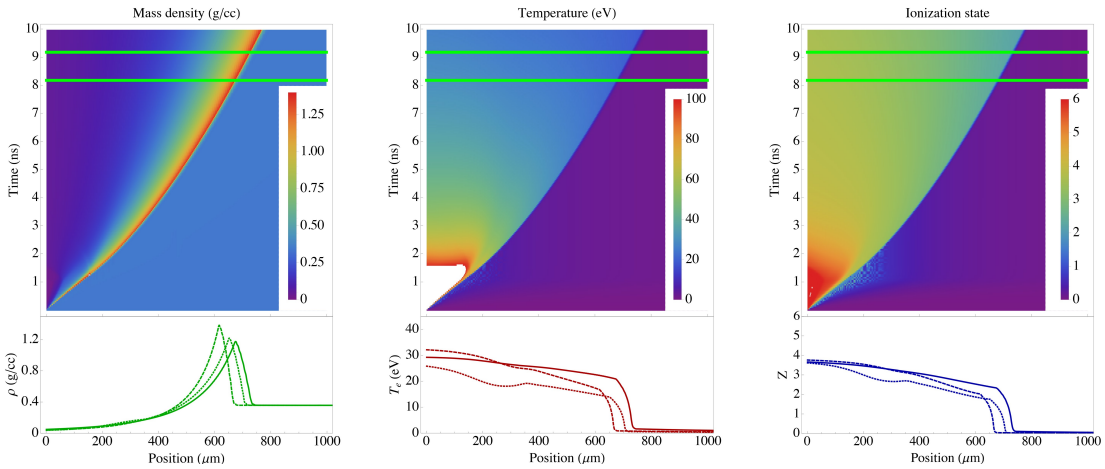

Figure 5.3: Results from HYADES simulations for the density (a), temperature (b), and ionization state (c) of the foam using an ideal gas EOS with $\gamma = 5/3$. The 1D simulations are time integrated over the 1 ns duration of the backlighter, the region between the green lines in the upper plots. The lower plots show the motion blurred quantities as the solid lines. For comparison, results are given of the same calculation using the polystyrene (dotted lines) and carbon (dashed lines) EOSs.

5.2 Target design

A central difficulty in laser x-ray scattering experiments is the low level of the signal as relative to the sources of background. This is further compounded in this experiment by the time-integrating nature of the IXTS. A successful target design requires large shields to block lines-of-sight to any surface that has been heated by even a small amount of laser energy. Another potential issue is that the spatial resolution of the IXTS suffers for extended sources. Therefore, the x-ray illumination must be restricted to the central region of the foam.

The target consisted of four main parts: an acrylic scaffold, a machined block of CRF, large gold shields, and an x-ray source and collimator. The design goals were to create a low-variability, easy to build target with large overlapping shields to ensure the collection of an uncontaminated scattering signal. Figure 5.2 presents a photograph of a completed target.

A machined piece of acrylic acted as the main structure of the target. Various slots were machined into the acrylic to act as sockets for the target components. Using this approach, we were able to reduce the variability in the relative positioning of the target components as they were constrained by the higher precisions that are achievable through machining. In addition, the targets were easier to build because we did not have to measure the absolute positions of any target components.

The material under investigation in this experiment was CRF foam at densities of 200 and 340 mg/cc. By weight, this material is 93 % carbon, 6% oxygen, and 1 % hydrogen (71). The Chemical Sciences Division at LLNL provided us with samples of this material, which were machined into blocks of dimensions $1.1 \times 1.8 \times 1.8$ mm for the targets.

CRF belongs to a class of low-density material called aerogels. The synthesis of organic aerogels was first reported by (132). A common resorcinol formaldehyde resin is prepared as a gel. Then, the liquid component is removed through a process called supercritical drying. The final step is pyrolysis in a argon or nitrogen atmosphere to drive off volatiles and convert the aerogel to nearly pure carbon. What is left behind is a "skeleton" of empty foam cells with an average cell size of 10 nm.

The low density nature of aerogels makes them useful in experiments to probe non-degenerate, heated matter. This is in comparison to the potential drawbacks to using solid density carbon in this experiment. The higher density would have resulted in much higher attenuation of the probe x-rays, limiting the scale length of the experiment. For a given drive laser energy, a larger density will result in a lower shock temperature. Coupled with the increased Fermi energy of the solid material, we would have required significantly more energy to drive solid carbon to the same physical regime as an aerogel.

The large gold shields are the two wings of the target, which are located in front of the two laser irradiated surfaces. They act to block the IXTS from being blinded

by stray light. A scattering aperture was laser-cut into the shields to allow for the scattered x-rays to escape and be picked up by the IXTS. The aperture was 1 mm long in the imaging direction and 0.5 mm in the spatially integrating direction. The known length of the scattering aperture also acted as a spatial fiducial in the scattered images.

One effect of the laser irradiation is to fill up the vacuum near the target with a hot, low-density blowoff plasma. The shields have to block both the strong emission directly coming from the laser spot and the weaker, but non-localized emission from the blowoff plasma. This drove the wings to be quite large, almost a cm in length. The target also had a smaller gold shield located behind the foam. This served much the same purpose to prevent blowoff plasma from shining directly through the scattering aperture.

A gold tube, 1.7 mm long with a 0.5 mm central circular aperture, acted to collimate the x-rays to limit the spread of incident $\boldsymbol{k}$-vectors to $\pm\ 8^{\circ}$ and restrict the scattering to the central portion of the foam. The choice of the aperture width on the collimator is a tradeoff between the spatial resolution and the signal level. On the image plane, the IXTS images in one dimension and integrates along the other. A source with a large lateral extent will be poorly focused, and lose spatial resolution. Based on the results from the ray tracing analysis presented in the previous chapter, the aperture diameter was chosen to get at least 50 μm of spatial resolution. Secondly, the shock is most planar close to the central axis. The DPPs used to smooth the laser spots have a supergaussian profile with a nominal full-width at half maximum of 412 μm. The drop in the laser intensity at the edges of the spot leads to a curved shock profile. This could potentially blur the 1D spatial profile, leading to averaging of the inferred thermodynamic parameters. The collimator restricts the probe x-rays to a region well within the uniform drive laser spot where the shock is most planar.

To assess the degree of curvature in the shock front at the desired probing time,

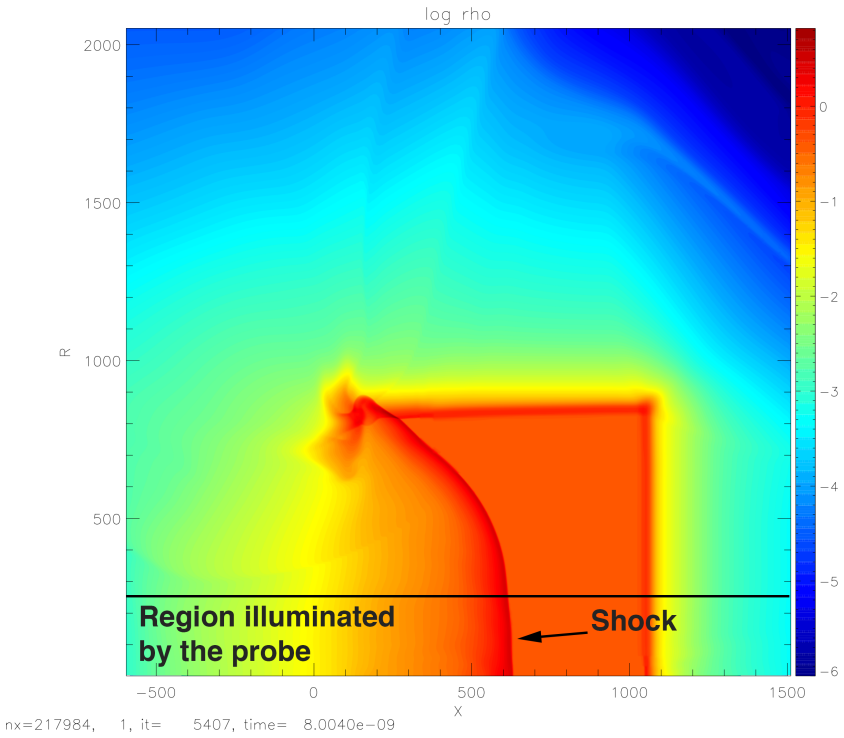

Figure 5.4: 2D CRASH simulations suggest that the shock front is planar to within 15 μm at 8 ns in the central region illuminated by the probe x-rays.

2D CRASH (133) simulations were performed by Matt Trantham at the University of Michigan. A density plot of the simulation results is shown in Figure 5.4. The simulations indicate that the shock front is curved very slightly, with the edges of the illuminated region trailing the center by 15 μm. These small displacements are below the resolution of the crystal imager and therefore curvature of the shock front is ignored in the analysis of the data.

5.2.1 2D analysis of the source collimation

A geometrical calculation was performed to evaluate the expansion of the x-rays in the foam. The problem is simplified by the cylindrical symmetry of the collimator. At an arbitrary point (r_1, z_1) in the foam, the source subtends a solid angle per unit

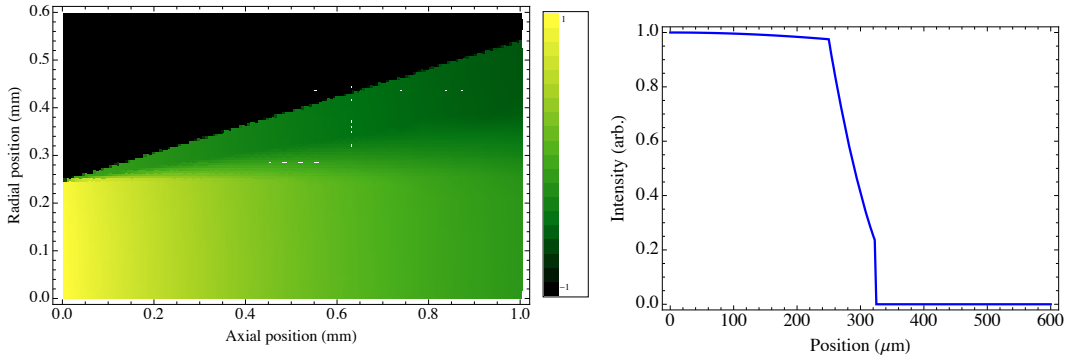

(a) (b)

Figure 5.5: (a) A density plot of the x-ray illumination of the foam. In this image, the x-rays are incident from the left. At all points the x-rays remain inside the foam, so that scattering from the shields is not possible. (b) Plots a radial line out of the x-ray intensity profile at a point mid-way through the foam. The x-rays are confined to a region well inside the initial drive laser spot.

length of

$$\frac{\Omega(r_1, z_1)}{r d\theta} = \int_{r_l}^{r_u} \frac{dr}{(z_1 + z_c)^2 + (r_1 - r)^2}. \tag{5.1}$$

Here x_c is the length of the collimator and r_l and r_u are the upper and lower radial extents of the source that are visible from that arbitrary point (r_1, z_1). In Figure 5.5 (a) shows this integration carried out over a mesh of points corresponding to a radial slice in the foam. Taking a lineout across the midpoint of this image (b) shows the radial profile of the x-ray intensity at the expected shock position. Rotating this profile about the central axis and integrating indicates that 93% of the x-ray photons remain within the initial radius of the collimator. The fullest extent of the x-rays lies well within the initial spot size of the laser irradiated drive surface of the foam.

5.2.2 Photometric analysis

Following Glenzer and Redmer (6), the number of detected photons in the inelastic scattering can be written as

$$N_{ph,d} = \left(\frac{E_L}{h\nu}\eta_x\right)\left(\frac{\Omega_{pl}}{4\pi}\eta_{att}\right)\left(\frac{n_e\sigma_{Th}\ell}{1+\alpha^2}\right)(\Omega_{det}DQE) \tag{5.2}$$

Here E_L is the probe laser energy, η_x is the fraction of laser energy that is converted to K-shell x-rays, Ω_{pl} is the solid angle of the scattering volume with respect to the x-ray probe, η_{att} is the fraction of x-rays transmitted through the plasma, n_e is the free electron density, σ_{Th} the differential Thomson scattering cross section, ℓ is the scattering path length, α is the dimensionless scattering parameter taken so that $1+\alpha^2 \sim 1$ for non-collective scattering, Ω_{det} is the collection solid angle of the detector, and DQE is the quantum efficiency of the detector.

Using the known parameters of the experiment, Eq. 5.2 is used to estimate the strength of the scattered signal. Values of $E_L = 5.4$ kJ, $h\nu = 7.8$ keV, $\eta_x = 0.005$ (117), $\Omega_{pl} = 0.04$ sr, $\eta_{att} = 0.64$, $n_e = 7 \times 10^{22}$ e/cc, $\ell = 0.1$ cm, $\Omega_{det} = 10^{-5}$ sr, and DQE=50% were used in the estimation. These parameters yield a total of 10^5 x-ray photons in the inelastic scattering over the 1 mm extent of the foam. Each 50 μm spatial slice of the target yields a spectra containing 5000 photons. This is equivalent to 150 photons per 50 μm spatial-5 eV spectral resolution element with a signal-to-noise ratio of 12.

5.3 Experimental data

A sample piece of scattering data is given in Figure 5.6. sion is vertical, with energy increasing to the top, while the spatial dimension is horizontal. A shock is driven in the scattering volume from the image left while x-rays are incident from image right. The bright splotch on the right edge of the image is from an extended

nickel plasma plume peeking around the stray light shielding in the target.

In this image, lineouts along the vertical direction yield scattering spectra. In the following analysis, the plasma conditions along spatial profiles are extracted by fitting theoretical spectra to these data. The first step is to spatially and spectrally calibrate the images and correct for various non-linearities.

5.3.1 Calibrating the images

The first step in the analyzing the data was to spatially and spectrally calibrate the scattered images. A dimension in pixels on the detector can be calibrated to a dimension in the target plane as

$$d_{\mu m} = d_{pix} * \frac{13.5 \mu m}{M} \tag{5.3}$$

based on the CCD pixel size of 13.5 μm, fill factor of 100 %, and the IXTS magnification of 2. A useful check to this calibration is that the width of the scattering aperture was resolved to the correct dimension of 1 mm. The images were binned into slices of approximately 40 μm spatial resolution elements by integrating over 6 pixels in the spatial direction. Each of these slices then contained a scattered spectrum.

It is likely that the absolute energy calibration, measured from the edge of the CCD, changes over time as the IXTS is disassembled for storage in between shot days. Therefore, the peak of the elastic scattering at 7806 eV was used as a reference point. The x-coordinate of each spectrum was zeroed at the center of this elastic scattering peak. The experimental calibration function from Eq. 4.22 was then used to convert the x-axis energy. The spectra were then binned and smoothed into 5 eV resolution elements. In this way, the image was divided from the 1 mm scattering aperture into twenty spatially-resolved spectra.

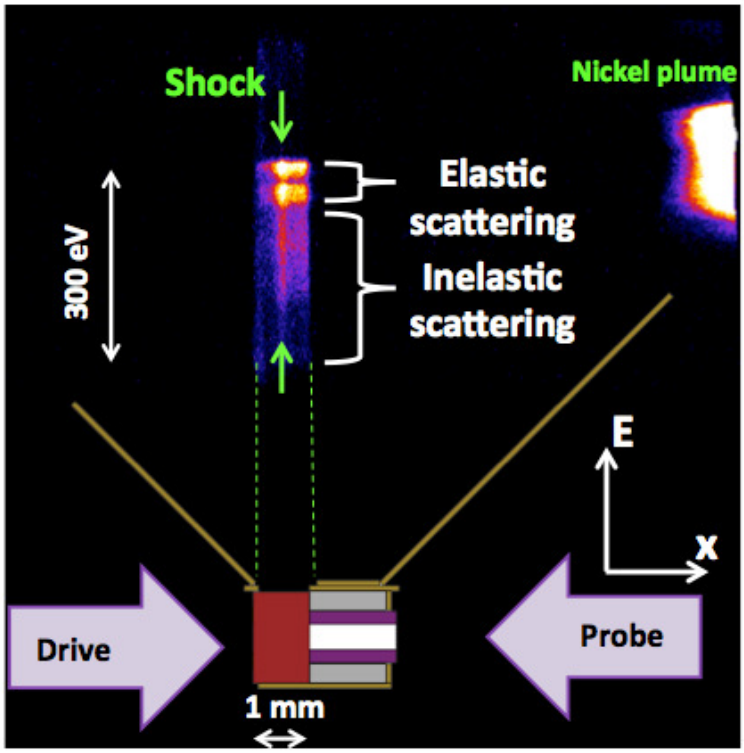

Figure 5.6: A sample piece of data from the XRTS experiment at a source delay of 8.2 ns.

5.3.2 Flat field corrections

The next postprocessing step was to correct for nonuniformities in the gain of the IXTS. Since the IXTS uses direct detection of x-rays by a CCD, the nonlinearities in the detection process are minor compared to time gated detectors that use microchannel plates (134). However, errors in the crystal manufacturing process can still introduce anomalies to the spectra.

We evaluated the spectral response of the IXTS by shooting a thin plastic foil during the experimental campaign on the Trident laser facility. Since the K-edges of the constituents of the plastic are all below 1 keV, the spectrum at 8 keV is a broadband, featureless x-ray continuum. The laser irradiation creates a thermal population of x-rays with a temperature of a few keV. In the absence of spectral peaks, the high energy tail of the thermal electron population still creates x-rays

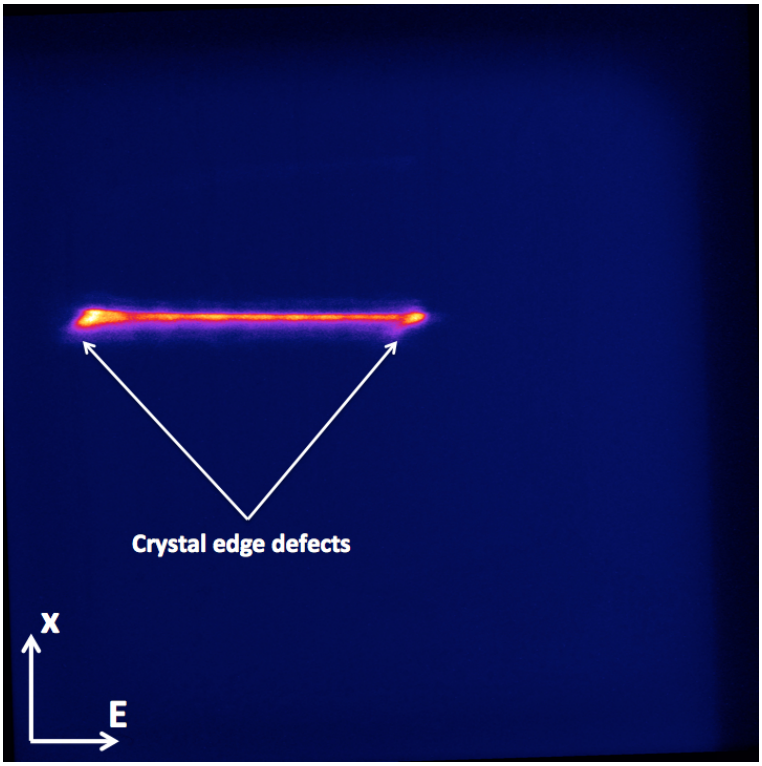

Figure 5.7: A full frame of the IXTS flat field image taken with a driven plastic foil. The increased brightness at the edges of the spectrum are from edge defects in the crystal.

through bremsstrahlung radiation. Any deviation from a flat spectral response on the detector will later be used to normalize the scattered x-ray spectra, a process that is called flat-fielding.

Figure 5.7 shows the results of the flat fielding shot. The x-ray continuum is evident as the bright band in the middle of the image. The lower energy side slightly diverges from the idealized line focus, which is a symptom of a slight crystal misalignment that was later corrected. There is also some shadowing on the upper and right sides of the image from clipping the edges of the camera.

I display a line out across the emission in Figure 5.8 (a). The edges of the spectrum are noticeably brighter than the central regions. We noticed this effect as well in the optical tests of the crystal. It is likely a manufacturing flaw. The crystal is held onto the substrate through an optical contact. The adhesive forces are strongest in

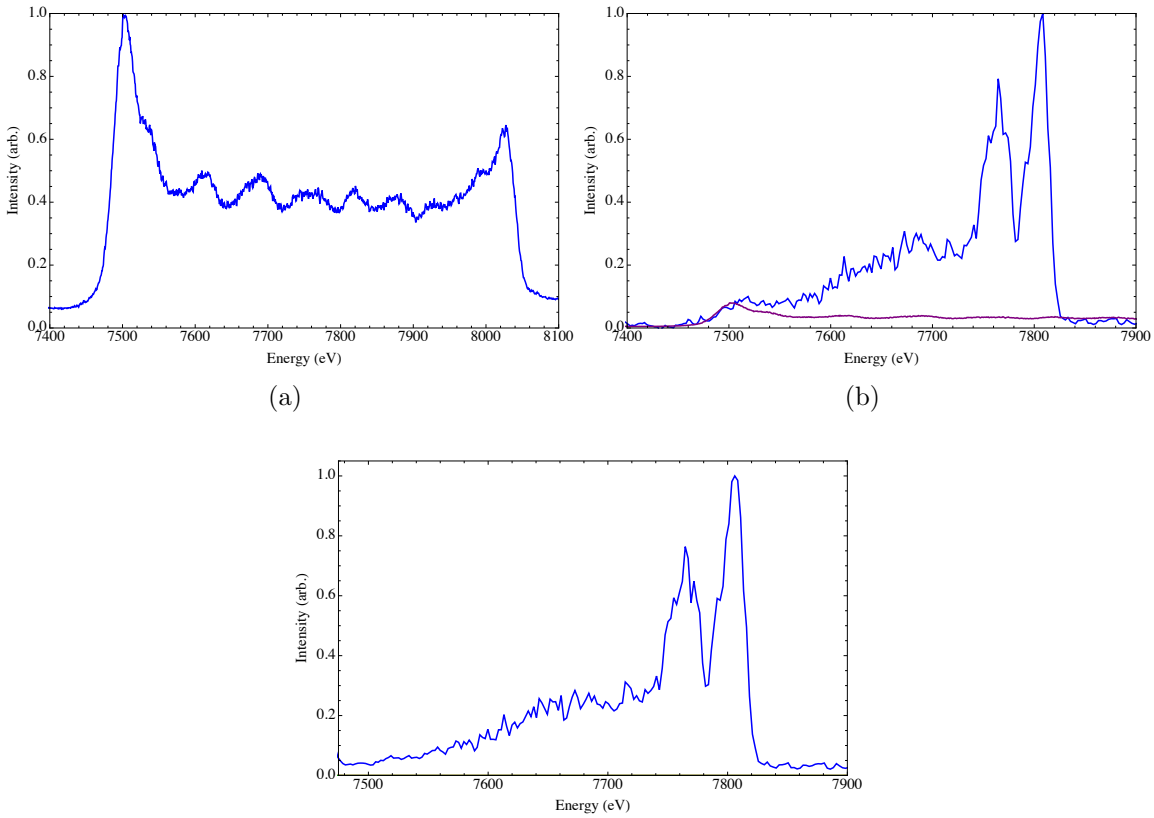

Figure 5.8: The spectrum in (a) is a line out from the flat-field image in Figure 5.7 which has been normalized to unity. The crystal response shows edge defects along with a waviness from form errors in the crystal backing. (b) A sample scattering spectrum (blue curve) and the calibrated background (purple curve). The result from the background subtraction is shown in part (c).

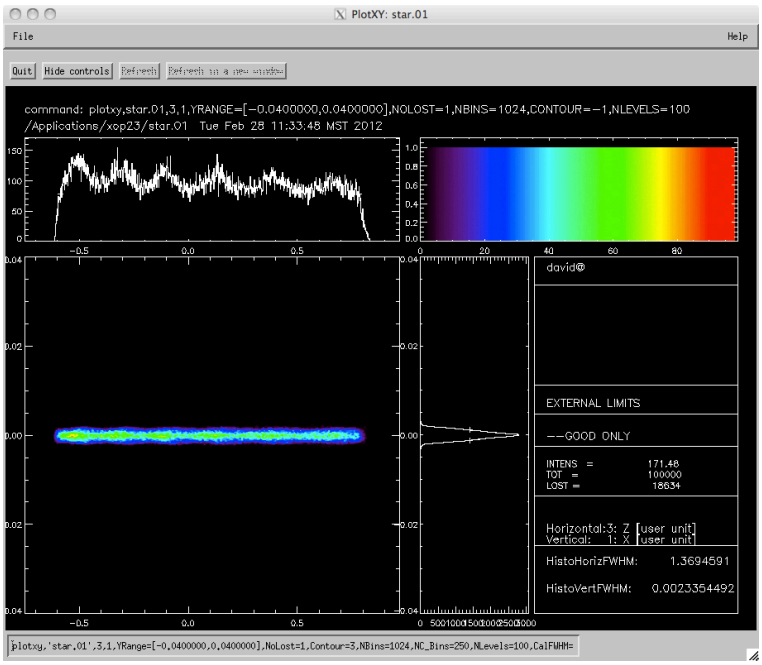

Figure 5.9: The results of a SHADOW raytracing calculation show the effect of crystal form errors on the spectral response. A small amplitude sinusoidal ripple was introduced to the crystal surface. The image shows the results from tracing a broadband point source. The horizontal spectral histogram shows rippling that is similar to that in Figure 5.7

the middle of the crystal where there is the most contact area. On the other hand, the edges and corners have much less contact area holding them in place. Therefore they tend to separate from the substrate and curl up, much like aging or improperly installed wallpaper. This gives rise to the parafocusing effect on the edges.

The flat-field image also shows a sinusoidal variation of the intensity with energy. We performed ray tracing simulations with SHADOW to assess the effect of form errors in the crystal substrate. The flat-field line out shows a total of 6 sinusoidal peaks. Given the crystal horizontal dimension of 30 mm, we introduced a crystal surface error in the form of a sinusoidal ripple with a wavelength of 5 mm and an amplitude of 50 nm. The raytracing analysis used a broadband point source with the resulting image shown in Figure 5.9. This analysis reproduced the nonlinearities seen in Figure 5.8 (a), indicating that crystal manufacturing errors were again the culprit.

Figure 5.8(b), shows a plot of a sample scattering spectrum (blue) and the scaled flat field spectrum(purple). Since the flat-field lacks a spectral reference point for calibration, the horizontal position of the flat field was shifted until the crystal edge defects in the two spectra coincided. The next step was to correct for the different noise levels in the images. When the flat field is correctly scaled, the background level in the region off the crystal (<7450 eV in Figure 5.8(b))should match the background in the scattering. A vertical offset was introduced to the flat field spectrum until these two regions matched. The final step was to divide the scattering spectrum by the calibrated flat field function. This yields the processed spectrum displayed in Figure 5.8 (c).

5.3.3 Control experiment

This target has large amounts of thick gold shielding to block the large background signals from the laser irradiated surfaces. The elastic scattering signal varies as Z_b^2, which is about 50 for gold. Therefore, it is possible to get a comparable background elastic scattering signal from a gold surface that sees an x-ray flux of nearly 1000 times less than is incident on the CRF. The target was desgined to eliminate any possible scattering paths from the gold shielding to the detector. Nevertheless, gaps in the shields or errors in the target fabrication could lead to small x-ray leaks and an amount of background scattering.

To evaluate the sources of background noise in the experiment, we shot a target that lacked the CRF foam. We irradiated the nickel foil with the full compliment of source beams and dropped the drive beams. The only other difference in this target was that we placed a thin (100 μm) CH tamper over the aperture of the collimator to restrict the late-time arrival of nickel plasma from the source.

I show the raw image from this shot in Figure 5.10. A scattering spectrum from the CH tamper is evident in the image. Behind the tamper, in the bracketed region

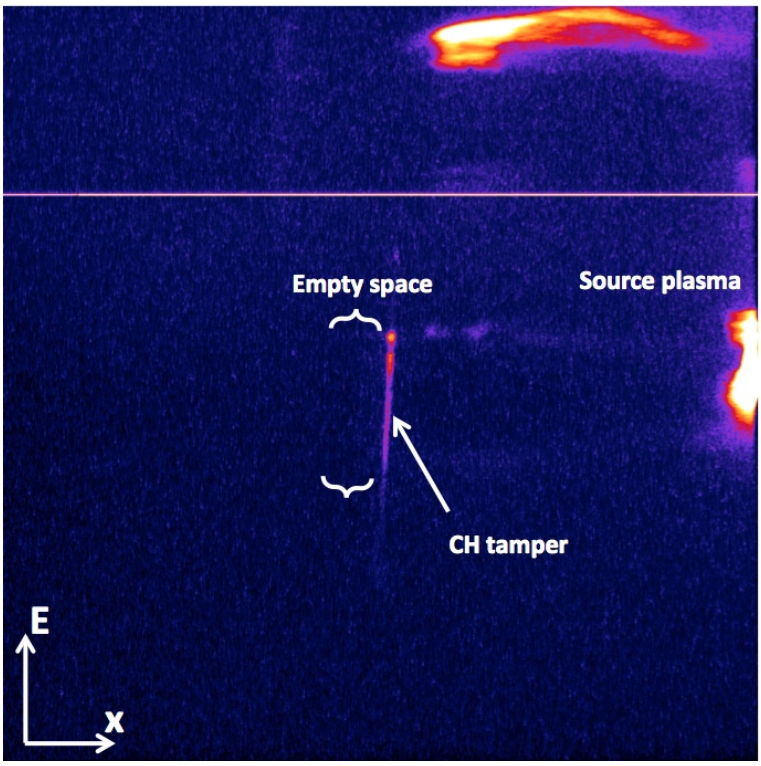

Figure 5.10: A scattered image from a control target that lacked a carbon foam. The control experiment is free from background scattering, with the exception of a signal from a CH tamper that was unique to this target.

normally filled by CRF, there is no signal. This indicates that there is no appreciable source of background in these targets.

5.4 Theoretical scattering profiles

The x-ray scattering code (XRS) code (135; 63; 136; 137) was developed for the purpose of generating theoretical scattering profiles. It does this by computing the DSF. The code is initialized by a user input file that specifies the choice of the theoretical model used for the computation, the material composition, and the plasma conditions. For a known material and judicious choice of a theoretical model, the input plasma conditions are varied until the DSF matches the experimental spectrum. We can then conclude that these "best fit" values are the actual plasma conditions that

generated the experimental spectrum.

The spectral signal on the detector represents a convolution between the power spectrum given as Eq. (3.24) and the finite spatial extent and bandwidth of the x-ray probe.

$$P_{det}(\omega) \propto S(\boldsymbol{\Delta k}, \omega) \otimes I(\omega) \tag{5.4}$$

where $\boldsymbol{\Delta} k$ represents the variation in scattered k vectors and $I(\omega)$ is the spectrum of the x-ray source.

The geometry of the target defines a central scattering angle of 90°. The size of the collimator apertures allows a range of possible scattering angles of ± 8 °. Varying the scattering angle will change the Compton shift and therefore broaden the Compton peak. However, the angular limitation imposed by the collimator made this effect negligible.

In a degenerate plasma, the total Compton profile will be the convolution of the angular broadening and the thermal profile. A thermally Doppler broadened Compton peak will take on a Gaussian shape with a FWHM of (138)

$$\Delta\hbar\omega = \sqrt{\frac{8k_bT\log(2)}{m_ec^2}}\hbar\omega. \tag{5.5}$$

For a electron temperature of 20 eV, the profile will be broadened by 115 eV. As a simplifying assumption, the Compton shifts over the range $\theta = 90\pm8°$ are taken as equally probable which amounts to a boxcar function of width ± 16 eV. The convolution of a Gaussian and a boxcar is two back-to-back error functions. In the limit that the boxcar is much narrower than the Gaussian, the convolved profile will be very close to the initial Gaussian profile. Since the angular broadening is about 4 times smaller than the thermal broadening, the former effect was neglected in the analysis.

A plan was to measure the input spectrum for each scattering shot using the Henway spectrometer, a fixed, absolutely-calibrated spectrometer on Omega. This approach had to be rejected in favor of a direct measurement of the source spectrum with the IXTS. Henway viewed the front, laser-irradiated side of the foil at an angle of 32° from normal. This is in contrast to the foam, which viewed the source from the rear of the foil. The different plasma opacities along these lines-of-sight can affect the relative intensities of the x-ray peaks. This was evident in the Henway data as the ratio of the intensities of the two heliumlike nickel x-ray lines was noticeably different from that of the scattering data. The Henway spectrometer uses a thick PET crystal, which has a much different spectral response than the IXTS. This is evident in the reduced resolution from source and depth broadening (92), which makes it impossible to fit the higher resolution data that was recorded by the IXTS.

To measure the input spectrum of the x-ray source, we performed a dedicated "source shot" in which the IXTS viewed a nickel foil that was driven with six Omega beams. This experiment was part of a shot day the author participated in on August of 2012 and is primarily the work of Katerina Falk of LANL. The IXTS observed the x-ray emission from the backside of the foil such that the normal to the foil was colinear to the source-to-crystal vector. We chose this geometry and the intensity of the laser spot to try to match the conditions in which the foam views the x-ray source. A spectrum from the source shot is shown in Figure 5.11. The effect of the plasma temperature and opacity is easily demonstrated by comparing Figure 5.11 to the underdriven heliumlike nickel spectrum from the Trident campaign, Fig, 4.9 (a).

Since the IXTS was directly viewing the laser spot, the greatly increased brightness as compared to a scattering signal made it potentially very easy to saturate and possibly damage the CCD. We put an additional 25 μm of iron shielding on the front aperture of the IXTS to cut the intensity of the source by approximately 10^{-3}. Coupled with a reduced laser energy of 2.2 kJ, the maximum value on the CCD from

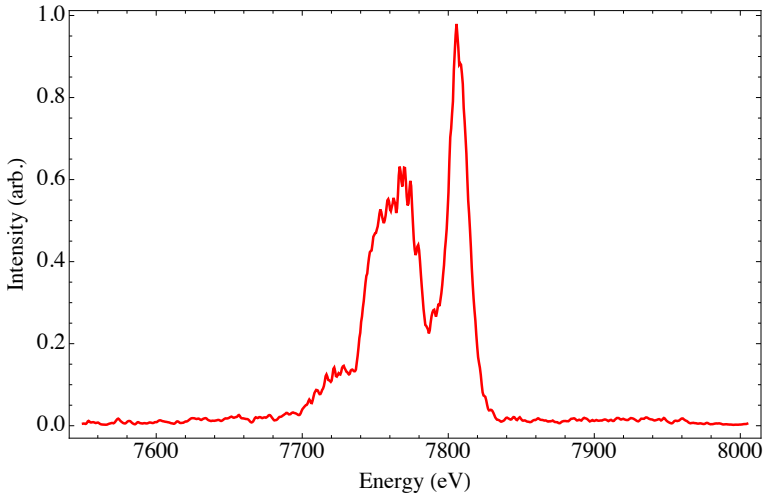

Figure 5.11: A direct measurement of the spectrum of heliumlike nickel was used as the input for the calculation of the theoretical scattering profiles.

the nickel spectrum was about half of saturation.

5.5 Fitting the data

I used the XRS code and the experimental nickel spectrum to compute theoretical scattering profiles over a two dimensional parameter space created from varying the temperature and ionization inputs. The temperature space spans 0-60 eV with 1 eV steps while the ionization goes from 0 to 6 in steps of 0.1. This is 3600 points, which took 15 hours of computation time on a personal computer.

For each scattering spectrum, χ^2 was computed as the weighted differences between the experimental values I_{exp} and the theoretical values I_{DSF}.

$$\chi^2 = \sum_{i=1}^{k} \frac{(I_{exp} - I_{DSF})^2}{I_{exp}} \tag{5.6}$$

where k is the number of spectral resolution elements in the spectrum. The best fit was defined as the theoretical spectrum that minimized χ^2. This reveals the inferred values for temperature and ionization of the plasma at a point in space. A basic

condition for the validity of this analysis is the presence of a unique overall minimum in the χ^2 map.

Figure 5.12 shows the results and supporting data from the fitting procedure as it is applied to the spectrum from the spatial position of the peak of the shock compression in shot 65401. In Figure 5.12 (a), the position of the lineout relative to the entire image is indicated. To help orient the image, note that the shock is driven from the top of the image. The box bordered by a green dotted line is the spatial integration volume. The experimental lineout are plotted as the blue curve in Figure 5.12 (b) with the best fit theoretical spectrum (red) revealing a $T_e = 25$ eV, $Z = 2.3$. The sensitivity to the fits to varying the temperature and ionization is demonstrated in Figure 5.12 (c) and (d). Finally, the χ^2 map is shown in Figure 5.12 (d). There is an overall minimum at the best fit values which is surrounded by compact contours of increasing χ^2. The artifact in the map at Z=1 and T_e=0-14 eV is a bug in the XRS code that overall did not have an effect on the best fit values.

I established the error bounds on the best fit values by fitting to the upper and lower bounds of the variation in the data points. This is not as rigorous as using the χ^2 value to compute the p-value and confidence interval. However, this is not possible since a closed form does not exist for the DSF. The error bars thus represent the range of possible inferred temperature and ionization values that encompass 1σ of the variation in the data.

I used the analysis method to process the scattered spectra over the spatial extent of the scattering aperture. For the shocked foam, the fitting procedure failed in two regions. In the rarefaction far enough away from the shock, the density drops such that the SNR is too low to meaningfully discern between different theoretical fits. In the region just ahead of the shock, the temperature varies rapidly with the position. The signal inside a resolution element is then a non-equilibrium average of the cold, upstream foam and the shock heated foam. The χ^2 map of the fits in this region

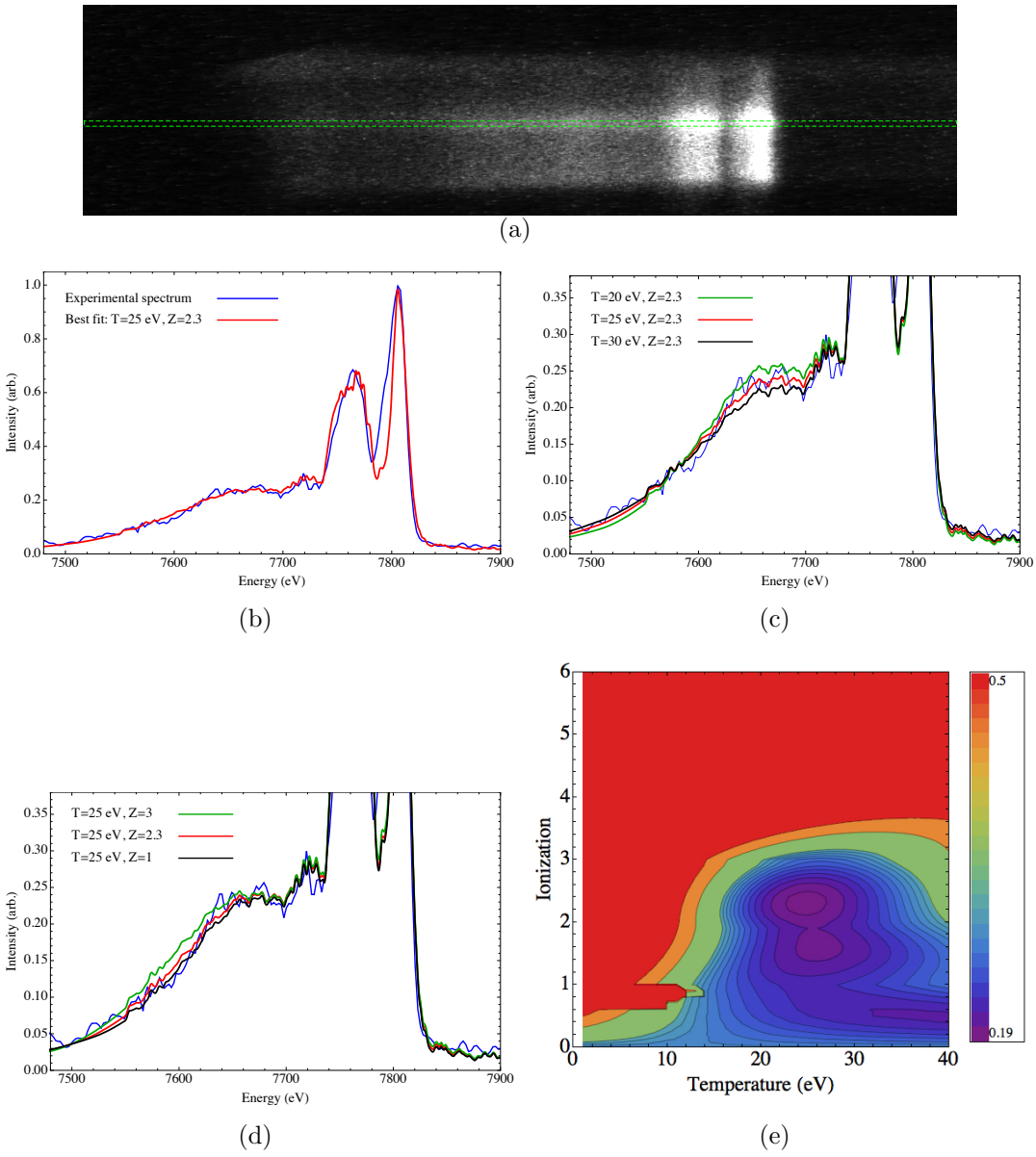

Figure 5.12: (a) Shows the position of the lineout across the position of maximum compression in shot 65401. (b) The best fit (red) of the experimental lineout(blue) reveals values of $T_e = 25$ eV, $Z_f = 2.3$. Shown in (c) is the the effect of varying the temperature while keeping the ionization constant and vice versa in (d), to establish the error bounds in the inferred values. (e) A contour map of the χ^2 values from the fits demonstrates that the best fit occupies a unique minimum.

do not converge to physically reasonable values. Analysis of this region is possible, but it requires knowledge of the composition of a resolution element to inform a multiple-temperature fitting method.

A summary of the experimentally determined temperature-ionization values is shown in Figure 5.13. In comparison, also plotted are the results from the atomic EOS simulation code FLYCHK (139). Collisional effects are likely predominant for this system, in which the ionization state is set at a given temperature by competition between collisional and photoionization and two and three body recombination. The ionization state is thus dependent on the material density as the various collisional ionization and recombination rate coefficients are proportional to the electron density.

The FLYCHK simulations in Figure 5.13 are calculated at three different densities for an uncompressed foam, the shocked layer, and far into the rarefaction. These values were chosen based on the measurements of the blast wave density profile presented in Section 5.7. The data from the shock-compressed region show good agreement with the modeling regardless of the density. However, FLYCHK underestimates the degree of ionization in the rarefaction. This may be because the rarefaction is driven out of equilibrium by the deposition of energy from x-rays or suprathermal electrons from the hot plasma created by the laser drive.

5.6 Assessing models for the bound-free

The XRS code includes multiple models for calculating the bound-free component of the scattering. In the version used for this analysis (v.5.0.1), the method is selectable between the form factor approximation (FFA), impulse approximation (IA), and the IA including the Compton defect. Previous versions of the XRS code lacked this capability and instead relied solely on the FFA. This approach has been used to analyze data in previous non-collective x-ray scattering experiments (73; 68; 70; 69). However, these experiments lacked a strong bound-free component as the remaining

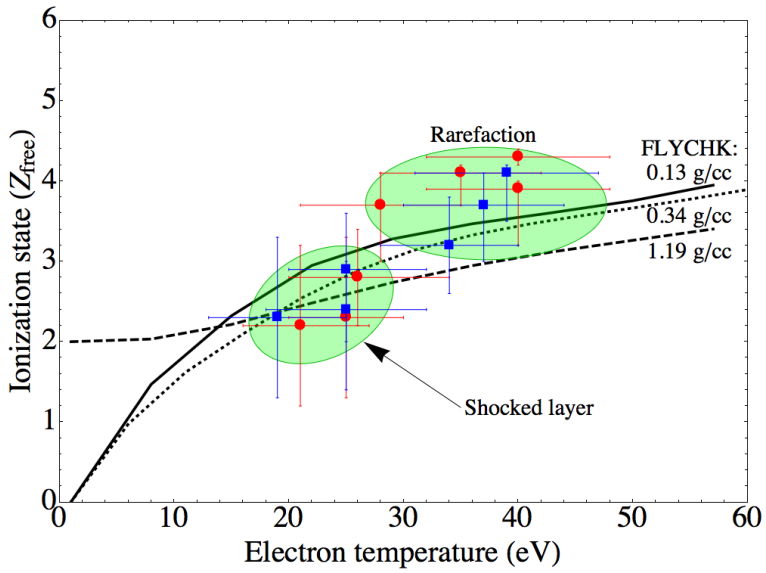

Figure 5.13: The points show the measured temperature and ionization values from the shocked foam. The solid, dashed, and dotted lines are FLYCHK runs at $\sim \frac{2}{5}$, 1, and 3.5 times the initial foam density, encompassing the range of observed densities. The points are grouped into either the shocked layer or rarefaction according to whether they originate from a spatial position where there is a net compression or expansion, respectively.

bound electrons were held too tightly to be accessed by Compton scattering.

In this experiment, all four of the carbon L-shell electrons could be accessed by Compton scattering and the atoms ranged from approximately neutral to fully stripped of the outer shell. The plots in Figure 5.14 (b)-(d) show scattering spectra from over this range of ionizations and theoretical fits calculated using the IA and FFA. The calculation using the FFA did not yield theoretical spectra that fit the data for any choice of parameters. Therefore, the best fit values were taken from the IA fits and compared to the same spectra from a FFA calculation.

Based on the experience of previous work, the present data was first analyzed using the FFA. However, the χ^2 plots of the fits failed to converge to physically meaningful values. This is especially evident in the FFA fit to the upstream scattering spectrum in Figure 5.14 (d). The foam has not yet been perturbed by the shock, so it should not be strongly heated and at a low ionization state. Since the free-free component

is small compared to the bound-free, the Compton peak is insensitive to the free electron temperature. Therefore, the ionization state is the only free parameter for the fit. The FFA fit is calculated for a low ionization state, but the FFA fit fails to match the experimental data for any choice of ionization state. The FFA fits give bound-free spectra that are consistently offset by about -25 eV relative to the free electron Compton shift of Eq. (3.3). This is consistent with the work of Mattern and Seidler (140) who show evidence that this erroneous shift is likely due to the fact that the FFA does not conserve energy.

The FFA is of limited use to describing the scattering in which there is a significant contribution from Compton scattering from weakly bound electrons. In the upstream fit in Figure 5.14 (d), the low ionizations (and large contribution from bound-free scattering) creates a large disagreement between these two models. As the ionization increases, the two fits become superimposed. However, this is only because the number of weakly bound electrons decreases, thereby reducing the effect of the shifted FFA bound-free peak. In the nearly heliumlike state of the carbon in the rarefaction the two fits are indistinguishable and fit the data well as there is no bound-free component left.

The IA yielded fits that yielded reasonable, unique values for the temperature and ionization. The calculation of the Compton defect showed it to be a minor effect, shifting the Compton peak by 5 eV towards higher energies. Therefore, the best-fit values reported in this work use theoretical form factors based on the IA calculation of the bound-free component.

5.7 Shock compression

Since the IXTS images along the shock propagation direction, the image intensity provides information of the material density. The ion density is related to the electron density through the ionization $n_e = Zn_i$. By Eq. 5.2 the intensity of the elastic

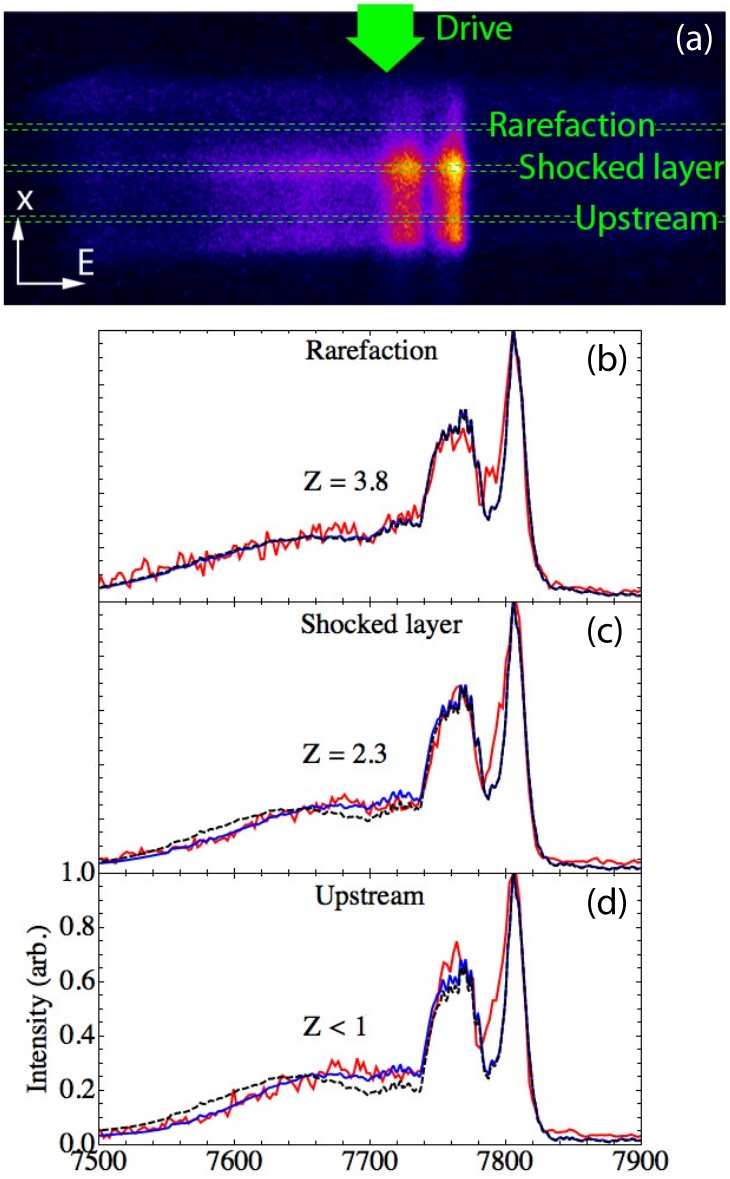

Figure 5.14: Sample spectra and fits taken from the scattered image (a) at positions yielding a strongly heated (b), moderately heated (c), and cold fluid (d). The red lines are the experimental lineouts and the blue lines are the best-fitting theoretical spectra calculated using the IA. The FFA (dashed lines) fails to meaningfully fit the data. The experimental spectra are normalized to the height of the elastic peak.

scattering varies as

$$I_{elastic}(x) \propto \rho(x)|f_I(k) + q(k)|^2 S_{ii}(k) \tag{5.7}$$

with $\rho(x)$ the mass density of the shock along the propagation direction.

For the parameters of this experiment, the bound charge is $|f_I(k) + q(k)| = 1.8$ and $S_{ii}(k) = 1$. This means that the elastic scattering intensity is independent of the material conditions until $Z_{free} > 4$ and the inner shell electrons start to become significantly ionized. At this point, the bound charge decreases and the elastic scattering intensity drops quickly. The previous section has demonstrated that the ionization stays below this level from the upstream foam to at least 240 μm behind the shock. The large potential barrier to ionize the core electrons likely precludes any more ionization in the remaining low-density material that is visible through the scattering aperture. Therefore, the spatial profile of the elastic scattering intensity depends only on the material density. A lineout across the elastic scattering yields a 1D, monochromatic map of the material density profile that is similar to radiography average along the line of sight where scattering x-rays are present.

Figure 5.15 shows a comparison of the elastic scattered imaging between a driven and an undriven shot. The shock is visible as an increase in the intensity of the scattered signal midway through the foam. Using Eq. (2.15) and a reasonable choice of $\gamma = 1.4$ - 1.66 for a shock in a low-Z material (15), the shock compression should be about four to six. At first glance, the observed compression appears to be significantly less than this.

With an observed compression of R_{obs}, the actual compression R_{act} is somewhat greater due to the photoattenuation of the scattered x-rays as they escape radially through the denser shocked material. This model assumes that the shock compresses the foam uniformly over the spot size r_{spot} of the drive lasers and there is unperturbed

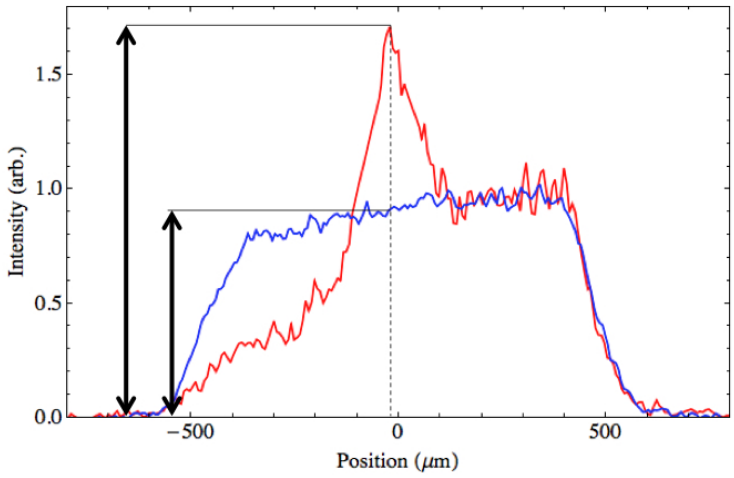

Figure 5.15: Spatial lineouts of the elastic scattering from the undriven foam (blue) and shocked foam at a probe delay of 8.2 ns. The lineouts are normalized so that the amplitude of the scattering from the upstream foam in the driven shot is equal to the undriven foam. The peak shock compression is ~ 1.9 and is equal to the ratio of the lengths of the longer arrow to the shorter.

foam beyond that. This assumption is valid because the 2D structure at the edges of the laser spot lags the 1D motion of the shock. The observed compression is then simply the actual compression modified by a photoabsorbtion factor,

$$R_{obs} = R_{act} e^{-\mu_{photo} r_{spot} (R_{act} - 1)} \tag{5.8}$$

where μ_{photo} is the linear attenuation coefficient for photoelectric absorption in the foam. The solution to Eq. (5.8) takes the form of a Lambert W function

$$R_{act} = -\frac{W(-\mu_{photo} r_{spot} e^{-\mu_{photo} r_{spot}} R_{obs})}{\mu_{photo} r_{spot}} \tag{5.9}$$

For the observed compression of 1.9, a spot size of 412 μm, and $\mu = 1.6$ cm^{-1} for the 0.34 g/cc foam, the actual compression is then 2.0. It is important to note that this analysis neglects the motion blurring from the movement of the shock under the duration of the x-ray probe. A compression of 2.0 represents a lower limit for the

peak shock compression. In the next section, a more sophisticated analysis is shown which uses realistic shock profiles to better infer this value.

5.7.1 Self-similar analysis of the blast wave spatial profile

The following analysis predicts the range of possible values for γ through a comparison of theoretical self-similar density profiles to the experimental data. To first order, the weakly coupled system under consideration can be approximated as an ideal gas. This is supported by the general agreement between Hyades calculations using an ideal gas EOS and SESAME tables for polystyrene and carbon that shown in Figure 5.3

The motion of the blast wave can be modeled analytically using a self-similar analysis. The experimental arrangement is quite similar to the planar impulsive load problem considered by Zel'dovich (141), Adamskii (142), and Zhukov and Kazhdan (143) in a series of closely related papers. A fluid that is initially at rest is hit with a short-duration source of energy with some short time duration τ. This impulse creates a shock which propagates down the fluid, while the downstream material expands into vacuum. We consider the motion of the resulting blast wave at some later time $t >> \tau$

The position of the shock front is taken as a power law with time

$$X(t) = At^{\alpha} \tag{5.10}$$

with scaling constant A and similarity exponent α. The problem is expressed in Eulerian coordinates with a dimensionless similarity variable

$$\eta = m/M. \tag{5.11}$$

Here $m = \int_{-\infty}^{x} \rho_0 dx$ is the mass of fluid per surface area that is behind the Eulerian

coordinate x and $M = \rho_0 X$ is the mass per surface area swept up by the shock front. The pressure, velocity, and density are expressed in terms of the variables as

$$P = B\rho_0 M^{-n} f(\eta) \tag{5.12}$$

$$u = \sqrt{B} M^{-n/2} w(\eta) \tag{5.13}$$

$$\rho = \rho_0 q(\eta) \tag{5.14}$$

with dimensionless functions $f(\eta)$, $w(\eta)$, and $q(\eta)$ and a new similarity exponent $n = 2(1-\alpha)/\alpha$ and proportionality constant B.

These reduced functions may be substituted into the Euler fluid equations, which yields the following set of algebraic-differential equations for the three dimensionless functions, which Adamskii (142) gives as

$$q(\eta) = \frac{\gamma+1}{\gamma-1}((\eta^n f(\eta))^{1/\gamma}) \tag{5.15}$$

$$\frac{n}{2} w(\eta) + \eta \frac{dw(\eta)}{d\eta} = \sqrt{\frac{2}{\gamma+1}} \frac{df(\eta)}{d\eta} \tag{5.16}$$

$$\frac{dw(\eta)}{d\eta} = -\sqrt{\frac{\gamma+1}{2}} \frac{\gamma-1}{\gamma+1} \eta \frac{d}{d\eta} \left[(\eta^n f(\eta))^{-1/\gamma} \right]. \tag{5.17}$$

This set are subject to the initial conditions $f(1) = 1$, $q(1) = 1$, and $w(1) = \sqrt{2/(\gamma+1)}$.

These equations admit an analytical solution for the case $\gamma = 7/5$ with n= 4/3. This solution describes a diatomic gas, which is quite useful for analyzing explosions in air. In the present experiment, the value of γ may be different as the carbon is monoatomic and in the ionizing regime.The preceding set of equations was solved numerically for arbitrary γ using the computed values of n given by Voloshinov and Fal'kovich (144).

The self-similar profiles were used as inputs to a simple ray-tracing model to account for the absorption of the x-rays by the foam, motion blurring during the

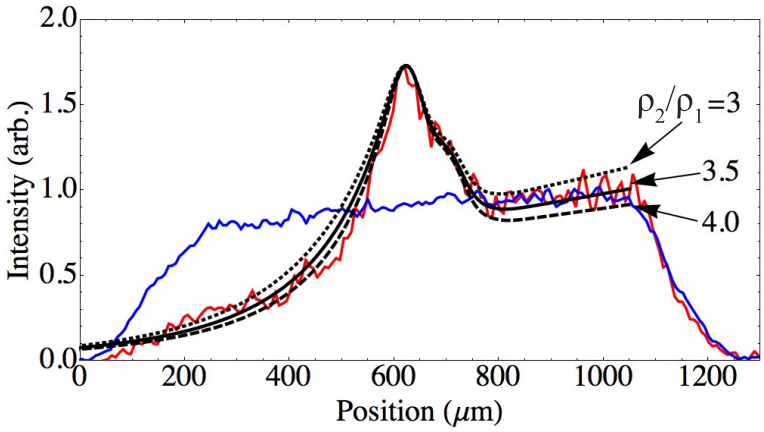

Figure 5.16: The red line shows the experimental elastic scattering imaging at 8.2 ns as compared to the self-similar computations of the material density profile with $\gamma = 2$ (dotted), $\gamma = 1.8$ (solid), and $\gamma = 5/3$ (dashed).

finite duration of the probe x-ray pulse, and finite resolution of the diagnostic.The adiabatic index was varied to match the intensity profile of the shock. It is important to note that the compression will be correctly modeled only if the the theoretical curve matches the data throughout the blast wave.

In fitting the profile, we must somehow account for the gradual increase in apparent compression ahead of the density maximum. The next section will show that this effect is too large to be explained by tilt or curvature of the shock front in the non-imaging direction. To do so, some small amplitude shocks are introduced to the theoretical profiles to fit the material leading the main peak. These could be produced from inhomogeneities in the foam structure or voids in the drive surface. The presence of these leading shocks suggests that the temperature and ionization values from the spectral fitting are affected by structure in the shock front and thus do not describe a single thermodynamic state. However, quantitive evaluation shows that this contribution to the scattered spectra is small.

The results of this procedure are displayed in Figure 5.16 as compared to the elastic imaging of the shocked and unshocked foams. Consistent with Figure 5.15, the scattering profiles are normalized to the right edge of the lineout. This process

yields a compression of $\rho_2/\rho_1 = 3.5 \pm 0.5$ times, which corresponds to $\gamma = 1.8 + 0.2/-0.14$. The upper and lower error bounds on the compression were found by fitting to the limits of the variation in the lineout.

This range of compressions are lower than might be expected from the strong shock limit (15); this might be a consequence of preheat of the foam upstream of the shock. In comparison to EOS experiments on plastic foams (145; 48), this target lacked a preheat shield. Other experiments that found compressions of 5-6 times in CRF foam either probed a shock driven by a significantly lower laser intensity (146) or much further from the drive surface (147) both of which would tend towards lower amounts of preheat.

5.7.2 Higher order structure

Another explanation for the shock profile is that there might be significant two or three dimensional structure in the shock. This could lead to mixing of the shocked and unshocked foam within a resolution element. Each of these explanations are considered in relation to the observations at hand.

The DPP on the drive beams produces a laser spot with a super gaussian profile. The lower intensity at the edges of the laser spot tends to produce a curved shock front. If there is significant curvature, the spatial resolution elements at the shock front could partially integrate over unshocked material, lowering the inferred average density. Using Figure 5.5, at the position of the shock at 8.2 ns, 74% of the x-rays are within the diameter of the collimator. The maximum radius of the beam increases from 250 μm to about 320 μm. Using the known intensity profile of the laser spot, at the edges of the x-ray beam the laser intensity driving the foam is 10% less than the center. By Eq. 2.13 and 2.14, the shock velocity scales with the laser intensity as $u_1 \propto I^{\frac{1}{3}}$. One would expect a 3.4 % lower shock velocity at the edges of the region illuminated by the x-ray probe beam, meaning the edges would lag the center

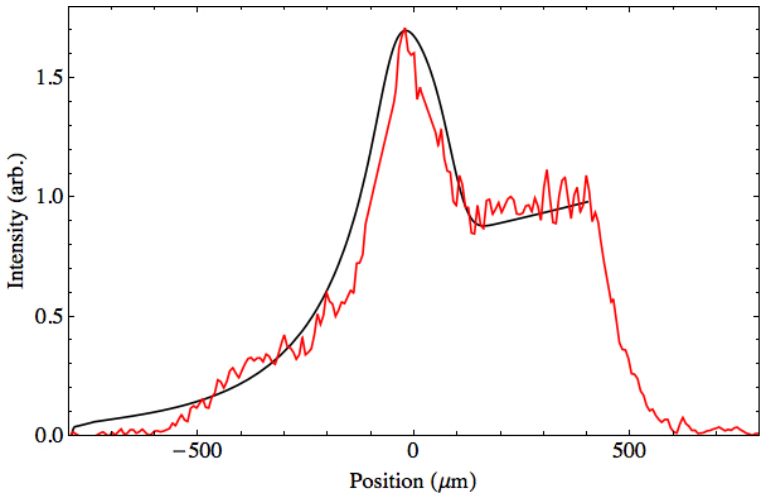

Figure 5.17: By tilting the 1D self-similar profile (black) for $\gamma = 5/3$ by 18°, the shock compression of 4 may be matched to the experimental profile (red.) The resulting theoretical profile predicts a wider than observed shock compressed region.

by about 20 μm. This is below the spatial resolution of the IXTS, so effects from curvature are likely not observable.

The results of previous experiments (148) showed that a blast wave may be tilted relative to the propagation direction which is set by the normal of the laser driven surface. The author concluded that the shock was tilted by 8°through the analysis of a two dimensional x-ray radiograph. In the present experiment the IXTS images in one dimension and spatially integrates along the other. Applying one dimensional imaging to a tilted shock will result in the mixing of shocked and unshocked material within a resolution element, thereby reducing the apparent compression.

To evaluate the possibility of a tilt reducing the apparent shock compression, a self-similar profile for $\gamma = 5/3$ was used to generate a two-dimensional image which was then rotated until the compression matched the experimental profile. A value of $\gamma = 5/3$ was chosen for this model as it is the upper limit of the compression found in the analysis in the previous section. The results of the tilt analysis are shown in Figure 5.17, where a tilt of 18° was necessary to match the compression. Based on

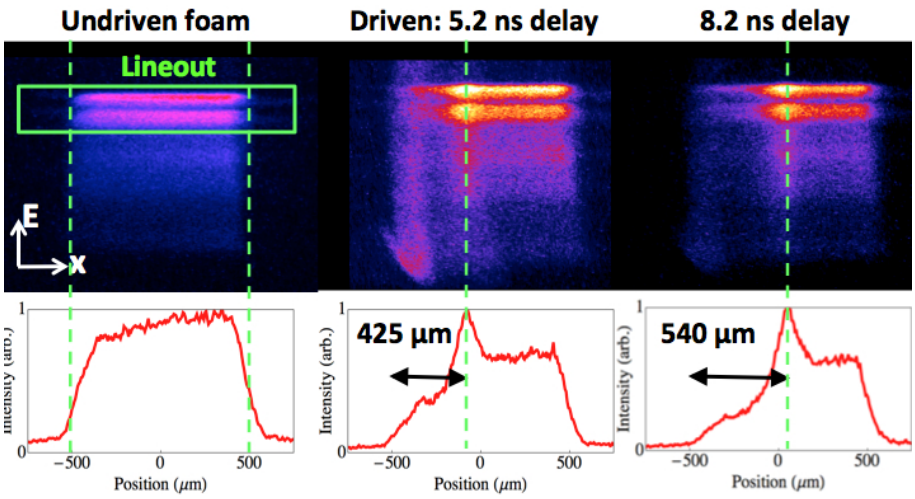

Figure 5.18: The 1D imaging of the elastic scattering intensity allows for tracking of the shock position in time. Note that the position is given relative to the center of the scattering aperture.

the accuracy of the target alignment, this amount of tilt is unreasonable. The shock should be launched perpendicular to the drive surface and this large a misalignment would have caused the source beams to miss their target. The compressed region in the tilted profile is too wide in comparison to the experimental data. Reducing the tilt will decrease the width of the shocked region, but at the expense of the getting the correct peak compression.

5.7.3 Measuring the shock velocity

By varying the delay of the probe beams, we can track the movement of the shock in time. Aside from the nominal delay of 8.2 ns, we reduced the delay to 5.2 ns and observed the shock retarded by 120 ± 35 μm. We can therefore infer an average shock velocity over this interval of 40 ± 12 μm/ns.

5.8 Self-consistency and comparisons to simulations

A basic test for the validity of these measurements is whether the temperature inferred by the shock velocity and compression is consistent with the values from the fits to the scattered spectra. Combining the jump conditions for mass (2.9) and momentum (2.10) across the shock, the ratio of the shock driving pressure to density may be written as

$$\frac{P_2}{\rho_2} = \frac{\rho_1}{\rho_2}\left(1 - \frac{\rho_1}{\rho_2}\right) u_1^2 \tag{5.18}$$

where the upstream pressure drops out via the strong shock limit. Substituting this equation into the ideal gas law (2.1) yields

$$k_B T = \frac{A m_u}{1+Z}\frac{\rho_1}{\rho_2}\left(1 - \frac{\rho_1}{\rho_2}\right) u_1^2 \tag{5.19}$$

The temperature depends on the shock speed u_1, compression ρ_2/ρ_1, and ionization Z, all of which have been measured in this experiment. For a fixed ionization and shock speed, this equation tells us that the temperature peaks for a compression of 2 and monotonically decreases for larger compressions.

With the compression and shock speed from the elastic imaging and using the Thomas-Fermi model (149) for the ionization state, Eq. (5.19) can be iteratively solved for an independent measurement of the temperature and ionization in the shock. The Thomas-Fermi model was used to constrain the ionization to equilibrium with that temperature because of the large experimental uncertainties in the x-ray scattering measurement of the ionization state. For this weakly coupled system, this model should give approximately correct results.

The elastic imaging thus yields values of T = 17 ± 7 eV and Z =1.8 which compares favorably with the average results inferred from the scattering spectra of $T_e = 22 \pm$

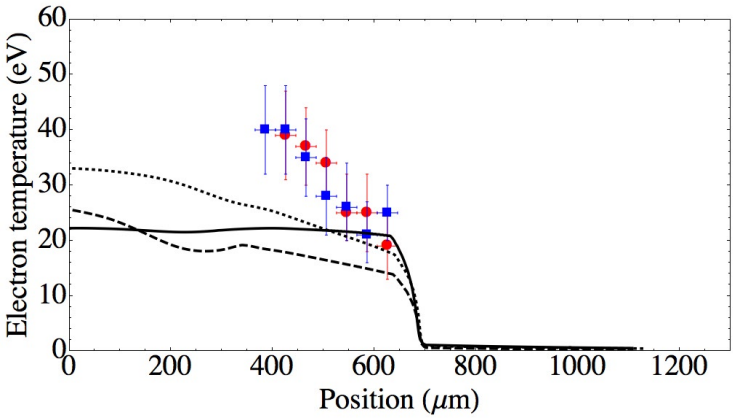

Figure 5.19: Data points show the results of the imaging XRTS measurements of the temperature profile of the blast wave at 8.2 ns. The lines are the results of HYADES simulations that were computed using the ideal gas (solid), polystyrene (dashed), and carbon (dotted) equations of state.

5 eV and Z = 2.3 ± 1. Therefore, at the shock front, the measured bulk properties from the elastic imaging are self-consistent with the microscopic quantities from the spectrally-resolved x-ray scattering.

Figure 5.19 (a) shows a comparison between the temperature measurements from x-ray scattering and the results from HYADES (150) simulations. The simulations were computed with three different EOSs from the Los Alamos SESAME tables (37): a polytropic gas with index chosen to match the experimental compression, polystyrene, and carbon. Given the high carbon content, the EOS of CRF is likely similar to pure carbon. Polystyrene is similarly 92 % carbon by weight, so it present a useful comparison. Each simulated temperature profile was motion blurred over the 1 ns duration of the probe laser pulse by weighting with respect to the simulated density profile. Because HYADES is a one dimensional code, it cannot account for the radial heat transport that reduces the ablation pressure (151). The laser intensity in the simulations was therefore reduced by 35-50% to match the experimental shock positions.

The difficulty in simultaneously matching all the observed profiles in the simu-

lations points to the value of such data. The ideal gas computation, adjusted as described above, gives the best agreement with the temperature, compression, and shock speed. For a cold upstream material, the polystyrene EOS predicts a compression of 4.2 and therefore requires a preheat of 4 eV to match the data. However, the temperature in the shocked material is too low and the shock velocity is overestimated as 60 μm/ns. The simulation using the carbon EOS better matches the temperature and shock speed, though the predicted strong-shock compression of 5.5 times requires almost double the preheat as the polystyrene case to match the data.

Assuming that 1% of the laser energy couples to the creation of a hot electron population at a temperature of $\sim$60 keV, the model of Kanaya and Okayama for electron energy deposition as a function of penetration depth (152) was used to estimate the feasibility of these levels of preheat. Given the large uncertainty in the laser-electron energy coupling, this calculation is perhaps accurate to within a factor of ten. At a position 600 microns away from the drive surface this model yields a temperature to be about 3 eV, which supports the explanation of relatively large levels of preheat in the foam affecting the compression.

In all cases, the experimental temperatures in the rarefaction are higher than in the simulations. A possible explanation is that the coronal plasma beyond the ablation surface provides an additional source of heating, not accurately captured by the flux-limited, single-group-diffusion heat transport model in the code.

5.9 Conclusion

This chapter has presented an experiment using imaging x-ray Thomson scattering to produce the first simultaneous measurements of the spatial profiles of the temperature, ionization state, and relative material density, and the shock speed, for an unsteady shock at high energy density. These experiments are the first to provide a measurement of the temperature of a shock driven in a near solid density, optically

opaque carbon sample in HEDP conditions and form the basis for later investigations of heavier materials. The x-ray scattering measurements of the temperature in the shock are shown to be self-consistent with estimates based on the shock velocity and compression from elastic imaging. This combined technique, which is unique to imaging x-ray Thomson scattering, helps bolster the validity of x-ray scattering as a diagnostic method. The somewhat low values inferred for the compression and the high ionizations in the rarefaction may indicate greater than expected strength of preheat effects from nonlocal heating. These effects may be explored in future experiments by including a thin layer of a high-Z material to act as a preheat shield. The spatially-resolved nature of the measurement would then allow differentiation between the scattering from the preheat shield and the shocked foam.

CHAPTER VI

Conclusion

The properties and dynamic behavior of material systems at high energy density are relevant to an enormous range of physical systems, including astrophysical equations of state (153), astrophysical dynamics (154), and inertial confinement fusion (4). Ideally laboratory experiments in this regime would employ only well-understood materials to eliminate uncertainties stemming from the material properties. For examples, fluid instability experiments may be scaled to astrophysical systems by matching certain dimensionless fluid parameters, the magnitude of which depend on the thermodynamic state of the materials (155). In practice experiments often rely on materials such as foams and aerogels where there are significant uncertainties in the EOS (151). They are used because there is a factor of 100 in density, from about 0.01 g/cm^3 to 1 g/cm^3, over which these porous solids are nearly the only practical choice. Studies have typically been unable constrain the theoretical description of such materials by simultaneous measurements of multiple properties in the presence of one dimensional gradients in the heating.

In the previous chapters I have described the design of an experiment to measure the spatial profile of the thermodynamic state of a blast wave driven in a dense medium. This was made possible through the first experimental implementation of the technique of imaging x-ray Thomson scattering using a doubly-curved x-ray crys-

tal spectrometer (33). The x-ray scattering measurements of the temperature in the shock are self-consistent with estimates based on the shock velocity and compression from elastic imaging. The somewhat low values for the inferred compression may reflect preheat of the foam upstream of the shock. This may be explored in future experiments by including a thin layer of a high-Z material to act as a preheat shield. The unique spatially-resolved nature of the measurement would then allow differentiation between the scattering from the preheat shield and the shocked foam.

6.1 Future work

There has been interest in the HEDP community for developing a higher resolution version of the imaging spectrometer. With a resolution on the order of 10 μm, experiments could be designed to probe the temperature jump at the leading edge of a shock or the very high densities produced at the interface of colliding shocks.

There are a number of technical challenges to implementing these high resolution measurements. As I have demonstrated, there is generally a tradeoff between resolution of signal level. For example, motion blurring can be reduced through using a shorter probe laser pulse which will result in a lower x-ray yield. Alternatively, a crystal that is wide along the focusing direction will gather more light, but at a cost of a lowered spatial resolution by introducing more spherical aberration. In creating the IXTS, I used these considerations to optimize the design in light of the constraints of the Omega target chamber.

Achieving this kind of resolution will require solutions to alleviate the zero-sum nature between resolution and signal. This can come from advances in the x-ray probe and the imaging crystals. Recent years have seen the emergence of a number of large, hard x-ray free electron lasers (FEL) around the world, such as the Linac Coherent Light Source (LCLS) at SLAC, the SPring-8 Angstrom Compact free electron laser (SACLA) at the RIKEN SPring-8 Center, and the European x-ray free electron laser

(XFEL) at DESY. These facilities are designed to produce intense bursts (10^12 - 10^13 photons) of monochromatic, hard x-ray photons (2-20 keV) focused to a sub-micron beam with a duration of less than 100 fs. These properties would largely eliminate motion and k-vector blurring while limiting the scattering to the narrow FEL beam to eliminate astigmatism inherent in the crystal.

High-resolution x-ray scattering measurements in HEDP regimes can be realized by combining an FEL with optical lasers. This is the case in the Matter in Extreme Conditions (MEC) station at the LCLS and the planned Helmholtz International Beamline for Extreme Fields (HIBEF) at the XFEL.

With the somewhat more flexible nature of these facilities, it should be possible to increase the spatial resolution of the crystal by increasing the magnification and the Bragg angle. The resolution could also benefit by exploring alternative geometric schemes. The focusing of the x-rays happens over the vertical, circular curvature of the crystal which inevitably creates spherical aberration in the image. A elliptical surface will give true point-to-point focusing, though creating the necessary elliptical toroid substrate may prove technically challenging. However, the technique of magnetorheological finishing could potentially be used to create these complex surfaces. An elliptical crystal could then be made wider along the focusing direction to gather more scattered light with no loss in resolution.

APPENDICES

APPENDIX A

Electronic measurement of microchannel plate pulse height distributions

A.1 Introduction

Microchannel plate (MCP) based framing cameras are often used to image swiftly moving hydrodynamic flows. A radiograph is formed by backlighting the plasma with x-rays. In contrast to most other applications of MCPs where they are used to count discrete pulses, high-energy-density physics experiments typically use MCPs as analog imagers.

A primary photoelectron from a detected x-ray is amplified by a cascade process yielding an average gain $\sim 10^4$ (156). The variation in the gain from the detection of single x-ray photons is characterized by a pulse-height distribution (PHD). The PHD from a single MCP has been described by a negative exponential (157; 158). The PHD in turn contributes to the noise in the image. The noise has been assumed to scale with the Poisson statistics of the input photons as in direct film exposure(159).

While the noise in framing cameras has been measured optically (160), we present a direct measurement the electron output of a MCP. From the MCP PHD, is possible to compute the signal-to-noise ratio (SNR) of a uniformly illuminated region. Naturally, in applications one desires to achieve the largest possible SNR. Understanding

the physical basis of SNR in radiographs allows for an optimization of framing cameras to yield the best image quality.

A.2 Theory

Here we first consider the noise properties of the signal from a single pixel on the detector and then, in the following section, consider the implications of the fact that the local signal on the detector may include contributions from many neighboring pixels.

We ignore the potential contributions from x-rays that do not enter the pores in the MCP. The SNR in MCP-intensified radiographs is generally an order of magnitude higher than what is expected from an examination of the MCP statistics. The variance in the images is reduced due to blurring from the point spread function (PSF). However, it is important to note that the spatial blurring reduces the information in the image.

A.2.1 Microchannel plate statistics

For an input x-ray flux of N_γ photons per pixel, a MCP quantum efficiency η_{MCP}, and average gain g_{MCP}, the MCP output per pixel is

$$N_{\mathrm{MCP}} = \eta_{\mathrm{MCP}} N_\gamma g_{\mathrm{MCP}} \tag{A.1}$$

We can write the variance in the output signal from a single pixel as (161)

$$\sigma^2_{N_{\mathrm{MCP}}} = g^2_{\mathrm{MCP}} \sigma^2_{\eta_{\mathrm{MCP}} N_\gamma} + \eta_{\mathrm{MCP}} N_\gamma \sigma^2_{g_{\mathrm{MCP}}} \tag{A.2}$$

The term $\sigma^2_{\eta_{\mathrm{MCP}} N_\gamma}$ is the variance in the number of incident photons that are detected per pixel and $\sigma^2_{g_{\mathrm{MCP}}}$ is the variance in the MCP electron gain. The former variance

term may be written as

$$\sigma^2_{\eta_{\mathrm{MCP}}N_\gamma} = \eta^2_{\mathrm{MCP}}\sigma^2_{N_\gamma} + \sigma^2_{\eta_{\mathrm{MCP}}} \tag{A.3}$$

Here $\sigma^2_{N_\gamma}$ represents the Poisson variation in the number of incident x-ray photons and $\sigma^2_{\eta_{\mathrm{MCP}}}$ is due to the binomial statistics of the detection process. Substituting the well known forms for the variance of Poisson and binomial processes simplifies Eq. (A.3) to $\sigma^2_{\eta_{\mathrm{MCP}}N_\gamma} = \eta_{\mathrm{MCP}}N_\gamma$. Using this simplified form of Eq. (A.3) in Eq. (A.2) yields

$$\sigma^2_{N_{\mathrm{MCP}}} = \eta_{\mathrm{MCP}}N_\gamma(g^2_{\mathrm{MCP}} + \sigma^2_{g_{\mathrm{MCP}}}) \tag{A.4}$$

Because of the large number of signal quanta at this stage, it is assumed that the subsequent contribution to the noise by the phosphor is negligible.

Defining the SNR as the ratio of the signal output to the standard deviation of the noise, the SNR per pixel at the framing camera output is then

$$SNR = \sqrt{\frac{\eta_{\mathrm{MCP}}}{1 + \frac{\sigma^2_{g_{\mathrm{MCP}}}}{g^2_{\mathrm{MCP}}}}} * \sqrt{N_\gamma} \tag{A.5}$$

The detection quantum efficiency (DQE) is a measure of how the output of a detector is degraded by noise. It is a useful measure of the performance of a measurement system as it is independent of the input signal level. The DQE is defined as $DQE = (SNR_{out}/SNR_{in})^2$. Since the input statistics are Poissonian, the DQE takes the form

$$DQE = \frac{\eta_{\mathrm{MCP}}}{1 + \frac{\sigma^2_{g_{\mathrm{MCP}}}}{g^2_{\mathrm{MCP}}}} \tag{A.6}$$

For a PHD that is exactly a negative exponential, $\sigma^2_{g_{\mathrm{MCP}}}/g^2_{\mathrm{MCP}} = 1$ and the above equation becomes equivalent to the expression given by Pawley (160). Electronically measuring the PHD allows for a determination of the three free parameters in Eq.

(A.6) thus the noise contribution of the MCP detection and multiplication statistics to the framing camera output.

A.2.2 Spatial blurring at the detector

Now we consider the implications of the fact that the PSF of a single pixel overlaps to nearby pixels. The signal at the detector is the per pixel signal with SNR described by Eq. (A.5) convolved with the PSF. Qualitatively, one would expect that a finite-width PSF would decrease the variance in the intensity as the signal in each pixel becomes correlated to its neighbors.

The total signal on the detector does not change; however, each pixel now samples many independent x-ray detections. The variance decreases by a factor of $1/N_{pix}^2$, where N_{pix} is the effective number of neighboring pixels that the signal at each pixel is correlated to. The SNR becomes

$$SNR = \sqrt{\frac{\eta_{\mathrm{MCP}} N_{pix}}{1 + \frac{\sigma_{g_{\mathrm{MCP}}}^2}{g_{\mathrm{MCP}}^2}}} * \sqrt{N_\gamma} + C_{bkg} \tag{A.7}$$

The term $1/N_{pix}$ may be calculated from the sum of the squares of the fractional contributions in intensities from neighboring pixels. This factor is then a function of the PSF width and the detector pixel size. For a 9 μm pixel detector and a Gaussian PSF(160) with a width of 50 μm(162), we find $N_{pix} = 55$. A constant background, including contributions from the MCP dark noise and parallel noise in the CCD, is contained within the term C_{bkg}.

A.3 Experiment

We performed measurements on a bare BURLE Long-Life$^{\mathrm{TM}}$ MCP with a length-to-diameter ratio of 40, channel diameter of 10 μm, and a bias angle of 8 °. A Manson source provided a uniform irradiation with Al K-α x-rays. These photons

were collimated to produce two beams of equal intensity at equal angles from the anode normal. One beam was directed to the MCP and the other was incident on a NIST-calibrated IRD AXUV-100 photodiode detector. As the photodiode quantum efficiency is 100%, the x-ray flux incident on the MCP can be calculated. The photon flux was kept low ($\sim$ 1 photon/s/channel) as to avoid saturation effects.

A planar anode suspended 1 mm away from the back face of the MCP collected the electron output which was shaped by an Amptek A250CF charge-sensitive preamplifier. The preamplifier gain was determined by careful measurements of the feedback capacitance. This allowed for a calibration between the preamplifier output and the absolute number of electrons per pulse. An Amptek PX4 digital pulse processor provided an output histogram of the pulse amplitudes to a PC.

With the measured pulse height distribution, we can calculate the mean of the gain and the variance. The ratio of the total pulses collected to the time integrated x-ray flux defines the quantum efficiency.

A.3.1 Results

Fig. A.1(a) shows the results from measurement of the MCP PHDs for a variety of applied voltages and Fig. A.1(b) plots the calculated DQE neglecting spatial effects at the detector. At an applied voltage of 900 V, we find the factor $\sigma^2_{g_{\mathrm{MCP}}}/g^2_{\mathrm{MCP}} = 0.68 \pm 0.05$ and the quantum efficiency $\eta_{\mathrm{MCP}} = 3.09 \pm 0.05$ % yielding the $DQE = 1.86 \pm 0.05$ %.

With the quantified MCP noise, we may analyze the SNR in a radiograph as shown in Fig. A.2(a). Each of the sixteen images were centered relative to a point chosen on the grid. Regions were sampled from each image of constant size and orientation with respect to the grid. The mean and standard deviation of the sampled regions were calculated yielding the SNR.

Assuming a linear detector response, by relating the intensity recorded by the

detector to an estimate of the x-ray flux, the images may be calibrated to x-ray photons per pixel. The unattenuated x-ray flux in the bright vacuum region in the final image may be may be calculated from the geometry of the framing camera and the conversion efficiency of the backlighter (163). Using the measured value of $3 * 10^{-3} \pm 30\%$ (93) for the conversion efficiency for Cl Ly-α, we estimate an incident flux of $(0.36 \pm 0.11)\ \gamma/\mu\text{m}^2$ in the vacuum region.

Plotted in Fig. A.2(b) is the calculated SNR from the sample points against the estimated x-ray flux per pixel. The data is fitted to Eq. (A.7) yielding $SNR = 1.63\sqrt{N_\gamma} + (0.6 \pm 0.6)$ as shown in the dashed line. The coefficient of the $\sqrt{N_\gamma}$ term has a systematic error of (+0.33, -0.19) arising from the uncertainty in the conversion efficiency and a random error of ± 0.6. The experimentally determined MCP and framing camera parameters yielded a value of $SNR = (1.00 \pm 0.02)\sqrt{N_\gamma}$. These results agree within a factor of two, confirming the scaling of the parameters in the analysis. This indicates that there may be an additional spatial averaging taking place and that better estimates of the photon flux on the MCP are needed.

A.4 Conclusion

We have developed an analytical form for the SNR in MCP-intensified radiographs. The analysis suggests that spatial blurring at the detector dominates the magnitude of the SNR, but the SNR scales with the Poisson statistics of the x-ray photon input. It has been assumed that the PSF width is constant for all output pulse sizes. Future work should be undertaken to assess the relationship between MCP gain and the PSF. The photon flux at the detector should be independently measured in future experiments to reduce the uncertainty in estimating the input signal level.

One method to increase the performance of a MCP framing camera is to implement a transmission photocathode (TPC). Since MCPs have quantum efficiency of essentially unity for low energy electrons(165), a TPC which converts some of the inci-

dent x-ray signal to electrons may significantly increase the quantum efficiency(166). Spreading of the electrons born within the TPC can lead to excitation of multiple MCP pores in parallel. This would lead to an increase in the size of the PSF on the detector. The expected rise in the SNR would come from both the greater throughput of the camera and the increased spatial averaging at the detector. The improved SNR would come at the cost of decreased spatial resolution.

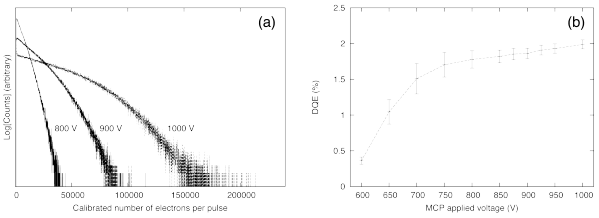

Figure A.1: (a) MCP PHDs for three sample voltages. The distributions fit negative exponentials at low voltages. For high voltages there is some rounding of the distribution at high gains indicating the onset of saturation effects. (b) The calculated DQE for a range of applied voltages 600-1000V. Above 850V, the DQE is relatively insensitive to changes in voltage. The higher quantum efficiency and gain is offset by the increased variance in the PHDs.

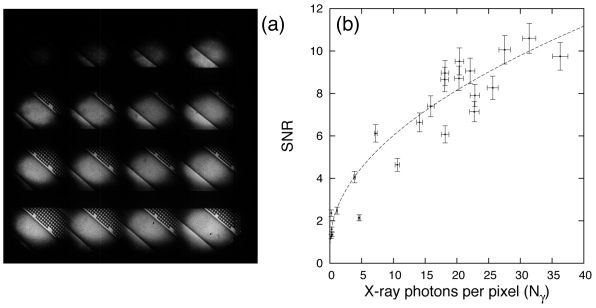

Figure A.2: (a) Shown is a series of radiographs taken by a 16 pinhole array illuminating a four strip MCP x-ray framing camera at the OMEGA laser (164) and a plot of the calculated SNR. The MCP parameters are similar to those described in Section A.3 with the bias voltage set to 900 V (b) Plotted is the calculated SNR against the estimated x-ray flux. The dashed line shows a fit of the data to Eq. (A.7). The uncertainties in the relative position of the data points arise from the finite size of the sampled regions in the images. Since the estimate of the x-ray flux is determined by the conversion efficiency, the uncertainty in the absolute scale in the horizontal axis is defined by the uncertainty in the conversion efficiency of $\pm$ 30% (93).

BIBLIOGRAPHY

BIBLIOGRAPHY

[1] J. J. Fortney, S. H. Glenzer, M. Koenig, B. Militzer, D. Saumon, and D. Valencia. Frontiers of the physics of dense plasmas and planetary interiors: Experiments, theory, and applications. *Phys. Plasmas*, 16(4):041003, 2009.

[2] S. Stanley and J. Bloxham. Convective-region geometry as the cause of Uranus' and Neptune's unusual magnetic fields. *Nature*, 428:151–153, 2004.

[3] B. Militzer, W. B. Hubbard, J. Vorberger, I. Tamblyn, and S. A. Bonev. A Massive Core in Jupiter Predicted from First-Principles Simulations. *Astrophys. J. Lett.*, 688(1):L45, 2008.

[4] J. Lindl. Development of the indirect-drive approach to inertial confinement fusion and the target physics basis for ignition and gain. *Phys. Plasmas*, 2(11):3933–4024, 1995.

[5] G. S. Fraley. Supernovae Explosions Induced by Pair-Production Instability. *Astrophys. Space Sci.*, 2:96–114, August 1968.

[6] S.H. Glenzer and R. Redmer. X-ray Thomson scattering in high energy density plasmas. *Rev. Mod. Phys.*, 81(4):1625–1663, Dec 2009.

[7] D. O. Gericke, J. Vorberger, K. Wünsch, and G. Gregori. Screening of ionic cores in partially ionized plasmas within linear response. *Phys. Rev. E*, 81:065401, Jun 2010.

[8] G. Gregori and D. O. Gericke. A reduced coupled-mode description for the electron-ion energy relaxation in dense matter. *Europhys. Lett.*, 83(1):15002, 2008.

[9] O.L. Landen, S.H. Glenzer, M.J. Edwards, R.W. Lee, G.W. Collins, R.C. Cauble, W.W. Hsing, and B.A. Hammell. Dense matter characterization by X-ray Thomson scattering. *J. Quant. Spectrosc. Radiat. Transfer*, 71(2-6):465 – 478, 2001.

[10] R. J. Pledger and J. A. Baross. Preliminary description and nutritional characterization of a chemoorganotrophic archaeobacterium growing at temperatures of up to 110 isolated from a submarine hydrothermal vent environment. *J. Gen. Microbiol.*, 137(1):203–211, 1991.

[11] B. Strömgren. Stars and Stellar Systems. In Lawrence H. Aller and Dean B. McLaughlin, editors, *Stellar Models for Main-sequence Stars and Subdwarfs*, volume 8, pages 269–295. University of Chicago Press, 1965.

[12] J D Lawson. Some Criteria for a Power Producing Thermonuclear Reactor. *Proc. R. Soc. London, Ser. B*, 70(1):6, 1957.

[13] S Pfalzner. *An Introduction to Inertial Confinement Fusion*. Taylor and Francis, 2006.

[14] E.I. Moses. Ignition on the National Ignition Facility: a path towards inertial fusion energy. *Nucl. Fusion*, 49(10):104022, 2009.

[15] R P. Drake. *High-Energy-Density Physics*. Springer, 2006.

[16] M. H. Key. Status of and prospects for the fast ignition inertial fusion concept. *Phys. Plasmas*, 14(5):055502, 2007.

[17] M. Tabak, J. Hammer, M. E. Glinsky, W. L. Kruer, S. C. Wilks, J. Woodworth, E. M. Campbell, M. D. Perry, and R. J. Mason. Ignition and high gain with ultrapowerful lasers. *Phys. Plasmas*, 1(5):1626–1634, 1994.

[18] R. Kodama, P. A. Norreys, K. Mima, A. E. Dangor, R. G. Evans, H. Fujita, Y. Kitagawa, K. Krushelnick, T. Miyakoshi, and N. Miyanaga et al. Fast heating of ultrahigh-density plasma as a step towards laser fusion ignition. *Nature*, 412, 2001.

[19] J. Soures, S. Kumpan, and J. Hoose. High Power Nd:Glass Laser for Fusion Applications. *Appl. Opt.*, 13(9):2081–2094, Sep 1974.

[20] S.A. Letzring. *Design and Development of an X-Ray Streak Camera for Laser Produced Plasma Measurement*. PhD thesis, University of Rochester, 1979.

[21] J. Soures, L.M. Goldman, and M. Lubin. Short-pulse-laser-heated plasma experiments. *Nucl. Fusion*, 13(6):829, 1973.

[22] J. Bunkenberg, J. Boles, D. Brown, J. Eastman, J. Hoose, R. Hopkins, L. Iwan, S. Jacobs, J. Kelly, and S. et al Kumpan. The omega high-power phosphate-glass system: Design and performance. *IEEE J. Quant. Electron.*, 17(9):1620 – 1628, 1981.

[23] P. A. Franken, A. E. Hill, C. W. Peters, and G. Weinreich. Generation of Optical Harmonics. *Phys. Rev. Lett.*, 7:118–119, Aug 1961.

[24] W. Seka, S.D. Jacobs, J.E. Rizzo, R. Boni, and R.S. Craxton. Demonstration of high efficiency third harmonic conversion of high power Nd-glass laser radiation. *Opt. Commun.*, 34(3):469 – 473, 1980.

[25] E. Bliss, J. Hunt, P. Renard, G. Sommargren, and H. Weaver. Effects of nonlinear propagation on laser focusing properties. *IEEE J. Quant. Electron.*, 12(7):402 – 406, jul 1976.

[26] Stanley Skupsky and Terrance Kessler. A source of hot spots in frequency-tripled laser light. *Opt. Commun.*, 70(2):123 – 127, 1989.

[27] Y. Lin, T. J. Kessler, and G. N. Lawrence. Distributed phase plates for super-Gaussian focal-plane irradiance profiles. *Opt. Lett.*, 20(7):764–766, Apr 1995.

[28] S. Skupsky, R. W. Short, T. Kessler, R. S. Craxton, S. Letzring, and J. M. Soures. Improved laser-beam uniformity using the angular dispersion of frequency-modulated light. *J. Appl. Phys.*, 66(8):3456–3462, 1989.

[29] S. P. Regan, J. A. Marozas, J. H. Kelly, T. R. Boehly, W. R. Donaldson, P. A. Jaanimagi, R. L. Keck, T. J. Kessler, D. D. Meyerhofer, and W. Seka et al. Experimental investigation of smoothing by spectral dispersion. *J. Opt. Soc. Am. B*, 17(9):1483–1489, Sep 2000.

[30] J. M. Soures, R. L. McCrory, C. P. Verdon, A. Babushkin, R. E. Bahr, T. R. Boehly, R. Boni, D. K. Bradley, D. L. Brown, and R. S. Craxton et al. Direct-drive laser-fusion experiments with the OMEGA, 60-beam, ¿ 40 kJ, ultraviolet laser system. *Phys. Plasmas*, 3(5):2108–2112, 1996.

[31] S. H. Batha, R. Aragonez, F. L. Archuleta, T. N. Archuleta, J. F. Benage, J. A. Cobble, J. S. Cowan, V. E. Fatherley, K. A. Flippo, and D. C. Gautier et al. TRIDENT high-energy-density facility experimental capabilities and diagnostics. *Rev. Sci. Instrum.*, 79(10):10F305, 2008.

[32] M. Roth, D. Jung, K. Falk, N. Guler, O. Deppert, M. Devlin, A. Favalli, J. Fernandez, D. Gautier, and M. et al Geissel. Bright Laser-Driven Neutron Source Based on the Relativistic Transparency of Solids. *Phys. Rev. Lett.*, 110:044802, Jan 2013.

[33] E. J. Gamboa, C. M. Huntington, M. R. Trantham, P. A. Keiter, R. P. Drake, D. S. Montgomery, J. F. Benage, and S. A. Letzring. Imaging x-ray Thomson scattering spectrometer design and demonstration (invited). *Rev. Sci. Instrum.*, 83(10):10E108, 2012.

[34] E.J. Gamboa, D.S. Montgomery, I.M. Hall, and R P. Drake. Imaging X-ray crystal spectrometer for laser-produced plasmas. *J. Instrum.*, 6:P04004, 2011.

[35] E.J. Gamboa, C.M Huntington, E.C. Harding, and R.P Drake. Electronic measurements of micro channel plate pulse height distributions. *Rev. Sci. Instrum.*, 83:10E310, 2010.

[36] P Watson, WG Kernohan, and RAB Möllan. A study of the cracking sounds from the metacarpophalangeal joint. *Proc. Inst. Mech. Eng. H J. Eng. Med.*, 203(2):109–118, 1989.

[37] S.P. Lyon and J. D. Johnson. SESAME: the Los Alamos National Laboratory equation of state database. *Los Alamos National Laboratory, Los Alamos, NM, LA-UR-92-3407*, 1992.

[38] A. B. Reighard, R. P. Drake, K. K. Dannenberg, D. J. Kremer, M. Grosskopf, E. C. Harding, D. R. Leibrandt, S. G. Glendinning, T. S. Perry, and B. A. Remington et al. Observation of collapsing radiative shocks in laboratory experiments. *Phys. Plasmas*, 13(8):082901, 2006.

[39] G.I. Taylor. The formation of a blast wave by a very intense explosion. II. The atomic explosion of 1945. *Proc. R. Soc. London, Ser. A*, 201(1065):175–186, 1950.

[40] G.I. Taylor. The formation of a blast wave by a very intense explosion. I. Theoretical discussion. *Proc. R. Soc. London, Ser. A*, 201(1065):159–174, 1950.

[41] D. G. Hicks, T. R. Boehly, P. M. Celliers, D. K. Bradley, J. H. Eggert, R. S. McWilliams, R. Jeanloz, and G. W. Collins. High-precision measurements of the diamond Hugoniot in and above the melt region. *Phys. Rev. B*, 78:174102, Nov 2008.

[42] P. M. Celliers, D. K. Bradley, G. W. Collins, D. G. Hicks, T. R. Boehly, and W. J. Armstrong. Line-imaging velocimeter for shock diagnostics at the OMEGA laser facility. *Rev. Sci. Instrum.*, 75(11):4916–4929, 2004.

[43] J. E. Miller, T. R. Boehly, A. Melchior, D. D. Meyerhofer, P. M. Celliers, J. H. Eggert, D. G. Hicks, C. M. Sorce, J. A. Oertel, and P. M. Emmel. Streaked optical pyrometer system for laser-driven shock-wave experiments on OMEGA. *Rev. Sci. Instrum.*, 78(3):034903, 2007.

[44] L. M. Barker and R. E. Hollenbach. Shock-Wave Studies of PMMA, Fused Silica, and Sapphire. *J. Appl. Phys.*, 41(10):4208–4226, 1970.

[45] J.H. Eggert, D.G. Hicks, P.M. Celliers, D.K. Bradley, R.S. McWilliams, R. Jeanloz, J.E. Miller, T.R. Boehly, and G.W. Collins. Melting temperature of diamond at ultrahigh pressure. *Nature Phys.*, 6:40–43, 2010.

[46] K. Falk, S.P. Regan, J. Vorberger, M.A. Barrios, T.R. Boehly, D.E. Fratanduono, S.H. Glenzer, D.G. Hicks, S.X. Hu, and C.D. Murphy et al. Self-consistent measurement of the equation of state of liquid deuterium. *High Energy Density Phys.*, 8(1):76 – 80, 2012.

[47] T. R. Boehly, V. N. Goncharov, W. Seka, S. X. Hu, J. A. Marozas, D. D. Meyerhofer, P. M. Celliers, D. G. Hicks, M. A. Barrios, D. Fratanduono, and G. W. Collins. Multiple spherically converging shock waves in liquid deuterium. *Phys. Plasmas*, 18(9):092706, 2011.

[48] M. A. Barrios, D. G. Hicks, T. R. Boehly, D. E. Fratanduono, J. H. Eggert, P. M. Celliers, G. W. Collins, and D. D. Meyerhofer. High-precision measurements of the equation of state of hydrocarbons at 1–10 Mbar using laser-driven shock waves. *Phys. Plasmas*, 17(5):056307, 2010.

[49] N. Ozaki, T. Sano, M. Ikoma, K. Shigemori, T. Kimura, K. Miyanishi, T. Vinci, F. H. Ree, H. Azechi, and T. Endo et al. Shock Hugoniot and temperature data for polystyrene obtained with quartz standard. *Phys. Plasmas*, 16(6):062702, 2009.

[50] R.S. McWilliams, D.K. Spaulding, J.H. Eggert, P.M. Celliers, D.G Hicks, R.F. Smith, G.W. Collins, and R. Jeanloz. Phase Transformations and Metallization of Magnesium Oxide at High Pressure and Temperature. *Science*, 338(6112):1330–1333, 2012.

[51] D. E. Fratanduono, T. R. Boehly, M. A. Barrios, D. D. Meyerhofer, J. H. Eggert, R. F. Smith, D. G. Hicks, P. M. Celliers, D. G. Braun, and G. W. Collins. Refractive index of lithium fluoride ramp compressed to 800 GPa. *J. Appl. Phys.*, 109(12):123521, 2011.

[52] Ya. B. Zel'dovich and Yu. P. Raizer. *Physics of Shock Waves and High Temperature Hydrodynamic Phenomena*. Dover, 1966.

[53] D. G. Hicks, T. R. Boehly, P. M. Celliers, J. H. Eggert, E. Vianello, D. D. Meyerhofer, and G. W. Collins. Shock compression of quartz in the high-pressure fluid regime. *Phys. Plasmas*, 12(8):082702, 2005.

[54] A.M. Evans, N.J. Freeman, P. Graham, C.J. Horsfield, S.D. Rothman, B.R. Thomas, and A.J. Tyrrell. Hugoniot EOS measurements at Mbar pressures. *Laser Part. Beams*, 14:113–123, 5 1996.

[55] D. G. Hicks, T. R. Boehly, P. M. Celliers, J. H. Eggert, S. J. Moon, D. D. Meyerhofer, and G. W. Collins. Laser-driven single shock compression of fluid deuterium from 45 to 220 GPa. *Phys. Rev. B*, 79:014112, Jan 2009.

[56] M. D. Knudson and M. P. Desjarlais. Shock Compression of Quartz to 1.6 TPa: Redefining a Pressure Standard. *Phys. Rev. Lett.*, 103:225501, Nov 2009.

[57] D. Hoarty, O. Willi, L. Barringer, C. Vickers, R. Watt, and W. Nazarov. Observation of ionization fronts in low density foam targets. *Phys. Plasmas*, 6(5):2171–2177, 1999.

[58] P. A. Keiter, R P. Drake, T. S. Perry, H. F. Robey, B. A. Remington, C. A. Iglesias, R. J. Wallace, and J. Knauer. Observation of a Hydrodynamically Driven, Radiative-Precursor Shock. *Phys. Rev. Lett.*, 89(16):165003, 2002.

[59] T. Afshar-rad, M. Desselberger, M. Dunne, J. Edwards, J. M. Foster, D. Hoarty, M. W. Jones, S. J. Rose, P. A. Rosen, R. Taylor, and O. Willi. Supersonic

Propagation of an Ionization Front in Low Density Foam Targets Driven by Thermal Radiation. *Phys. Rev. Lett.*, 73:74–77, Jul 1994.

[60] H. Sawada, S. P. Regan, P. B. Radha, R. Epstein, D. Li, V. N. Goncharov, S. X. Hu, D. D. Meyerhofer, J. A. Delettrez, P. A. Jaanimagi, V. A. Smalyuk, T. R. Boehly, T. C. Sangster, B. Yaakobi, and R. C. Mancini. Al 1s-2p absorption spectroscopy of shock-wave heating and compression in laser-driven planar foil. *Phys. Plasmas*, 16(5):052702, 2009.

[61] P A. Keiter, A Comely, J Morton, H Tierney, J Workman, and Mark Taylor. Conversion efficiency of high-Z backlighter materials. *Rev. Sci. Instrum.*, 79(10):10E918, 2008.

[62] A.H. Compton. A Quantum Theory of the Scattering of X-rays by Light Elements. *Phys. Rev.*, 21(5):483–502, May 1923.

[63] G. Gregori, S. H. Glenzer, W. Rozmus, R. W. Lee, and O. L. Landen. Theoretical model of x-ray scattering as a dense matter probe. *Phys. Rev. E*, 67:026412, 2003.

[64] S. H. Glenzer, G. Gregori, R. W. Lee, F. J. Rogers, S. W. Pollaine, and O. L. Landen. Demonstration of Spectrally Resolved X-Ray Scattering in Dense Plasmas. *Phys. Rev. Lett.*, 90(17):175002, May 2003.

[65] A. L. Kritcher, P. Neumayer, H. J. Lee, T. Döppner, R. W. Falcone, S. H. Glenzer, and E. C. Morse. Demonstration of x-ray Thomson scattering using picosecond K-alpha x-ray sources in the characterization of dense heated matter. *Rev. Sci. Instrum.*, 79(10):10E739, 2008.

[66] A.L. Kritcher et al. Measurements of Ionic Structure in Shock Compressed Lithium Hydride from Ultrafast X-Ray Thomson Scattering. *Phys. Rev. Lett.*, 103(24):245004, Dec 2009.

[67] H. Sawada et al. Diagnosing direct-drive, shock-heated, and compressed plastic planar foils with noncollective spectrally resolved x-ray scattering. *Phys. Plasmas*, 14(12):122703, 2007.

[68] H. J. Lee, P. Neumayer, J. Castor, T. Döppner, R. W. Falcone, C. Fortmann, B. A. Hammel, A. L. Kritcher, O. L. Landen, and R. W. et al Lee. X-Ray Thomson-Scattering Measurements of Density and Temperature in Shock-Compressed Beryllium. *Phys. Rev. Lett.*, 102(11):115001, Mar 2009.

[69] S. P. Regan, K. Falk, G. Gregori, P. B. Radha, S. X. Hu, T. R. Boehly, B. J. B. Crowley, S. H. Glenzer, O. L. Landen, and D. O. et al Gericke. Inelastic X-Ray Scattering from Shocked Liquid Deuterium. *Phys. Rev. Lett.*, 109:265003, Dec 2012.

[70] G. Gregori, S.H. Glenzer, H.-K. Chung, D.H. Froula, R.W. Lee, N.B. Meezan, J.D. Moody, C. Niemann, O.L. Landen, and B. Holst et al. Measurement of carbon ionization balance in high-temperature plasma mixtures by temporally resolved X-ray scattering. *J. Quant. Spectrosc. Radiat. Transfer*, 99(13):225 – 237, 2006.

[71] G. Gregori, S. H. Glenzer, K. B. Fournier, K. M. Campbell, E. L. Dewald, O. S. Jones, J. H. Hammer, S. B. Hansen, R. J. Wallace, and O. L. Landen. X-Ray Scattering Measurements of Radiative Heating and Cooling Dynamics. *Phys. Rev. Lett.*, 101(4):045003, Jul 2008.

[72] G. Gregori, S. H. Glenzer, F. J. Rogers, S. M. Pollaine, O. L. Landen, C. Blancard, G. Faussurier, P. Renaudin, S. Kuhlbrodt, and R. Redmer. Electronic structure measurements of dense plasmas. *Phys. Plasmas*, 11(5):2754–2762, 2004.

[73] A. J. Visco, R. P. Drake, S. H. Glenzer, T. Döppner, G. Gregori, D. H. Froula, and M. J. Grosskopf. Measurement of Radiative Shock Properties by X-Ray Thomson Scattering. *Phys. Rev. Lett.*, 108:145001, Apr 2012.

[74] C.M. Huntington. *High-Energy-Density Physics Experiments Relevant to Astrophysical Systems*. PhD thesis, University of Michigan, 2012.

[75] S. Ichimaru. *Basic Principles of Plasma Physics*. W.A. Benjamin, Inc., 1973.

[76] R Kubo. The fluctuation-dissipation theorem. *Rep. Prog. Phys.*, 29(1):255, 1966.

[77] D. Froula, S.H. Glenzer, N.C. Luhmann, and J. Sheffield. *Plasma Scattering of Electromagnetic Radiation*. Academic Press, 2010.

[78] J. Chihara. Interaction of photons with plasmas and liquid metals - photoabsorption and scattering. *J. Phys.: Condens. Matter*, 12(3):231, 2000.

[79] J Chihara. Difference in X-ray scattering between metallic and non-metallic liquids due to conduction electrons. *J. Phys. F*, 17(2):295, 1987.

[80] J W. M. Du Mond. Compton Modified Line Structure and its Relation to the Electron Theory of Solid Bodies. *Phys. Rev.*, 33:643–658, May 1929.

[81] P. Eisenberger and P. M. Platzman. Compton Scattering of X Rays from Bound Electrons. *Phys. Rev. A*, 2:415–423, Aug 1970.

[82] P. Holm and R. Ribberfors. First correction to the nonrelativistic Compton cross section in the impulse approximation. *Phys. Rev. A*, 40:6251–6259, Dec 1989.

[83] F. Bloch. Contribution to the Theory of the Compton-Line. *Phys. Rev.*, 46:674–687, Oct 1934.

[84] P. A. Ross and P. Kirkpatrick. Effect of Electron Binding upon the Magnitude of the Compton Shift. *Phys. Rev.*, 46:129–155, Oct 1934.

[85] M.J. Cooper R.J. Weiss and R.S. Holt. The Compton Defect. *Philos. Mag.*, 36(1):193–200, 1977.

[86] M Schumacher, F Smend, and I Borchert. Incoherent scattering of gamma rays by inner-shell electrons. *J. Phys. B.*, 8(9):1428, 1975.

[87] H. H. Johann. Die Erzeugung lichtstarker Röntgenspektren mit Hilfe von Konkavkristallen. *Z. Kristallogr.*, 69:185–206, 1931.

[88] T Johansson. Über ein neuartiges, genau fokussierendes Röntgenspektrometer. *Z. Phys.*, 82:507–528, 1933.

[89] L. von Hámos. Formation of true X-ray images by reflection on crystal mirrors. *Z. Kristallogr.*, 101(17), 1939.

[90] Y Aglitskiy, T Lehecka, S Obenschain, S Bodner, C Pawley, K Gerber, J Sethian, C M. Brown, J Seely, U Feldman, and G Holland. High-resolution monochromatic x-ray imaging system based on spherically bent crystals. *Appl. Opt.*, 37(22):5253–5261, Aug 1998.

[91] Y Aglitskiy, F G Serpa, E S Meyer, J D Gillaspy, C M Brown, A Ya Faenov, and T A Pikuz. The use of a Spherically Curved Crystal Spectrometer for X-ray Measurements on Electron Beam Ion Trap. *Phys. Scr.*, 58(2):178, 1998.

[92] A. Pak, G. Gregori, J. Knight, K. Campbell, D. Price, B. Hammel, O. L. Landen, and S. H. Glenzer. X-ray line measurements with high efficiency Bragg crystals. *Rev. Sci. Instrum.*, 75(10):3747–3749, 2004.

[93] M.K. Urry, G. Gregori, O.L. Landen, A. Pak, and S.H. Glenzer. X-ray probe development for collective scattering measurements in dense plasmas. *J. Quant. Spectrosc. Radiat. Transfer*, 99(1-3):636 – 648, 2006. Radiative Properties of Hot Dense Matter.

[94] B. Yaakobi and A. Burek. Crystal diffraction systems for X-ray spectroscopy, imaging, and interferometry of laser fusion targets. *IEEE J. Quantum Electron.*, 19(12):1841 – 1854, December 1983.

[95] A. Ya. Faenov, I. Yu. Skobelev, S. A. Pikuz, G. A. Kyrala, R. D. Fulton, J. Abdallah, and D. P. Kilcrease. High-resolution x-ray spectroscopy of a subpicosecond-laser-produced silicon plasma. *Phys. Rev. A*, 51(5):3529–3533, May 1995.

[96] T A. Pikuz, A Y. Faenov, A. I. Magunov, I Y. Skobelev, F. Blasco, C. Stenz, F Salin, P. Monot, T. Auguste, and Sandrine Dobosz. High-resolution X-Ray spectromicroscopy of fs laser-produced plasma by tunable, high-luminosity spherical crystal spectrometers with X-Ray CCD or MCP. *Proc. SPIE*, 4504:12–25, 2001.

[97] P. Monot, T. Auguste, S. Dobosz, P. DOliveira, S. Hulin, M. Bougeard, A.Ya. Faenov, T.A. Pikuz, and I.Yu. Skobelev. High-sensitivity, portable, tunable imaging X-ray spectrometer. *Nucl. Instrum. Meth. A*, 484:299–211, 2002.

[98] D. B. Sinars et al. Plasma Imaging and Spectroscopy Diagnostics Developed on 100–500-kA Pulsed Power Devices. *Proc. IEEE*, 92:1110–1121, 2004.

[99] D.B. Sinars, G.A. Chandler, J.E. Bailey, R.C. Mancini, G.A. Rochau, D.F. Wenger, R.G. Adams, M.L. Adams, H.A. Scott, and A.Ya. Faenov et al. Measurements of K-shell Ar spectra from z-pinch dynamic hohlraum experiments made using a focusing spectrometer with spatial resolution. *J. Quant. Spectrosc. Radiat. Transfer*, 99:595–613, 2006.

[100] T. A. Shelvenko et al. Use of spherically bent crystals to diagnose wire array z pinches. *Rev. Sci. Instrum.*, 75(10):3681–3683, 2004.

[101] B.K.F. Young. High-resolution x-ray spectrometer based on spherically bent crystals for investigations of femtosecond laser plasmas. *Rev. Sci. Instrum.69*, 1998(4049-4053), 12.

[102] D B. Sinars, G R. Bennett, D F. Wenger, M E. Cuneo, and J L. Porter. Evaluation of Bent-Crystal X-Ray Backlighting and Microscopy Techniques for the Sandia Z Machine. *Appl. Opt.*, 42(19):4059–4071, Jul 2003.

[103] E. Förster, K. Gabel, and I. Uschmann. New crystal spectrograph designs and their application to plasma diagnostics (invited). *Rev. Sci. Instrum.*, 63(10):5012–5016, 1992.

[104] M Vollbrecht, O Treichel, I Uschmann, K Gäbel, R Lebert, and E Förster. Soft-X-Ray Imaging with Toroidally Curved Thallium Acid Phthalate Crystals in the Water Window. *Appl. Opt.*, 37(10):1803–1807, Apr 1998.

[105] E. Förster, K. Gabel, and I. Uschmann. X-ray microscopy of laser-produced plasmas with the use of bent crystals. *Laser Part. Beams*, 9(1):135–148, 1991.

[106] O. Renner I.M. Hall, N.C. Woolsey and I. Uschmann. High-resolution X-ray spectroscopy using toroidally bent crystals. *Central Laser Facility Rutherford, Appleton Laboratory Annual Report*, pages 47–48, 2003-2004.

[107] T. Missalla, I. Uschmann, E. Förster, G. Jenke, and D. von der Linde. Monochromatic focusing of subpicosecond x-ray pulses in the keV range. *Rev. Sci. Instrum.*, 70(2):1288–1299, 1999.

[108] W.H. Zachariasen. *X-ray Diffraction in Crystals*. John Wiley and Sons, 1944.

[109] I. Uschmann, E. Förster, K. Gäbel, G. Hölzer, and M. Ensslen. X-ray reflection properties of elastically bent perfect crystals in Bragg geometry. *J. Appl. Crystallogr.*, 26(3):405–412, Jun 1993.

[110] C. Welnak, P. Anderson, M. Khan, S. Singh, and F. Cerrina. Recent developments in SHADOW. *Rev. Sci. Instrum.*, 63(1):865–868, 1992.

[111] J.F. Seely, G E. Holland, L T. Hudson, and A Henins. X-ray modulation transfer functions of photostimulable phosphor image plates and scanners. *Appl. Opt.*, 47(31):5753–5761, Nov 2008.

[112] J. A. Koch, Y. Aglitskiy, C. Brown, T. Cowan, R. Freeman, S. Hatchett, G. Holland, M. Key, A. MacKinnon, J. Seely, R. Snavely, and R. Stephens. 4.5- and 8-keV emission and absorption x-ray imaging using spherically bent quartz 203 and 211 crystals (invited). *Rev. Sci. Instrum.*, 74(3):2130–2135, 2003.

[113] M Sanchez del Rio and R J. Dejus. XOP: a multiplatform graphical user interface for synchrotron radiation spectral and optics calculations. *Proc. SPIE*, 3152(1):148–157, 1997.

[114] T. R. Boehly et al. Initial performance results of the OMEGA laser system. *Opt. Commun.*, 133(1-6):495 – 506, 1997.

[115] G.E. Ice and C.J. Sparks Jr. Mosaic crystal X-ray spectrometer to resolve inelastic background from anomalous scattering experiments. *Nuclear Instruments and Methods in Physics Research Section A: Accelerators, Spectrometers, Detectors and Associated Equipment*, 291(12):110 – 116, 1990.

[116] A P. Shevelko, A A. Antonov, I G. Grigorieva, Y S. Kasyanov, L V. Knight, A Reyes-Mena, C Turner, Q Wang, and O F. Yakushev. Focusing crystal von Hamos spectrometer for x-ray spectroscopy and x-ray fluorescence applications. In Carolyn A. MacDonald and Ali M. Khounsary, editors, *Advances in Laboratory-based X-Ray Sources and Optics*, volume 4144, pages 148–154. SPIE, 2000.

[117] Jonathan Workman and George A. Kyrala. Scaling of x-ray K-shell sources from laser-solid interactions. *Proc. SPIE*, 4504(1):168–179, 2001.

[118] L. E. Ruggles, Jr. J. L. Porter, P. K. Rambo, W. W. Simpson, M. F. Vargas, G. R. Bennett, and I. C. Smith. Measurements of 4–10 keV x-ray production with the Z-Beamlet laser. *Rev. Sci. Instrum.*, 74(3):2206–2210, 2003.

[119] F. Zamponi et al. Characterization of a deep depletion, back-illuminated charge-coupled device in the x-ray range. *Rev. Sci. Instrum.*, 76(11):116101, 2005.

[120] A. L. Meadowcroft, C. D. Bentley, and E. N. Stott. Evaluation of the sensitivity and fading characteristics of an image plate system for x-ray diagnostics. *Rev. Sci. Instrum.*, 79(11):113102, 2008.

[121] T. Shirai, J. Sugar, A. Musgrove, and W.L. Wiese. Spectral Data for Highly Ionized Atoms: Ti, V, Cr, Mn, Fe, Co, Ni, Cu, Kr, and Mo. In M. W. Chase, editor, *Journal of Physical and Chemical Reference Data Monograph No. 8*. American Institute of Physics, 2000.

[122] H. Hsuan, M. Bitter, K. W. Hill, S. von Goeler, B. Grek, D. Johnson, L. C. Johnson, S. Sesnic, C. P. Bhalla, K. R. Karim, F. Bely-Dubau, and P. Faucher. Satellite spectra of Heliumlike nickel. *Phys. Rev. A*, 35:4280–4285, May 1987.

[123] M. Bitter, K. W. Hill, N. R. Sauthoff, P. C. Efthimion, E. Meservey, W. Roney, S. von Goeler, R. Horton, M. Goldman, and W. Stodiek. Dielectronic Satellite Spectrum of Heliumlike Iron (Fe XXV). *Phys. Rev. Lett.*, 43:129–132, Jul 1979.

[124] A. J. Smith, M. Bitter, H. Hsuan, K. W. Hill, S. von Goeler, J. Timberlake, P. Beiersdorfer, and A. Osterheld. $K\ \beta$ spectra of heliumlike iron from tokomak-fusion-test-reactor plasmas. *Phys. Rev. A*, 47:3073–3079, Apr 1993.

[125] U I Safronova, M S Safronova, and R Bruch. Relative intensity of dielectronic satellite spectra for highly charged He-like ions (1s2l"nl-1s 2 n'l', n, n'=2, 3) with Z=6-54. *J. Phys. B: At., Mol. Opt. Phys.*, 28(14):2803, 1995.

[126] J. Workman, N. E. Lanier, and G. A. Kyrala. Analysis of Ti K-shell emission produced from solid targets using nanosecond pulses on the TRIDENT laser facility. *Rev. Sci. Insturm.*, 74(3):2165–2168, 2003.

[127] C.I. Szabó, L.T. Hudson, A. Henins, G.E. Holland, R. Atkin, and J.F. Seely. Mitigation of fluorescence and scattering in reflection convex-crystal X-ray spectrometers. *Radiat. Phys. Chem.*, 75(11):1824 – 1829, 2006.

[128] J. A. Bearden and A. F. Burr. Reevaluation of X-Ray Atomic Energy Levels. *Rev. Mod. Phys.*, 39:125–142, Jan 1967.

[129] J.H. Hubbell et al. A Review, Bibliography and Tabulation of K,L, and Higher Atomic Shell X-Ray Fluorescence Yields. *J. Phys. Chem. Ref. Data*, 23(2):339–364, 1994.

[130] H.-S. Park, B. R. Maddox, E. Giraldez, S. P. Hatchett, L. T. Hudson, N. Izumi, M. H. Key, S. Le Pape, A. J. MacKinnon, and A. G. MacPhee et al. High-resolution 17–75 keV backlighters for high energy density experiments. *Phys. Plasmas*, 15(7):072705, 2008.

[131] A. L. Kritcher, T. Döppner, C. Fortmann, T. Ma, O. L. Landen, R. Wallace, and S. H. Glenzer. In-Flight Measurements of Capsule Shell Adiabats in Laser-Driven Implosions. *Phys. Rev. Lett.*, 107(1):015002, July 2011.

[132] R.W. Pekala. Organic aerogels from the polycondensation of resorcinol with formaldehyde. *J. Mater. Sci.*, 24:3221–3227, 1989.

[133] B. van der Holst et al. CRASH: A Block-adaptive-mesh Code for Radiative Shock Hydrodynamics Implementation and Verification. *Astrophys. J. Suppl. S.*, 194(2):23, 2011.

[134] L. R. Benedetti, P. M. Bell, D. K. Bradley, C. G. Brown, S. M. Glenn, R. Heeter, J. P. Holder, N. Izumi, S. F. Khan, G. Lacaille, N. Simanovskaia, V. A. Smalyuk, and R. Thomas. Crosstalk in x-ray framing cameras: Effect on voltage, gain, and timing (invited). *Rev. Sci. Instrum.*, 83(10):10E135, 2012.

[135] G Gregori, S H Glenzer, and O L Landen. Strong coupling corrections in the analysis of x-ray Thomson scattering measurements. *J. Phys. A: Math. Gen.*, 36(22):5971, 2003.

[136] G. Gregori, A. Ravasio, A. Hll, S.H. Glenzer, and S.J. Rose. Derivation of the static structure factor in strongly coupled non-equilibrium plasmas for X-ray scattering studies. *High Energy Density Phys.*, 3(12):99 – 108, 2007. ¡ce:title¿Radiative Properties of Hot Dense Matter¡/ce:title¿.

[137] C. Fortmann, R. Thiele, R.R. Fustlin, Th. Bornath, B. Holst, W.-D. Kraeft, V. Schwarz, S. Toleikis, Th. Tschentscher, and R. Redmer. Thomson scattering in dense plasmas with density and temperature gradients. *High Energy Density Phys.*, 5(3):208 – 211, 2009.

[138] K. Huang. *Statistical Mechanics*. John Wiley & Sons, 1987.

[139] H.-K. Chung, M.H. Chen, W.L. Morgan, Y. Ralchenko, and R.W. Lee. FLYCHK: Generalized population kinetics and spectral model for rapid spectroscopic analysis for all elements. *High Energy Density Phys.*, 1(1):3 – 12, 2005.

[140] B. A. Mattern and G. T. Seidler. Theoretical treatments of the bound-free contribution and experimental best practice in X-ray Thomson scattering from warm dense matter. *Phys. Plasmas*, 20(2):022706, 2013.

[141] Ya. B. Zeldovich. Motion of a gas under the action of an impulsive pressure (load). *Akust. Zh.*, 2:28–38, 1956.

[142] V.B. Adamskii. Integration of the system of self-similar equations in the problem of an impulsive load on a cold gas. *Akust. Zh.*, 2:3–9, 1956.

[143] A.I. Zhukov and Ya. M. Kazhdan. On the motion of a gas under the action of a short duration impulse. *Akust. Zh.*, 2:352–357, 1956.

[144] A.V. Voloshinov and S.V. Fal'kovich. One-dimensional problem of a shock in a gas. *Fluid Dyn.*, 6:74–78, 1973.

[145] M Koenig, A Benuzzi, B Faral, D Batani, L Mller, F Torsiello, T Hall, N Grandjouan, and W Nazarov. EOS Data Experiments for Plastic Foams Using Smoothed Laser Beams. *Astrophys. J. Suppl. S.*, 127(2):385, 2000.

[146] S Le Pape, A Macphee, D Hey, P Patel, A Mackinnon, M Key, J Pasley, M Wei, S Chen, and T Ma et al. Density measurement of shock compressed foam using two-dimensional x-ray radiography. *Rev. Sci. Instrum.*, 79(10):106104, 2008.

[147] E. C. Harding, J. F. Hansen, O. A. Hurricane, R. P. Drake, H. F. Robey, C. C. Kuranz, B. A. Remington, M. J. Bono, M. J. Grosskopf, and R. S. Gillespie. Observation of a Kelvin-Helmholtz Instability in a High-Energy-Density Plasma on the Omega Laser. *Phys. Rev. Lett.*, 103:045005, Jul 2009.

[148] E.C. Harding. *Observations of shear flows in high-energy-density plasmas*. PhD thesis, University of Michigan, 2010.

[149] D. Salzmann. *Atomic Physics in Hot Plasmas*. Oxford University Press, USA, 1998.

[150] J. T. Larsen and S. M. Lane. HYADES A plasma hydrodynamics code for dense plasma studies. *J. Quant. Spectrosc. Radiat. Transfer*, 51(12):179 – 186, 1994.

[151] A. R. Miles, D. G. Braun, M. J. Edwards, H. F. Robey, R. P. Drake, and D. R. Leibrandt. Numerical simulation of supernova-relevant laser-driven hydro experiments on OMEGA. *Phys. Plasmas*, 11(7):3631–3645, 2004.

[152] K Kanaya and S Okayama. Penetration and energy-loss theory of electrons in solid targets. *J. Phys. D: Appl. Phys.*, 5(1):43, 1972.

[153] G. W. Collins, L. B. Da Silva, P. Celliers, D. M. Gold, M. E. Foord, R. J. Wallace, A. Ng, S. V. Weber, K. S. Budil, and R. Cauble. Measurements of the Equation of State of Deuterium at the Fluid Insulator-Metal Transition. *Science*, 281(5380):1178–1181, 1998.

[154] B. A. Remington, J. Kane, R. P. Drake, S. G. Glendinning, K. Estabrook, R. London, J. Castor, R. J. Wallace, D. Arnett, and E. Liang et al. Supernova hydrodynamics experiments on the Nova laser. *Phys. Plasmas*, 4(5):1994–2003, 1997.

[155] D. Ryutov, R. P. Drake, J. Kane, E. Liang, B. A. Remington, and W. M. Wood-Vasey. Similarity Criteria for the Laboratory Simulation of Supernova Hydrodynamics. *Astrophys. J.*, 518(2):821, 1999.

[156] Joseph Ladislas Wiza. Microchannel Plate Detectors. *Nucl. Instrum. Methods*, 162:60–1, 1979.

[157] A. J. Guest. A computer model of channel multiplier plate performance. *Acta Electronica*, 14:79–97, 1971.

[158] W. Parkes, R. Gott, and K. A. Pounds. Soft X-Ray Studies of Channel Multipliers and Multiplier Arrays. *IEEE Trans. Nucl. Sci.*, 17:360–366, 1970.

[159] C. C. Kuranz, B. E. Blue, R. P. Drake, H. F. Robey, J. F. Hansen, J. P. Knauer, M. J. Grosskopf, C. Krauland, and D. C. Marion. Dual, orthogonal, backlit pinhole radiography in OMEGA experiments. *Rev. Sci. Instrum.*, 77(10):10E327, 2006.

[160] C J. Pawley and A. V. Deniz. Improved measurements of noise and resolution of x-ray framing cameras at 1–2 keV. *Nucl. Instrum. Meth. A*, 71(3):1286–1295, 2000.

[161] H. J. Zweig. Detective Quantum Efficiency of Photodetectors with Some Amplification Mechanisms. *J. Opt. Soc. Am.*, 55(5):525–528, 1965.

[162] M. E. Lowenstern, E. C. Harding, C. M. Huntington, A. J. Visco, G. Rathore, and R. P. Drake. Performance of Au transmission photocathode on a microchannel plate detector. *Rev. Sci. Instrum.*, 79(10):10E912, 2008.

[163] D. K. Bradley, O. L. Landen, A. B. Bullock, S. G. Glendinning, and R. E. Turner. Efficient, 1–100-keV x-ray radiography with high spatial and temporal resolution. *Opt. Lett.*, 27(2):134–136, 2002.

[164] T. R. Boehly, R. S. Craxton, T. H. Hinterman, J. H. Kelly, T. J. Kessler, S. A. Kumpan, S. A. Letzring, R. L. McCrory, S. F. B. Morse, W. Seka, S. Skupsky, J. M. Soures, and C. P. Verdon. The upgrade to the OMEGA laser system. *Rev. Sci. Instrum.*, 66(1):508–510, 1995.

[165] G. W. Fraser, J. F. Pearson, G. C. Smith, M. Lewis, and M. A. Barstow. The gain characteristics of microchannel plates for X-ray photon counting. *IEEE Trans. Nucl. Sci.*, 30:455–460, 1983.

[166] G. W. Fraser. The characterisation of soft X-ray transmission photocathodes. *Nucl. Instrum. Meth. A*, 228:532–540, January 1985.